Estimation and control of noise amplifier flows using data-based approaches

J. Guzman Inigo

Ecole Polytechnique

Thèse présentée en vue de l'obtention du titre de

Docteur de l'Ecole Polytechnique

Par

Juan Guzmán Iñigo

Estimation and control of noise amplifier flows using data-based approaches

---

Soutenue le 4 novembre 2015 devant un jury composé de :

François Gallaire	EPFL	Rapporteur
Georgios Papadakis	Imperial College London	Rapporteur
Jean-Luc Aider	ESPCI Paris	Examinateur
Sherwin Bagheri	KTH	Examinateur
Jean-Christophe Robinet	ENSAM Paris	Examinateur
Denis Sipp	ONERA	Directeur de Thèse
Peter Schmid	Imperial College London	Directeur de Thèse

ONERA

THE FRENCH AEROSPACE LAB

ESTIMATION AND CONTROL OF NOISE AMPLIFIER FLOWS USING DATA-BASED APPROACHES

This work aims at providing new modelling strategies for noise-amplifier flows using data-based approaches. This kind of flows are particularly difficult to model since the upstream noise environment, triggering the flow via a receptivity process, is not known. The proposed framework is illustrated on the case of a transitional flat-plate boundary layer – a classical an generic flow that acts as a noise amplifier. A system-identification approach, rather than a classical Galerkin technique, is used to extract a model of the flow from time-synchronous velocity snapshots and wall-shear stress measurements. The model obtained is then used to build an efficient closed-loop controller to significantly reduce the kinetic energy of the perturbation field and thus successfully delay transition.

Keywords: Noise-amplifier flows, Closed-loop control, System-identification, Reduced-order models, Dynamic observer, Linear estimator.

Contents

Chapter 1

Introduction

Flow control is a discipline which has grown substantially over the last few years. Improving mixing processes, reducing noise emissions, suppressing instabilities, or reducing drag are some examples of the problems to which flow control may provide technological solutions. In the current economic context, with scarce energetic resources and an increasing awareness about the environment, these solutions are of special interest to the aeronautical and automotive industries.

The focus of this work is the suppression of unsteadiness arising from hydrodynamic instabilities and, in particular, from convective instabilities. For this purpose, a model-based closed-loop control strategy was considered. The aim of this thesis is to contribute to the theoretical development of data-based techniques to obtain models of the flow which can be used in the control design.

1.1 Flow unsteadiness

Unsteadiness in open flows can be classified into two main categories (Huerre and Rossi, 1998): (i) oscillator-type flows, which are defined by a global instability resulting in self-sustained oscillatory fluid behaviour (intrinsic dynamics); and (ii) noise amplifiers, which are characterised by selectively amplifying the noise which is already present in the upstream flow (extrinsic dynamics). Different control and modelling strategies should be considered depending on the type of unsteadiness.

1.1.1 Oscillator-type flows

Oscillator flows are characterized by a self-sustained beating of the flow at a certain frequency. The usual mechanism leading to the unsteadiness in oscillators consists in the exponential growth of small perturbations of the flow field and the subsequent saturation into a limit cycle due to non-linearities. At low Reynolds number, the viscous terms damp any perturbation and the flow is steady. As the Reynolds number increases, the convective terms become dominant and a Hopf bifurcation may occur: a theoretical steady unstable solution (base flow) coexists with an unsteady state which drives the system.

The dynamics of oscillator flows is well predicted by global stability analysis (Jackson, 1987). Conceptually, a stability analysis studies the linear development of small perturbations around a fixed point solution of the Navier-Stokes equations (base flow). The most unstable mode of the system determines the dynamics of the flow and defines a characteristic frequency. The frequency predicted by the linear analysis may, however, be shifted by non-linearities (Sipp and Lebedev, 2007).

1.1.2 Noise-amplifier flows

On the other hand, fluid systems that fall under the category of noise amplifiers are characterized by a globally stable spectrum. In this case, the unsteadiness arise from convective instabilities which amplify the existing environmental perturbations. The length scales and frequencies of the detected unsteadiness have a broad range and only exist if the flow is perturbed by an external noise source (extrinsic dynamics).

It is worth mentioning that a global stability analysis of noise-amplifier flows is an ill-posed mathematical problem (Trefethen et al., 1993) due to the non-normality of the linearised Navier-Stokes operator. The non-normality is also responsible for the transient-growth which amplifies the external noise (Schmid and Henningson, 2001; Chomaz, 2005; Schmid, 2007). Consequently, these flows are preferably studied using the resolvent operator which highlights the transient amplification of perturbations in such systems (Sipp and Marquet, 2013).

1.2 Flow control

Flow unsteadiness may be detrimental for engineering applications (structural fatigue, noise generation, laminar-turbulent transition or combustion instabilities (Dowling and Morgans, 2005)), or even endanger the safety of operation (shock buffeting (Jacquin et al., 2009)). It is therefore of pivotal importance to design robust and efficient techniques to manipulate the inherent flow behaviour. Flow control is the field which deals with such problem. Among the different control strategies, we can distinguish two main categories (Rowley and Williams, 2006; Choi et al., 2008): (i) *passive control*, and (ii) *active control*.

1.2.1 Passive control

Passive control aims at modifying the flow behaviour by shape modifications or by introducing passive elements into the flow. Some examples of passive control used in fluid dynamics applications are the addition of vortex generators to control boundary layer separation (Lin, 2002; Godard and Stanislas, 2006), the placement of a small cylinder upstream of a cavity (Illy et al., 2004) or in the near wake of a cylinder (Strykowski and Sreenivasan, 1990), or the use of roughness or dimples to control the flow behind a cylinder (Shih et al., 1993; Bearman and Harvey, 1993) or a separated boundary layer (Boiko et al., 2008).

Techniques to compute the sensitivity of the eigenvalues to base-flow modifications have been proposed for laminar (Bottaro et al., 2003; Giannetti and Luchini, 2007; Marquet et al., 2008) and turbulent flows (Meliga et al., 2012; Mettot et al., 2014a,b). For noise-amplifier flows, the sensitivity of the singular values to base-flow modifications has been studied by Brandt et al. (2011). All these techniques are of great interest for the design and evaluation of passive control strategies.

Passive control strategies are easy to implement due to the absence of moving devices (actuators). However, this implies that the control is designed for a specific flow configuration and cannot adapt to possible changes in the flow state.

1.2.2 Active control

Contrary to the passive approach, active control requires the supply of energy to the system via an actuator. More aggressive control strategies can be implemented. The supplementary cost of active control is generally justified by a positive energetic balance: the energy saving obtained by the control system should be larger than the energy required. Examples of actuators used in flow control applications include plasma devices, moving objects and small jets among others (see Cattafesta III and Sheplak (2011) for a review on the subject).

Active control can be classified into two categories: (i) open-loop control, and (ii) closed-loop control. Open-loop control implements a control law which is determined off-line. We can cite for instance, the work by (Tokumaru and Dimotakis, 1991; He et al., 2000; Protas and Wesfreid, 2002), where the authors show that the rotatory movement of a cylinder significantly improves its aerodynamic performance. Another example is Sipp (2012), where it is showed that a global mode in a cavity may effectively be stabilized by harmonic forcing.

On the other hand, closed-loop control uses measurements extracted in real time from the flow to produce a relevant control action. This strategy may adapt to flow changes and, thus, more efficient and robust control systems are expected (Kim and Bewley, 2007). However, closed-loop control generally requires the computation of a model of the flow and of the actuators, which is a challenging problem for flow applications (Section 1.3).

Genetic algorithms are a recent attempt to obtain model-free closed-loop controllers (Parezanović et al., 2015; Gautier et al., 2015). This technique explores a wide range of control laws and determines the optimum by minimizing a cost function. However, the controllers obtained in such a way do not guarantee any stability robustness and may lead to unstable compensated systems if the design conditions are modified.

Closed-loop control has been widely applied to noise amplifier flows. The motivation of these studies was the delay of laminar-turbulent transition by suppressing the linear transient growth of small perturbations (Joshi et al., 1997; Bewley and Liu, 1998; Högberg and Henningson, 2002; Hogberg et al., 2003; Chevalier et al., 2007; Monokrousos et al., 2008; McKernan et al., 2009a,b), the relaminarization

of turbulent flows (Högberg et al., 2003; Sharma et al., 2011), and the reduction of drag of turbulent channels (Cortelezzi et al., 1998; Lee et al., 2001).

1.3 Modelling

The high number of degrees of freedom of fluid systems (often $\mathcal{O}(10^6)$) are far beyond the capabilities of current control strategies, which typically can handle $\mathcal{O}(10^2)$ variables. As a consequence, the full fluid system has to be properly reduced, before a controller can be designed for the reduced-order model (ROM). Three different strategies are commonly considered to obtain ROMs of the flow: (i) simplified physical models, (ii) the projection of the Navier-Stokes equations onto reduced bases, and (iii) system identification techniques.

The first strategy consists in tuning simple physical models of the flow to match experimental data. This approach has been successfully used to model the flow over a cavity (Rowley et al., 2006; Illingworth et al., 2012), and behind a turbulent bluff body (Rigas et al., 2015). However, this approach requires a deep physical understanding of the flow. Projection and identification techniques are more general and systematic strategies and are introduced in Section 1.3.1 and Section 1.3.2, respectively.

Recently, full-order optimal controllers and estimators have been obtained for a two-dimensional boundary layer over a flat plate using a Ricatti-less approach (Semeraro et al., 2013a). The full- and reduced-order compensators turned out to be in good agreement when a feed-forward control strategy was used.

1.3.1 Galerkin projection

The most popular approach to obtain ROMs of fluid systems is the Galerkin projection of the Navier-Stokes equations onto reduced-bases which capture the most important features of the system dynamics. The choice of the reduced basis is of great importance since it will determine the quality of the ROM. Three projection bases have mainly been employed in fluid dynamics applications: (i) global modes, (ii) proper orthogonal decomposition (POD)-modes, and (iii) balanced proper orthogonal decomposition (BPOD)-modes.

The global modes are the eigenvectors of the linearized Navier-Stokes operator (see Sipp et al. (2010)). By construction, global modes are related to the open-loop dynamics of the flow of interest without any information about actuators and sensors. For that reason, their efficiency as a projection basis for control-oriented reduced-order models is questionable. Examples of closed-loop control applications using global-modes-based ROMS include Åkervik et al. (2007), Ehrenstein et al. (2011) and Barbagallo et al. (2011).

POD-modes (Lumley, 1967; Sirovich, 1987) are a popular choice for reduced-order basis since this decomposition minimizes the averaged residual in the energy norm for a given number of modes. See for instance the work by Aubry et al. (1988) where the coherent structures of a turbulent boundary layer have been modelled using this approach. However, reduced-order models using Galerkin projection onto POD-modes may be unstable (Ma and Karniadakis, 2002). Different strategies have been considered to improve these models; we can cite for instance the addition of "shift modes" and stability modes (Noack et al., 2003), the addition of a pressure term (Noack et al., 2005) or a spectral viscosity (Sirisup and Karniadakis, 2004), the calibration of the model coefficients (Galletti et al., 2004; Bergmann et al., 2009), or, recently, the use of a discrete empirical interpolation method (DEIM) (Chaturantabut and Sorensen, 2010; Fosas de Pando et al., 2013). Examples of flow control results based on reduced-order models designed with POD modes may be found in Bergmann et al. (2005); Bergmann and Cordier (2008); Weller et al. (2009) and in the experimental work of Samimy et al. (2007).

Reduced-order models with better properties are obtained by projecting the equations onto a balanced basis and a subsequent truncation of the degrees of freedom. In systems theory, a balanced realization implies that the degree of reachability and the degree of observability of each state are the same (Moore, 1981). Reduced-order models obtained by balanced truncation present a priori bounds for the error and preserve stability. Balanced truncation, however, is not computationally feasible for very large systems using the Gramians (Antoulas, 2005). An alternative algorithm based on snapshots was proposed by Willcox and Peraire (2002) and Rowley (2005). This technique, referred to as balanced proper orthogonal decomposition (BPOD), has been successfully applied in the control of a channel flow (Ilak and Rowley, 2008), the vortex shedding behind a plate (Ahuja and Rowley, 2010), a boundary layer over a flat plate (Bagheri et al., 2009; Semeraro et al., 2011), or the flow over a cavity (Barbagallo et al., 2009).

Finally, it is worth to say that a ROM obtained by using BPOD in the time domain only provides the information between a given input and all the outputs of the system. However, noise-amplifier flows are driven by the external sources of noise which are generally unknown and, consequently, an input of the system cannot be defined. An alternative approach is a frequency-domain formulation of the BPOD which allows to recover the transfer-function between all the inputs and all the outputs (Dergham et al., 2011a,b, 2013).

1.3.2 System identification

An alternative approach to Galerkin projection is system identification (Ljung, 1999). System identification techniques represent a family of algorithms that efficiently determine the coefficients of an underlying model directly from observed input–output data via a statistical learning process.

Examples of applications of system identification techniques to fluid dynamics include the control of a separated flow using ARX models (Huang and Kim, 2008), ARMARKOV models to suppress thermoacoustic oscillations (Lacy et al., 1998), or frequency-domain identification to reduce the pressure drag of a turbulent backward-facing step (Dahan et al., 2012).

System identification techniques are better suited for noise-amplifier flows than Galerkin projection. The reason is that projection techniques require detailed knowledge of the spatial distribution of the upstream noise sources. This requirement imposes great limitations, especially in experimental situations, where information about the noise environment is neither directly nor sufficiently available. In contrast, system identification only requires the input-output data measured by sensors. Hervé et al. (2012) used an ARMAX model for the control of a numerical backward-facing step. This strategy was successfully extended by Gautier and Aider (2014) to an experimental configuration. Recently, subspace identification was employed to compute state-space models of numerical (Juillet et al., 2013) and experimental channel flows (Juillet et al., 2014).

The eigensystem realisation algorithm (ERA) is an identification technique which yields a ROM of the model which is theoretically equivalent to a model obtained by BPOD (Juang and Pappa, 1985; Ma et al., 2011). This technique has been widely applied to fluid systems: the flow over a cavity (Illingworth et al., 2011),

or two-dimensional (Belson et al., 2013) and three-dimensional (Semeraro et al., 2013a) boundary layers. ERA requires to apply an impulse-response to the system and, consequently, is not well-suited for experimental noise-amplifier flows for the reasons previously stated.

1.4 Objectives of this thesis and outline

The aim of this thesis is to provide new modelling strategies for *noise-amplifier flows* using *data-based* approaches (system identification). The existing techniques (Hervé et al., 2012; Juillet et al., 2013) determine the dynamics from an estimation sensor and an actuator to a performance sensor. A control law which minimizes the root-mean-square signal (rms) of the performance sensor is then computed. Either the estimation and performance sensors are localized measurements. In our case, we extend this approach: the inputs of the system are again the estimation sensor and the actuator, but the output is the full velocity field. This technique allows to directly target the velocity field as the objective of the control. Moreover, the estimation performance obtained by our estimator is proven to be far superior to existing data-based techniques (linear stochastic estimation (LSE) (Adrian, 1979)) when dealing with convective flows. It is worth to say that the spirit of this thesis is to propose techniques that can be used in experiments, although they were developed using numerical simulations.

This thesis is organised as follows. Chapter 2 presents a technique to compute a model for noise amplifiers based solely on data which may be readily available in experiments. This technique is illustrated on a two-dimensional boundary layer over a flat plate. The performance of the model was compared with respect to a classical data-based estimator (LSE). Finally, the model was used in an optimal closed-loop control framework to reduce the amplitude of the perturbations. This chapter is presented in the form of an article published in the *Journal of Fluid Mechanics* (Guzmán Iñigo et al., 2014). In Chapter 3, the model was used to determine the intrinsic dynamics of the flow: the global modes of the ROM were computed showing good qualitative agreement with the global modes of the full-order system. This chapter is also presented as an article submitted to the *Journal of Fluid Mechanics*. In Chapter 4, the performance of the data-based estimator is assessed with respect to an optimal estimator (reduced-order Kalman

filter obtained from the exact equations). Chapter 5 provides guidelines for a future experimental implementation of the model. Finally, a summary of results and conclusions is given in Chapter 6.

Chapter 2

A dynamic observer to capture and control perturbation energy in noise amplifiers

This chapter is presented in the form of a self-contained article published in the *Journal of Fluid Mechanics* (Guzmán Iñigo et al., 2014). In this article, we introduce a technique to obtain a reduced-order estimator of a noise-driven amplifier flow. An estimator of the flow is a system which aims at approximating as best as possible the state of the flow based solely on the limited information given by a sensor. A classical procedure to obtain estimators in fluid dynamics applications consists of the reduction of the degrees of freedom of the system by a Galerkin projection and the computation of a Kalman filter by solving a Riccati equation of the reduced-order model (ROM). However, this approach is not well-suited for noise amplifiers since the external driving term is unknown in experimental situations. This chapter aims at providing an alternative technique to obtain an estimator of the flow solely based on input-output data which is readily available in experimental setups.

Abstract

In this article we introduce techniques to build a reduced-order model of a fluid system which accurately predicts the dynamics of a flow from local wall measurements. This is particularly difficult in the case of noise amplifiers where the

upstream noise environment, triggering the flow via a receptivity process, is not known. A system-identification approach, rather than a classical Galerkin technique, is used to extract the model from time-synchronous velocity snapshots and wall-shear stress measurements. The technique will be illustrated on the case of a transitional flat-plate boundary layer, where the snapshots of the flow are obtained from direct numerical simulations. Particular attention is directed to limiting the processed data to data that would be readily available in experiments, thus making the technique applicable to an experimental setup. The proposed approach combines a reduction of the degrees of freedom of the system by a projection of the velocity snapshots onto a POD basis combined with a system-identification technique to obtain a state-space model. This model is then used in a feedforward control setup to significantly reduce the kinetic energy of the perturbation field and thus successfully delay transition.

2.1 Introduction

Fluid systems that fall under the category of noise amplifiers are characterized by a globally stable spectrum despite the presence of convective instabilities. Boundary layers are examples of this type of fluid behavior. External perturbations permeate the near-wall region during the receptivity phase and initiate disturbances that are amplified into Tollmien-Schlichting waves as they are swept downstream. If these instabilities reach sufficient amplitudes, breakdown of the flow into turbulent fluid motion can occur. Much effort has been expended to understand and control this breakdown into turbulence by manipulating the underlying instability processes.

While many open-loop control techniques have been developed to delay the transition process, closed-loop approaches, where actuation depends on sensor measurements, are more effective and efficient (Kim and Bewley, 2007). However, under realistic flow conditions, the direct application of closed-loop control techniques is often not tractable. The high degrees of freedom of fluid systems (often $\mathcal{O}(10^6)$) are far beyond the capabilities of current control devices which typically can handle $\mathcal{O}(10^2)$ variables. As a consequence, the full fluid system has to be properly reduced, before a controller can be designed for the reduced-order model. This methodology has been demonstrated to yield successful control designs, see Bagheri et al. (2009) and Barbagallo et al. (2009), among others. In these investigations, model reduction is accomplished by a flow decomposition (e.g., POD or

BPOD decomposition) followed by a Galerkin projection of the equations onto the reduced basis.

In the case of noise amplifiers, external perturbations strongly influence the system dynamics. Thus, it is very important for the reduced-order model (ROM) to accurately capture the noise environment. In particular, ROMs obtained by means of Galerkin projections require detailed knowledge of the spatial distribution of the upstream noise sources. This requirement imposes great limitations, especially in experimental situations where information about the noise environment is neither directly nor sufficiently available. A promising alternative to control design based on Galerkin projections derives from system-identification techniques as proposed in Hervé et al. (2012); this approach also constitutes an encouraging step towards the control of noise amplifiers in experimental situations.

This paper intends to provide a methodology to obtain reduced-order estimators for noise amplifiers without using Galerkin projections. While in Hervé et al. (2012) the model describes only the dynamics between one sensor (upstream measurement) to another (downstream measurement), here we aim to capture the dynamics between upstream measurements and the *entire* perturbation field. This will allow the reconstruction of the full flow field and, consequently, the design of controllers that target the kinetic energy of the full perturbation field, not only the variance of a wall-measurement signal. This reminds the Galerkin-based output projection technique introduced by Rowley (2005) that captures the full perturbation field from a given input. However, the latter technique requires precise knowledge of the spatial distribution of the input, which is generally not available in amplifier flows. Therefore, Dergham et al. (2013) has extended it to also account for any possible input, so as to obtain a model that captures any input to any output. In the present work, we aim at obtaining a similar model — capturing the dynamics from unknown input to any output — but with identification methods. The proposed approach consists of a reduction of the degrees of freedom of the system by (i) a projection of the velocity fields onto a reduced basis combined with (ii) a system-identification algorithm to obtain the dynamic operators of a reduced-order system. In particular, a link between velocity fields (e.g., from TR-PIV data) and time-synchronous wall-shear stress measurements is established, and a dynamic observer is determined. A key feature of our procedure is its reliance on a Galerkin model *structure* but on the determination of the

model matrices by system identification rather than integral expressions (Galerkin projections).

The link between velocity fields and wall measurements is reminiscent of linear stochastic estimation (LSE) techniques (Adrian, 1979; Guezennec, 1989; Bonnet et al., 1994; Tinney et al., 2006; Hudy et al., 2007; Taylor and Glauser, 2004; Tu et al., 2013) where multiple, measured inputs are correlated to simultaneous, multiple outputs by averaging over many realizations. Our proposed technique generalizes this *static* approach by accounting for the *dynamics* of either measurement data. The comparison between LSE and dynamic observers obtained by Galerkin projection has already been considered in Rowley and Juttijudata (2005) showing the superiority of dynamic estimators. A further relation can be demonstrated to data-assimilation techniques, specifically, to the online variant (see, e.g., Lewis et al., 1989) where streaming data are matched to an underlying model which is then used to predict future measurement signals. Once a model has been extracted by our technique from measured data, it can straightforwardly be used in a closed-loop control application, as will be illustrated below.

The present study is structured as follows. After a brief description of the flow configuration and the governing equations (§ 2.2) we present a dynamic observer obtained by Galerkin projection (§ 2.3) and by the identification procedure (§ 2.4). § 2.5 will compare the identified observer with different well-known approaches, while § 2.6 will demonstrate how to include the identified model in a control framework. A summary of results and conclusions are given in § 2.7. The appendix gives details about the employed subspace system identification techniques.

2.2 Problem formulation

2.2.1 Governing equations

We choose a zero-pressure gradient boundary layer — a classical and generic flow that acts as a noise amplifier — as our configuration to design and test the dynamic observer. This flow is globally stable but selectively amplifies upstream disturbances by convective instabilities. In a low-amplitude noise environment, two-dimensional Tollmien-Schlichting waves appear as a result of this instability mechanism.

We consider the dynamics of disturbances $\mathbf{u}$ around a base-flow $\mathbf{U}_0$, which we take as a Blasius boundary layer. The disturbances $\mathbf{u}$ are additionally driven by an external forcing term, $\mathbf{F}_w w(t)$, which acts as an upstream disturbance source of unknown origin. For simplicity, we assume that $w(t)$ is a random process of zero mean and variance W, while $\mathbf{F}_w$ describes a spatial two-dimensional Gaussian distribution centered at (x_w, y_w) of spread (σ_x, σ_y) and amplitude A. The spatio-temporal evolution of the total flow field, $\mathbf{U}_{\text{tot}} = \mathbf{U}_0 + \mathbf{u}$, is governed by the incompressible Navier-Stokes equations, augmented by a forcing term,

$$\partial_t \mathbf{U}_{\text{tot}} + \mathbf{U}_{\text{tot}} \cdot \nabla \mathbf{U}_{\text{tot}} = -\nabla P_{\text{tot}} + Re_{\delta_0^*}^{-1} \Delta \mathbf{U}_{\text{tot}} + \mathbf{F}_w w(t), \qquad \nabla \cdot \mathbf{U}_{\text{tot}} = 0. \quad (2.1)$$

The variables are non-dimensionalized using the displacement thickness δ_0^* of the boundary-layer at the computational inlet ($x_0 = 0$) and the free-stream velocity U_∞. Consequently, the Reynolds number is defined as $Re_{\delta_0^*} = U_\infty \delta_0^* / \nu$. All simulations were performed at $Re_{\delta_0^*} = 1000$, which ensures the presence of strong Tollmien-Schlichting instabilities since $Re_{\delta_0^*} > Re_{\delta^*}^{\text{crit}} = 520$.

The governing equations (2.1) are solved in a computational domain Ω of size $(0, 1000) \times (0, 40)$, sketched in figure 2.1. A Blasius profile of unit displacement thickness is prescribed at the left boundary, outflow conditions are employed at the upper and right boundaries, and a no-slip condition is imposed at the wall. We use the spectral-element code `Nek5000` (see https://nek5000.mcs.anl.gov) to perform the computations below.

With the base flow $\mathbf{U}_0$ as a solution of the unforced ($w = 0$) steady Navier-Stokes equations (2.1), the perturbations $\mathbf{u}$ are governed by the following equations

$$\partial_t \mathbf{u} + \mathbf{U}_0 \cdot \nabla \mathbf{u} + \mathbf{u} \cdot \nabla \mathbf{U}_0 = -\nabla p + Re_{\delta_0^*}^{-1} \Delta \mathbf{u} + \mathbf{F}_w w(t), \qquad \nabla \cdot \mathbf{u} = 0, \quad (2.2)$$

where the nonlinear term $\mathbf{u} \cdot \nabla \mathbf{u}$ has been omitted since only low-amplitude noise $W \ll 1$ will be considered. This assumption ensures linear perturbation dynamics, as well as a linear response to the noise w. During the DNS simulations, white noise is imposed via $w(n)$ to mimic upstream excitations of unknown source and distribution (mimicking conditions in physical experiments). We use a time-step of $dt_{\text{dns}} = 0.1$.

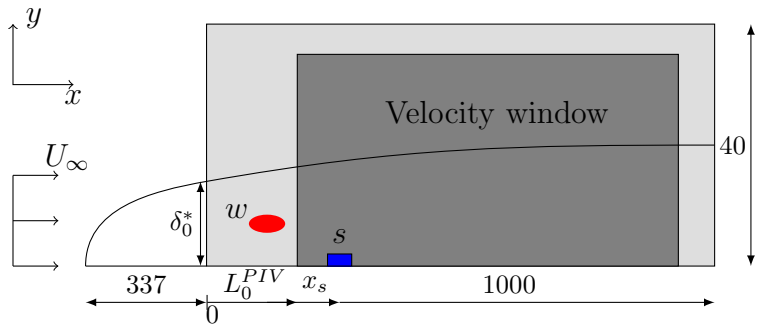

FIGURE 2.1: Sketch of the flow configuration. The computational domain Ω is of size $(0, 1000) \times (0, 40)$, represented by the light gray box. The upstream receptivity of the boundary layer to external perturbations is modeled by the noise w which is placed at $(x_w, y_w) = (50, 0.95)$. A sensor located at $(x_s, y_s) = (200, 0)$ will identify incoming perturbations, while a velocity window (represented by the dark gray box) is used to quantify the effect of the forcing on the velocity field.

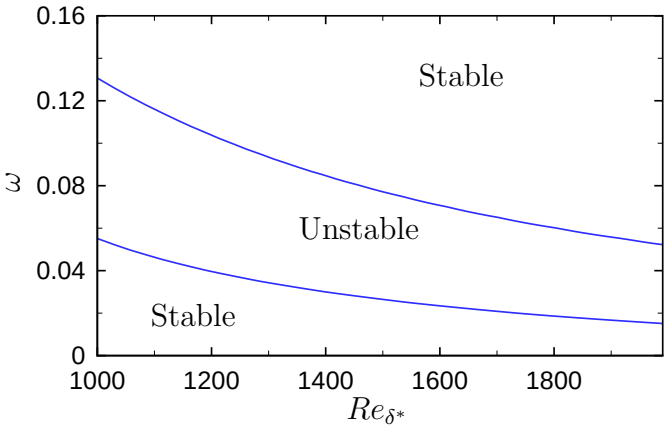

FIGURE 2.2: Neutral curve obtained by a local spatial stability analysis in the computational domain.

2.2.2 Perturbation dynamics

Choosing the Blasius boundary layer as an example of a noise amplifier and assuming a low-noise environment, perturbations may be amplified by two different instability mechanisms: (i) the Tollmien-Schlichting instability which takes advantage of a critical layer as well as a wall layer to generate a non-zero Reynolds stress, and (ii) the Orr instability where initial perturbations lean against the mean shear but grow in amplitude as they are tilted by the mean velocity (Butler and Farrell, 1992). The details of these mechanisms can be studied within a local stability framework, considering perturbations of the form $e^{i(\alpha x - \omega t)}$, with ω as the frequency and α as the streamwise wavenumber of the perturbation. An analysis of this type shows that the Blasius boundary layer is convectively unstable to

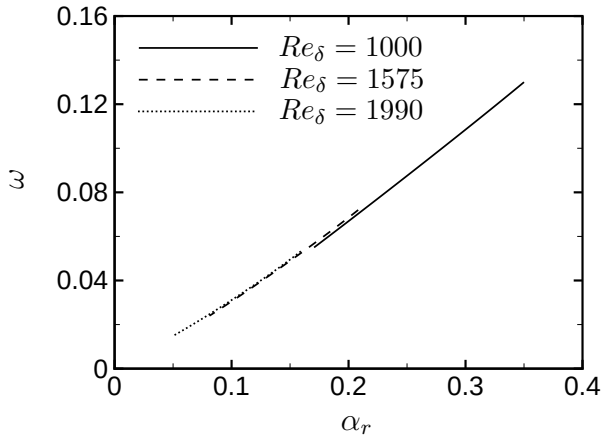

FIGURE 2.3: Spatial dispersion relation for the convectively unstable frequencies at three different positions within the domain.

Tollmien-Schlichting waves when the Reynolds number based on the local displacement thickness $\delta^*(x)$ is larger than the critical value of $Re = 520$. In figure 2.2, the neutral curve obtained from a local spatial stability analysis performed with wall-normal profiles extracted from the base flow $\mathbf{U}_0$ is displayed. The unstable frequencies fall in the interval $0.055 < \omega < 0.13$ at the computational inlet and $0.015 < \omega < 0.052$ at the end of the domain. When a localized disturbance is placed inside the boundary layer, the response is a wavepacket which convects downstream at the local group velocity $v_g = d\omega/d\alpha$. The group velocity is a very important parameter, as it sets a characteristic time for the perturbation, and can easily be obtained from the dispersion relation $\omega = \omega(\alpha)$. In figure 2.3, the dispersion relation is represented for three different Reynolds numbers (corresponding to streamwise locations at the computational inlet, middle and outlet). For the considered configuration, the group velocity is estimated as $v_g \approx 0.375 U_\infty$ using the real-axis approximation.

2.2.3 Measurements

This paper aims at providing a data-based technique that is applicable in an experimental setting. For this reason, special care must be taken to only use data which is readily available in an experiment. We first consider a wall-friction sensor s (see figure 2.1), located at $x_s = 200$ and of spatial extension in the streamwise

direction $\Delta x = 0.5$, which measures the wall shear-stress:

$$s_{\text{tot}} = \int_{x_s}^{x_s+\Delta x} \left.\frac{\partial u_{\text{tot}}}{\partial y}\right|_{y=0} dx + g = \int_{x_s}^{x_s+\Delta x} \left.\frac{\partial U_0}{\partial y}\right|_{y=0} dx + \underbrace{\int_{x_s}^{x_s+\Delta x} \left.\frac{\partial u}{\partial y}\right|_{y=0} dx + g}_{s(t)}, \tag{2.3}$$

where s denotes the fluctuating part of the measurement, which may be obtained by subtracting the time-averaged value of s_{tot} from the signal s_{tot}. For the case of low-amplitude forcing, i.e., for linear perturbation dynamics, the time-averaged value also corresponds to the base-flow value. The sensor s_{tot} (or s) may be corrupted by white noise g, of variance G (with G small and of the order of magnitude of W).

In addition to the wall-friction sensor s, we also consider velocity snapshots $\mathbf{u}_{\text{snap}}$ in a given domain Ω_{snap}, which may be chosen smaller than the computational domain Ω (see figure 2.1). The fluctuating parts of the velocity field may again be obtained by subtracting the time-averaged snapshots from the total snapshot sequence. In an experimental setup, the velocity snapshots may be obtained by a PIV technique. In what follows, we will consider time-series of composite skin-friction measurements and velocity snapshots.

2.3 Structure of a dynamic observer using Galerkin projection

In this section the model reduction technique based on Galerkin projection will be briefly discussed to motivate the use of identification methods in the design of reduced-order models (ROMs). Special attention will be paid to the structure of the resulting model since it will form the basis of the system-identification approach. We proceed by developing and analyzing the ROM that would result from a projection of the linearized Navier-Stokes equations onto a POD basis (§ 2.3.1) which is followed by the introduction of a Kalman filter allowing us to replace the unknown driving term $w(t)$ by the known measurements $s(t)$ (§ 2.3.2).

2.3.1 Reduced-order model with Galerkin projection by approximation of the controllability Gramian

A common method used to obtain a reduced-order model of a dynamical system is based on Galerkin projection, i.e., a projection of the Navier-Stokes equations (2.2) onto an appropriate basis, such that the input-output behavior of the full system is preserved as accurately as possible. The choice of basis is critical. The two most common options are based on: an approximation of the controllability Gramian which yields a POD basis (Rowley, 2005; Barbagallo et al., 2009) that maximizes the energy captured by the reduced-order model, and an approximation of the controllability and observability Gramians which yields a balanced basis (Moore, 1981; Rowley, 2005; Bagheri et al., 2009) that directly focuses on the input-output relation of the reduced system. In this article, only ROMs obtained by approximating the controllability Gramian will be considered.

After extracting the POD modes (taking data from the full computational domain) from the approximation of the controllability Gramian by an impulse response of the full system (see Barbagallo et al. (2009) for details), the governing equations (2.2) are projected onto the first k modes to obtain a reduced state-space representation of the system according to

$$\frac{d\mathbf{X}}{dt} = \mathsf{A}'_w \mathbf{X}(t) + \mathbf{B}'_w w(t), \tag{2.4a}$$

$$s(t) = \mathbf{C}'_s \mathbf{X}(t) + g(t). \tag{2.4b}$$

where $\mathbf{X}(t)$ is a vector containing the k POD coefficients at time t. Denoting by $\langle \cdot \rangle$ the energy based-inner product that has been used to extract the POD modes, the components of the matrix A'_w and of the vectors $\mathbf{B}'_w$, $\mathbf{C}'_s$ are obtained as follows: $\mathsf{A}'_{w,ij} = \langle \mathbf{\Phi}_i, \mathscr{A}\mathbf{\Phi}_j \rangle$ (with $\mathscr{A}$ as the linearized Navier-Stokes operator (2.2) on Ω), $\mathbf{B}'_{w,i} = \langle \mathbf{\Phi}_i, \mathbf{F}_w \rangle$ and $\mathbf{C}'_{s,i} = \mathscr{C}_s \mathbf{\Phi}_i$ (with $\mathscr{C}_s$ as the measurement operator).

A Galerkin projection usually provides a continuous-time format for the state-space system (2.4). With the remaining article pertaining to system identification methods, it is more convenient to express the governing equations in a discrete-time framework. In the discrete-time domain, the mapping of the state-vector $\mathbf{X}$ from time t (index n) to $t + \Delta t$ (index $n + 1$) reads

$$\mathbf{X}(n+1) = \mathsf{A}_w \mathbf{X}(n) + \mathbf{B}_w w(n), \tag{2.5a}$$

$$s(n) = \mathbf{C}_s \mathbf{X}(n) + g(n), \tag{2.5b}$$

with $\mathbf{B}_w = \int_0^{\Delta t} \exp[\mathsf{A}'_w(\Delta t - \tau)]\mathbf{B}'_w \, d\tau$ associated with the discrete driving term, $\mathsf{A}_w = \exp(\mathsf{A}'_w \Delta t)$ denoting the evolution matrix over a time interval Δt and $\mathbf{C}_s = \mathbf{C}'_s$.

2.3.2 Kalman filter

When dealing with noise amplifiers, it is critical to accurately account for the disturbance environment, as it both triggers and sustains the dynamics of the system. Despite this requirement, in an experimental setup, access to accurate information about the noise environment is, at best, very difficult or, in most cases, impossible. We thus have to introduce an observer where the noise source-term $\mathbf{B}_w w(t)$ is replaced by a measurement term $\mathbf{L}s(t)$ which drives, as best as possible, the estimated state of the system. Formally, the observer may be obtained in a straightforward manner by introducing a linear estimator of the form

$$\mathbf{X}_e(n+1) = \mathsf{A}_w \mathbf{X}_e(n) + \mathbf{L}\left[s(n) - \mathbf{C}_s \mathbf{X}_e(n)\right] = \mathsf{A}_s \mathbf{X}_e(n) + \mathbf{L}s(n), \tag{2.6}$$

where $\mathbf{X}_e(n)$ is the estimated state, $s(n)$ is the measurement signal from the friction sensor (defined by (2.3)) and $\mathbf{L}$ represents the gain of the estimator which can be selected by the designer to achieve different objectives. If the gain $\mathbf{L}$ is selected to statistically minimize the error $\|\mathbf{X}_e - \mathbf{X}\|_2$, the estimator is referred to as a Kalman filter and $\mathbf{L}$ is obtained by solving a Riccati equation (see Burl (1999)) of the form

$$\mathsf{P} = \mathsf{A}_w \mathsf{P} \mathsf{A}_w^* - \mathsf{A}_w \mathsf{P} \mathbf{C}_s^* \left(\mathbf{C}_s \mathsf{P} \mathbf{C}_s^* + G\right)^{-1} \mathbf{C}_s \mathsf{P} \mathsf{A}_w^* + \mathbf{B}_w W \mathbf{B}_w^*, \tag{2.7a}$$

$$\mathbf{L} = \mathsf{A}_w \mathsf{P} \mathbf{C}_s^* \left(\mathbf{C}_s \mathsf{P} \mathbf{C}_s^* + G\right)^{-1}. \tag{2.7b}$$

In short, the dynamic observer (2.6) consists of a linear relationship between two subsequent state-vectors $\mathbf{X}_e(n+1), \mathbf{X}_e(n)$ and the measurement $s(n)$. Its dynamics are fully determined by the evolution matrix $\mathsf{A}_s = \mathsf{A}_w - \mathbf{L}\mathbf{C}_s$ and the observer gain

L. We stress that this estimator is effective, only if the measurement s remains constant over the sampling time Δt; for this reason, a spectral analysis of the measurement s must be employed to determine its frequency content and thus the sampling time Δt.

2.3.3 Limitations of Galerkin-based methods

Galerkin models based on Gramians are a popular choice for model reduction, owing to their ease of use in feedback applications, the availability of mathematical bounds on their convergence, and their link to physically relevant flow structures. But despite their wide-spread use, Galerkin-based methods for the computation of reduced-order models suffer from notable limitations when they are applied to experimental situations.

The favorable properties of the Galerkin model presented in this section stem from the fact that the POD modes were obtained by accurately discretizing the integral involved in the controllability Gramian. This requires that an impulse of $w(t)$ can be generated and its response can be analyzed using velocity snapshots; furthermore, a very small delay between two successive snapshots and a very long series of snapshots is desirable. If such requirements are not met, Galerkin projection then provides POD-based models which may even become unstable: *a posteriori* regularization and calibration techniques are then required to render the models stable again (Bergmann et al. (2009)).

One of the most important limitations of Galerkin-based models is linked to the requirement of a very accurate distribution of the noise sources in the experiment for amplifier flows, since these sources will drive the dynamics of the system. Generally, the noise distribution in experimental setups will be complex, difficult to represent, and mostly unknown, so that triggering by an impulse in $w(t)$ is nearly impossible.

2.4 Dynamic observer using system-identification techniques

This section introduces an alternative method to obtain a dynamic observer. We will present a data-driven approach, based on system identification techniques, that solely relies on observations of the system in the presence of unknown upstream noise $w(t)$. System identification techniques represent a family of algorithms which efficiently determine the coefficients of an underlying model directly from observed input-output data via a statistical learning process. This section aims at obtaining a dynamic observer model such as Eq. (2.6) directly from observations of the system. In the following, we will first briefly recall the basics of system identification techniques, which generate a model governing the dynamics of given outputs from known inputs (§2.4.1). Second, we will define the output of our system as the coefficients of the velocity snapshots in a POD basis (§2.4.2). Third, we will introduce the model structure of the dynamic observer (§2.4.3), identify the coefficients of the model (§2.4.4) and validate the model (§2.4.5). Finally, the influence of various parameters on the quality of the model will be assessed (§2.4.6).

2.4.1 System identification based on subspace techniques

System identification comprises a wide range of methods of varying applicability and complexity (see Ljung (1999)). In our case, we aim at obtaining a linear time-invariant (LTI) multiple-input-multiple-output (MIMO) system, such as the one given in Eq. (2.6). In general, we have $u(n)$ as known inputs, $w(n)$ as unknown white plant noise and $y(n)$ as known outputs corrupted by unknown white noise $v(n)$. We aim at determining the system matrices ($\mathcal{A}, \mathcal{B}, \mathcal{C}$ and $\mathcal{D}$), which govern a state $x(n)$ such that

$$x(n+1) = \mathcal{A}x(n) + \mathcal{B}u(n) + w(n), \tag{2.8a}$$

$$y(n) = \mathcal{C}x(n) + \mathcal{D}u(n) + v(n). \tag{2.8b}$$

The coefficients of the system matrices are chosen such that the estimated output $y_e(n)$, obtained by time-marching (2.8) with $w(n) = v(n) = 0$, is as close as

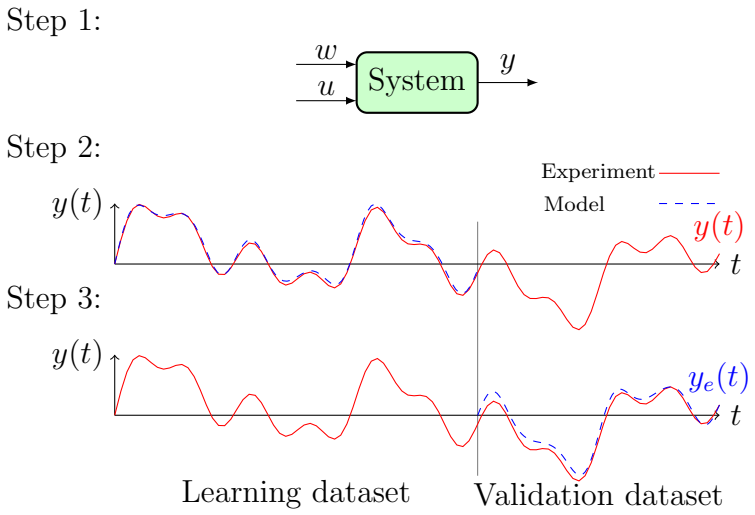

FIGURE 2.4: Procedural steps of system identification techniques. Step 1: The system is forced with a frequency-rich input signal and data is acquired. The forcing term $w(n)$ driving the system should be either known, or replaced by a known proxy measurement $s(n)$. Step 2: After selecting a model structure and appropriate parameters, the model coefficients are then computed by maximizing the fit between the output of the system and the prediction of the model for a part of the available data. Step 3: The model is tested on a dataset different than the one used for learning. If the model does not reproduce the system dynamics with the required accuracy, a different model structure, a different parametrization or even a different experiment should be considered.

possible to the measured output $y(n)$ (subject to the white-noise sources $w(n)$ and $v(n)$), knowing the inputs $u(n)$. We stress that the state $x(n)$ does not necessarily have to have a physical interpretation.

System identification consists of three procedural steps (see figure 2.4). First, the system is excited by known and unknown input signals $u(n)$ and $w(n)$ while the outputs $y(n)$ (corrupted by noise $v(n)$) are recorded. In a second step, a parametrized model is chosen, in our case a LTI system characterized by the system matrices $\mathcal{A}, \mathcal{B}, \mathcal{C}$ and $\mathcal{D}$, together with an appropriate identification algorithm. A subsample of the full data set, referred to as the learning dataset, is then processed to determine the system matrices of the model. In a third step, a different part of the data, known as the testing dataset, is used to drive the identified system, and the output $y_e(t)$ produced by the model is compared to the measured true output $y(t)$; based on this validation test, the model is accepted, adapted or rejected.

The form of the model given in (2.8) makes subspace identification algorithms a convenient choice. Appendix A presents a brief introduction to these techniques; a more comprehensive description is given in Qin (2006) and Van Overschee and

De Moor (1996). In this study, the `N4SID` algorithm (Van Overschee and De Moor, 1994) has been used to obtain all the models.

2.4.2 Outputs as coefficients of velocity snapshots in a POD basis

We would like to describe the system at each time instant with velocity snapshots $\mathbf{u}_{\text{snap}}$. The large number of degrees of freedom in these snapshots makes direct application of identification techniques excessively, or prohibitively, expensive. It is thus necessary to reduce the dimensionality of the measured data. In this article, we use the proper orthogonal decomposition (POD) modes (Lumley, 1967; Sirovich, 1987) to form a reduced basis. Note that, contrary to the previous section, the velocity snapshots used to build the POD basis are obtained in the presence of the true, but unknown, noise environment $w(t)$.

We consider a sequence of m velocity snapshots $\{\mathbf{V}_{\text{snap}}(n)\}_{n=1..m}$ extracted from the Ω_{snap}-domain and containing the effect of upstream noise w. The sequence needs to cover a sufficiently large time range to explore all states of the system. Therefore, even though not mandatory, the time-delay between two snapshots can be taken as quite large, so as to obtain nearly uncorrelated successive snapshots. The proper orthogonal decomposition then enables us to compute a ranked orthonormal basis $\{\mathbf{\Phi}_i\}_{i=1..m}$ of flow fields, satisfying $\langle \mathbf{\Phi}_i, \mathbf{\Phi}_j \rangle = \delta_{ij}, \quad i,j = 1,2,...,m$, which can be expressed most conveniently as a linear combination of these m snapshots. Here, the scalar-product $\langle \cdot \rangle$ is associated with the energy-based inner product: $\left\langle \mathbf{u}^1_{\text{snap}}, \mathbf{u}^2_{\text{snap}} \right\rangle = \int_{\Omega_{\text{snap}}} (u^1_{\text{snap}} u^2_{\text{snap}} + v^1_{\text{snap}} v^2_{\text{snap}})\, dx\, dy$. Any velocity field $\mathbf{V}$ in Ω_{snap} can then be projected onto the first k POD modes according to

$$y_i = \langle \mathbf{\Phi}_i, \mathbf{V} \rangle, \qquad i = 1,2,...,k, \tag{2.9a}$$

$$\mathbf{V}' = \sum_{i=1}^{k} \mathbf{\Phi}_i y_i, \tag{2.9b}$$

to produce the approximate flow field $\mathbf{V}'$. Properties of the POD guarantee that, for all k, the error $\|\mathbf{V} - \mathbf{V}'\|^2 = \langle \mathbf{V} - \mathbf{V}', \mathbf{V} - \mathbf{V}' \rangle$ is minimal for the set of m measured snapshots. For the subsequent derivations, we define the reduced state vector given by the k POD coefficients by $\mathbf{Y} = [y_1, y_2, ..., y_k]^T$ and denote the reduced POD basis by $\mathsf{U} = [\mathbf{\Phi}_1, \mathbf{\Phi}_2, ..., \mathbf{\Phi}_k]$.

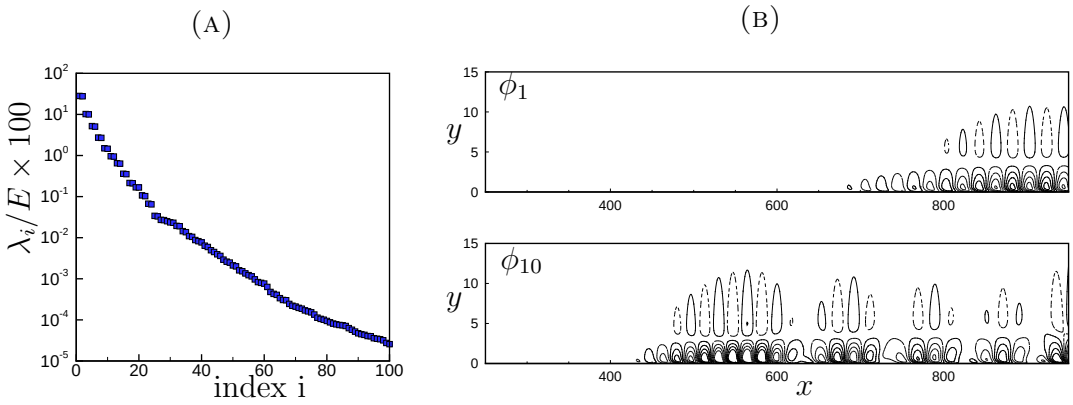

FIGURE 2.5: (a) First 100 POD eigenvalues λ_i of the correlation matrix. (b) Contours of the streamwise velocity component of the first ($\mathbf{\Phi}_1$) and tenth ($\mathbf{\Phi}_{10}$) POD-mode.

In what follows, snapshots have been obtained with the smaller Ω_{snap}-domain of dimension $(150, 950) \times (0, 40)$. A total of 1500 snapshots sampled each $\Delta t_{pod} = 5$ have been used to obtain the POD basis. From figure 2.6 a cut-off for the lower frequencies can be established at $f \approx 10^{-3}$ which, considering the total length T of the time data used to compute the POD basis ($T = 1500 \times 5 = 7500$), guarantees that the lowest physical frequencies $f \approx 10^{-3}$ have been explored approximately $7500 \times 10^{-3} \approx 8$ times. Figure 2.5(a) shows the corresponding eigenvalues of the correlation matrix, confirming a steady decay over about three decades in the first thirty modes (95 % of the energy is contained in the first ten modes). Two selected POD modes, $\mathbf{\Phi}_1$ and $\mathbf{\Phi}_{10}$, are displayed in figure 2.5(b).

The time-evolving POD coefficients $\mathbf{Y}(n)$ constitute the output of the system. In the next section, we will seek a model structure for a dynamic observer that is able to accurately predict $\mathbf{Y}(n)$ from the input to the system.

2.4.3 A dynamic observer obtained by identification technique

An approximation $\mathbf{Y}_e$ of the temporal evolution of the reduced state vector $\mathbf{Y}$ can be obtained by time marching a dynamic observer equation, whose structure is similar to the one given in (2.6), that is,

$$\mathbf{Y}_e(n+1) = \widetilde{\mathsf{A}}_s \mathbf{Y}_e(n) + \widetilde{\mathbf{L}} s(n). \tag{2.10}$$

The quantities $\widetilde{\mathsf{A}}_s$, $\widetilde{\mathbf{L}}$ and $\widetilde{\mathbf{C}}_s$ will be obtained with system identification techniques that solely rely on knowledge of input-output datasets $\{s(n), \mathbf{Y}(n)\}_{n=1..m}$, rather than by performing a Galerkin projection and solving a Riccati equation. A relation between the general formulation of subspace algorithms defined in § 2.4.1 and the dynamic observer notation can straightforwardly be defined as $\widetilde{\mathsf{A}}_s = \mathcal{C}\mathcal{A}\mathcal{C}^{-1}$ and $\widetilde{\mathbf{L}} = \mathcal{C}\mathcal{B}$, assuming that $\mathcal{D} = 0$.

The input $s(n)$ is related to the state $\mathbf{Y}_e(n)$ according to

$$s(n) = \widetilde{\mathbf{C}}_s \mathbf{Y}_e(n), \tag{2.11}$$

where $\widetilde{\mathbf{C}}_s$ is a measurement matrix which can be obtained using two different procedures: its exact definition or an identification techniques. In the first case, we combine equations (2.3) and (2.9) to get

$$\widetilde{\mathbf{C}}_{s,i}^{\text{exact}} = \int_{x_s}^{x_s+\Delta x} \left.\frac{\partial(\mathbf{\Phi}_i \cdot \tau_x)}{\partial y}\right|_{y=0} dx, \qquad \tau_x = \begin{pmatrix} 1 \\ 0 \end{pmatrix}. \tag{2.12}$$

The evaluation of this expression involves either measuring the POD modes or combining the measurements $\{s(n)\}_{n=1..m}$ associated with the velocity snapshots $\{\mathbf{V}_{\text{snap}}(n)\}_{n=1..m}$, that were used for the construction of the POD basis in §2.4.2. In the second case, we use a simple least-squares method applied to a composite time-series $\{s(n), \mathbf{Y}(n)\}_{n=1..m}$ of the learning dataset. It is straightforward to show that

$$\widetilde{\mathbf{C}}_s = [s(1) \cdots s(m)][\mathbf{Y}(1) \cdots \mathbf{Y}(m)]^{\dagger}, \tag{2.13}$$

where † denotes the Moore-Penrose pseudo-inverse.

As shown in §2.3.1, the true evolution matrix for $\mathbf{Y}$ is not $\widetilde{\mathsf{A}}_s$ but $\widetilde{\mathsf{A}}_w$. Considering a model-structure for $\mathbf{Y}$ similar to the one obtained by Gakerkin projection in (2.5), we see that the state $\mathbf{Y}(n)$ is governed by

$$\mathbf{Y}(n+1) = \widetilde{\mathsf{A}}_w \mathbf{Y}(n) + \widetilde{\mathbf{B}}_w w(n), \tag{2.14a}$$

$$s(n) = \widetilde{\mathbf{C}}_s \mathbf{Y}(n) + g(n), \tag{2.14b}$$

where the known input $\widetilde{\mathbf{L}}s(n)$ has been replaced by the unknown driving term $\widetilde{\mathbf{B}}_w w(n)$. The true evolution matrix $\widetilde{\mathsf{A}}_w$ in (2.14) can thus be obtained from the observer matrix $\widetilde{\mathsf{A}}_s$ via

$$\widetilde{\mathsf{A}}_w = \widetilde{\mathsf{A}}_s + \widetilde{\mathbf{L}}\widetilde{\mathbf{C}}_s. \tag{2.15}$$

	Galerkin projection	System identification
Reduced-order state	$\mathbf{X}(n)$	$\mathbf{Y}(n)$
ROM matrices	$\mathsf{A}_w, \mathbf{B}_w$	$\widetilde{\mathsf{A}}_w, \widetilde{\mathbf{B}}_w$
Estimated state	$\mathbf{X}_e(n)$	$\mathbf{Y}_e(n)$
Observer matrices	$\mathsf{A}_s, \mathbf{L}$	$\widetilde{\mathsf{A}}_s, \widetilde{\mathbf{L}}$
Measurement matrix	$\mathbf{C}_s$	$\widetilde{\mathbf{C}}_s^{\text{exact}}$ (obtained by definition)
		$\widetilde{\mathbf{C}}_s$ (obtained by least-squares)

TABLE 2.1: Notation used for the Galerkin-projection- and identification-based design of a dynamic observer.

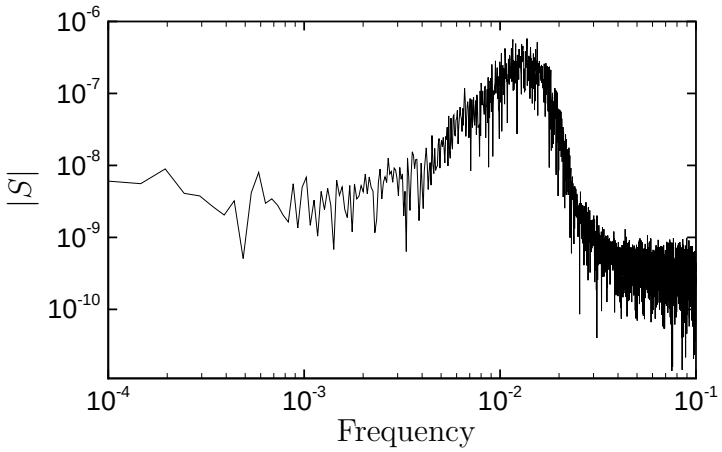

FIGURE 2.6: Spectrum of the input signal $s(t)$ obtained from the shear-stress sensor placed at $x = 200$.

The different notations used for the models obtained with Galerkin projection and identification techniques are summarized in table 2.1.

2.4.4 Identification of model coefficients with learning dataset

We obtain data by performing a linearized direct numerical simulation of the boundary layer in the presence of unknown noise. We use a sampling interval $\Delta t = 5$ for the velocity snapshots and the shear-stress measurements s. This choice of sampling interval can be justified by regarding figure 2.6, where the frequency spectrum of the input signal $S(f)$ is represented. This figure shows that the frequency content of s is rather low near the Nyquist frequency $f_{\text{nyquist}} = f_s/2 = 0.1$ defined by our sampling interval $\Delta t = 1/f_s$. The datasets to be processed are composed of the input signal from the sensor s and several outputs y_i corresponding to the projection of the snapshots onto the set of POD modes $\{\mathbf{\Phi}_i\}$ (figure 2.7).

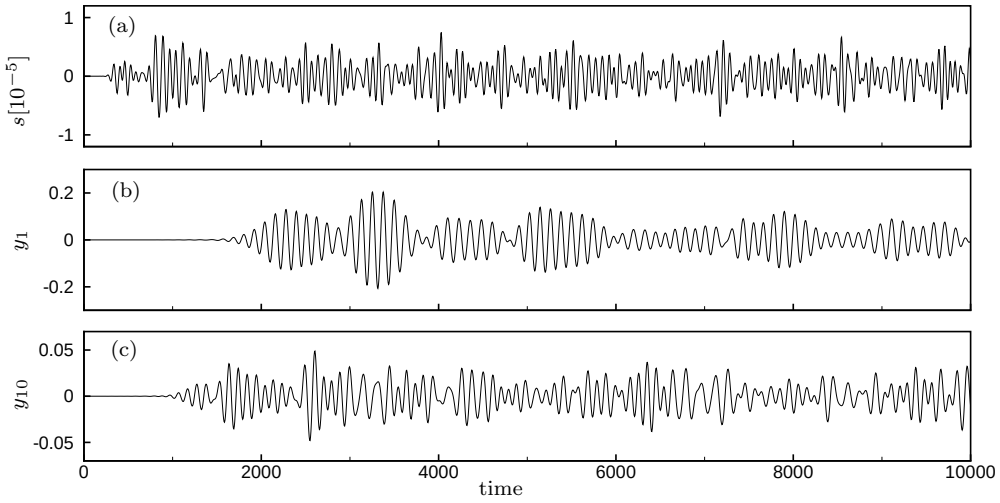

FIGURE 2.7: Learning dataset: (a) the measurement s capturing the influence of external noise and (b) and (c) the POD coefficients y_i obtained by projecting the flow field onto the POD modes $\mathbf{\Phi_1}$ and $\mathbf{\Phi}_{10}$, respectively.

Using the `N4SID` algorithm (Van Overschee and De Moor, 1994) and the Moore-Penrose pseuso-inverse, the model parameters $\widetilde{\mathsf{A}}_s$, $\widetilde{\mathbf{L}}$ and $\widetilde{\mathbf{C}}_s$ are then determined by fitting the model output to the true, measured output, as the model is forced by the recorded input. A reduced-order model has been determined with $k = 90$ POD modes and a learning data set of length $N_{\text{snap}} = 2000$.

2.4.5 Assessment of model performance with testing dataset

The validity of the identified parameters is subsequently confirmed by using a *different* data set (referred to as the testing data set) and by comparing the model output to the true output. As this testing data set has not been used in the identification of the model, we can assess the predictive capability of the identified model in this manner. The kinetic energy defined as $E(t) = \langle \mathbf{u}_{\text{snap}}, \mathbf{u}_{\text{snap}} \rangle \approx \mathbf{Y}^*\mathbf{Y}$ is an important variable of the system since it represents the global dynamics of the flow. The quality of fit between the energy of the DNS, denoted by $E(t)$, and the value predicted by the model, denoted by $\widetilde{E}(t)$, can be stated as

$$\mathsf{FIT}[\%] = 100 \left(1 - \frac{\left\| E(t) - \widetilde{E}(t) \right\|}{\| E(t) - \text{mean}(E(t)) \|} \right) \tag{2.16}$$

and can be used to quantify the performance of the estimator. Figure 2.8(a) displays the measured input signal s from the wall shear-stress sensor, from which

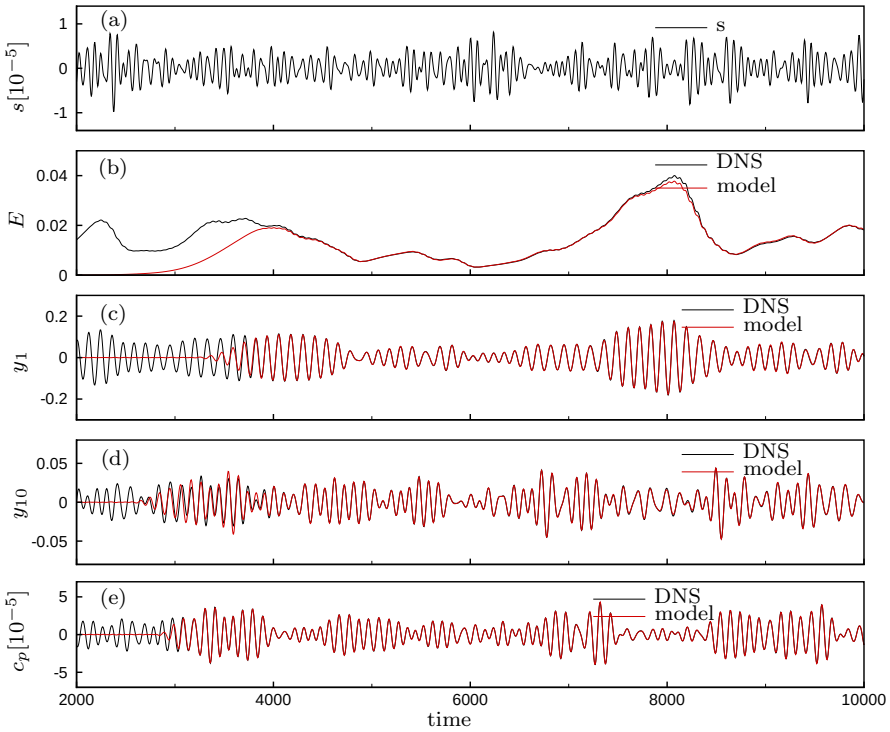

FIGURE 2.8: Validation dataset: performance of the system-identified model, initialized by $\mathbf{Y} = 0$ at $t = 2000$. The input data from the wall shear-stress sensor s is shown in (a); the remaining flow variables are recovered solely from this measurement signal using the identified model. (b-e) Comparison between the DNS (black) and the model prediction (red) for four variables from the testing dataset: (b) the energy of the system, (c) and (d) the POD coefficients y_i for the first and tenth modes, respectively, and (e) a friction sensor c_p placed at $x = 600$.

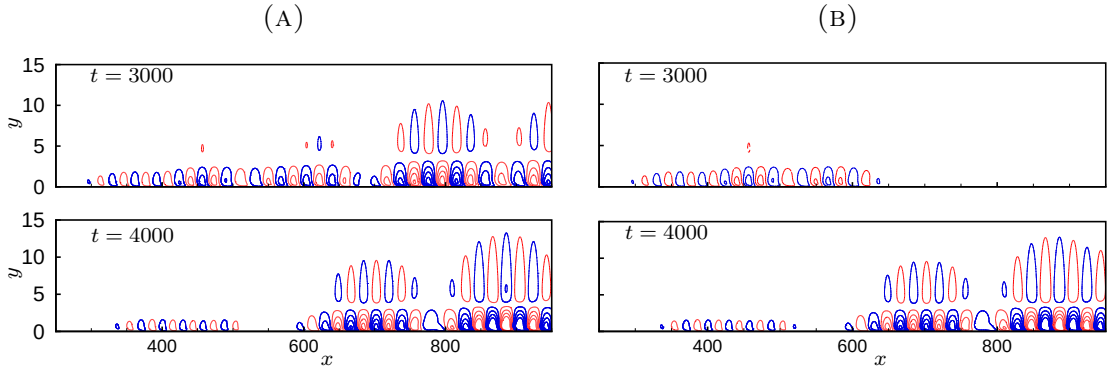

FIGURE 2.9: Snapshots of the streamwise disturbance velocity component obtained (a) from the DNS and (b) recovered from $s(n)$ via the model for $t = 3000$ and $t = 4000$. See supplementary movie 1.

all subsequent flow variables (figure 2.8(b-e)) can be derived using the identified model. In our case, we show the evolution of energy (b), the first and tenth POD coefficient (c,d) and the output from a friction sensor (e) placed at $x = 600$. After a short transient period, the predicted flow variables closely track their true DNS-equivalents, which yields a relative match of $\mathsf{FIT}_{\text{ener}} = 93.72\%$ when evaluated over the time interval $t \in [4000, 10000]$. The length of the transient period, estimated as $T_{\text{trans}} \approx 2000$, can be directly linked to the convective time of the disturbances. As previously mentioned, Tollmien-Schlichting waves are convected with a group velocity equal to $v_g = 0.375$. This convective velocity defines the characteristic time T_{conv} necessary for the wavepacket to cover the distance between the sensor s and the downstream edge of the domain Ω_{snap}. This time ($T_{\text{conv}} \approx 2000$) accurately predicts the duration of transient effects T_{trans}. This match between the time the estimator needs to propagate information and the time the system needs to convect a wavepacket confirms that the input-output behavior of the system is well-captured by the model. From the POD coefficients in $\mathbf{Y}_e$ the full flow field can be reconstructed from the basis U. Two examples of this reconstruction, visualized by the streamwise velocity component, are shown in figure 2.9 and compared to the equivalent full DNS simulation. The first instant at $t = 3000$ has been taken during the transient phase and shows a promising but incomplete match over the entire flow domain; a second instant at $t = 4000$ displays an excellent agreement between the flow structure recovered from $s(t)$ via the identified model and the full DNS solution.

2.4.6 Influence of some model parameters on performance

System-identification techniques usually contain numerous model parameters which have to be determined with care in order to obtain a representative and robust model of the underlying physical process. Subspace identification methods are particularly advantageous in this respect, when compared to parametrized models (see Hervé et al. (2012)), due to the relative simplicity of their parametrization; in fact, the size of the state-space model is the only user-defined parameter for subspace techniques.

In this section, we study the influence of the state-space size k (in other words, the number of POD modes), as well as the number of snapshots N_{snap} contained

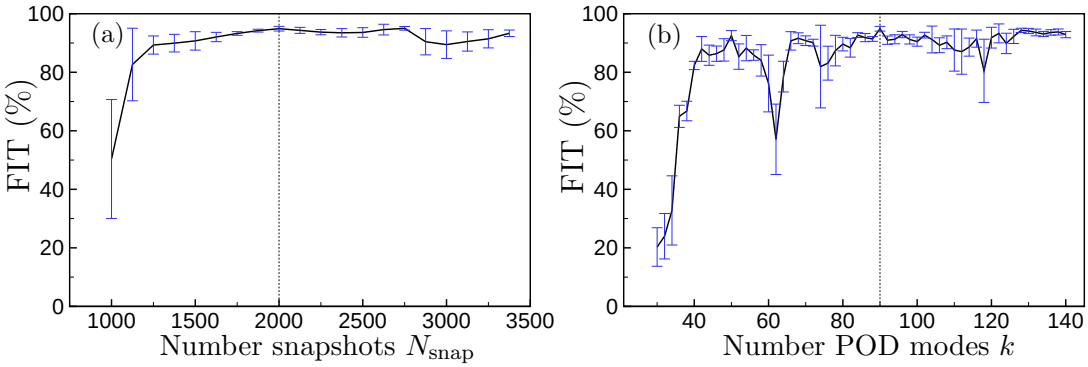

FIGURE 2.10: Influence of the model parameters on the quality of the identification. Mean (black) and standard deviation (blue) of the validation fit computed from samples of ten models obtained from different learning datasets. (a) Influence of the length of the learning dataset N_{snap} (for a fixed number of POD modes $N_{\text{pod}} = 90$) and (b) of the number of POD modes k (for a fixed number of snapshots $N_{\text{snap}} = 2000$).

in the learning dataset, on the quality of our identified reduced-order model. Figure 2.10 represents the statistical mean and standard deviation of the fit between the validation dataset and the predictions of different models. Both graphs have been obtained by computing, for each point on the curves, ten models obtained from distinct sections of a long learning dataset. The total length of the learning dataset is $N_{\text{snap}} = 8000$ (40000 time units) and the different learning sections i begin at different time instants, $t^{\text{init}}_{i=0..9} = 2500 + 500i$. Figure 2.10(a) shows, for a fixed number of POD modes ($k = 90$), the influence of the number of snapshots N_{snap}: we observe that a minimum number of snapshots are necessary to obtain an accurate model. This observation is common in identification techniques, since the algorithm requires sufficiently long time sequences from the dynamical system to arrive at statistically converged data. In our case, the identification procedure requires about $1500 \times 5 = 7500$ characteristic time units to obtain satisfactory results (signal components of the lowest system frequency $f = 10^{-3}$ have been explored about 8 times).

The influence of the number of POD modes k on the model quality (fit) observed in Figure 2.10(b) is far less trivial. For a fixed number of snapshots $N_{\text{snap}} = 2000$, a minimum number of $k = 40 - 50$ POD modes are required to obtain a good performance of the dynamic observer: this is related to the concept of observability of the POD basis.

Intuitively, a necessary condition for an observable system requires that the input

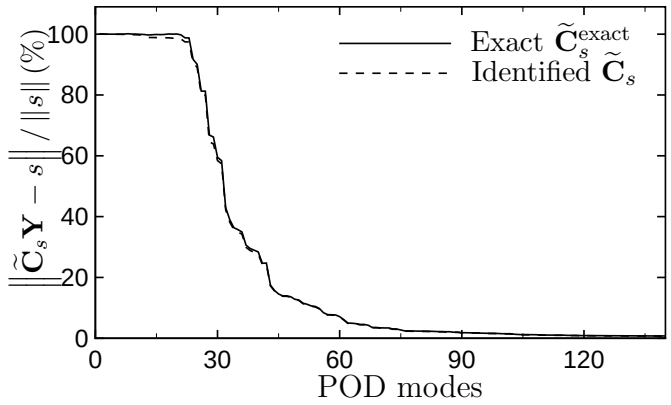

FIGURE 2.11: Relative error between the signal $s(t)$ obtained by DNS and the signal given by $\widetilde{\mathbf{C}}_s^{\text{exact}}\mathbf{Y}(t)$ (exact definition) and $\widetilde{\mathbf{C}}_s\mathbf{Y}(t)$ (estimated by least-squares) for different numbers of POD modes. $\|\cdot\|$ indicates the 2-norm on the vertical axis.

$s(n)$ and the state $\mathbf{Y}(n)$ are well correlated or, in other words, that the measurement $s(n)$ must be accurately representable by the POD coefficients according to $s(n) \approx \widetilde{\mathbf{C}}_s\mathbf{Y}(n)$. Figure 2.11 shows the relative error between the measurement $s(n)$ given by the sensor in the DNS simulation and the measurement $s = \widetilde{\mathbf{C}}_s\mathbf{Y}$, with $\mathbf{Y}$ obtained by projection of the velocity snapshots onto the POD modes. The solid and dashed lines respectively represent the relative error for the case where $\widetilde{\mathbf{C}}_s$ is obtained by measuring the POD modes (Eq. (2.12)) and by the pseudo-inverse (Eq. (2.13)). Both curves show a similar behaviour, reflecting the fact that, after a minimum number of POD modes are taken into account, the POD basis accurately captures the temporal behaviour of the measurement signal $s(n)$. The relatively high degree of the system ($N_{\text{pod}} = k = 90$) is related to the inherent lack of observability of the POD basis. Proper orthogonal decomposition maximizes the energy captured by a few orthogonal modes and, as is the case for the boundary layers (and, more generally, flow amplifiers), the most energetic structures are commonly localized downstream in the domain of interest. Consequently, the first POD modes do not show much spatial support in the upstream part of the domain, and higher modes are necessary to represent the full dynamics of $s(n)$. Figure 2.12 demonstrates this tendency, showing that the energy content of the modes at the location of the estimation sensor is nearly zero up to the 22^{nd} POD-mode.

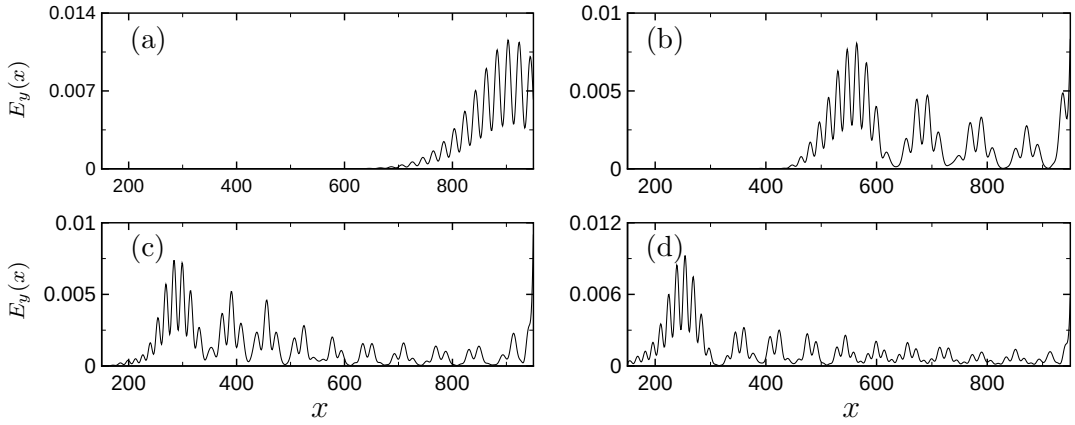

FIGURE 2.12: Local kinetic energy $E_y(x) = \int_0^\infty (u^2 + v^2)dy$ for four POD modes: (a) $\mathbf{\Phi}_1$, (b) $\mathbf{\Phi}_{10}$, (c) $\mathbf{\Phi}_{22}$ and (d) $\mathbf{\Phi}_{24}$. The estimation sensor is located at $x_s = 200$.

2.5 Comparison of model obtained by system identification with other techniques

In this section, we compare the performance of our identified dynamic observer to that of a more common Galerkin-based observer (§2.5.1) and to that of a Linear-Stochastic-Estimation (LSE)-based observer (§2.5.2).

2.5.1 Comparison with model obtained by Galerkin projection

The identification-based dynamic observer presented in this article is similar to the one obtained by Galerkin projection. However, the identification process will introduce a bias in the obtained model; this bias will be analyzed below. In figure 2.13, we compare the performances of the dynamic observer established in (2.6) by Galerkin projection and the one obtained in (2.10) by identification methods. Even though the temporal evolution of the POD coefficients is quite similar in both models, a slight overestimation in energy is observed in the identified system. The temporal evolution of the POD coefficients furthermore shows small oscillations in the signal of the identified model (noticeable for sufficiently small signal amplitudes; see $3000 < t < 4000$ in figures 2.13(a,b)). This oscillatory effect often appears in identified models and stems from an inadequate representation of some frequencies. It is important, however, to keep in mind that both models are associated with slightly different bases, but a fair comparison has to be performed

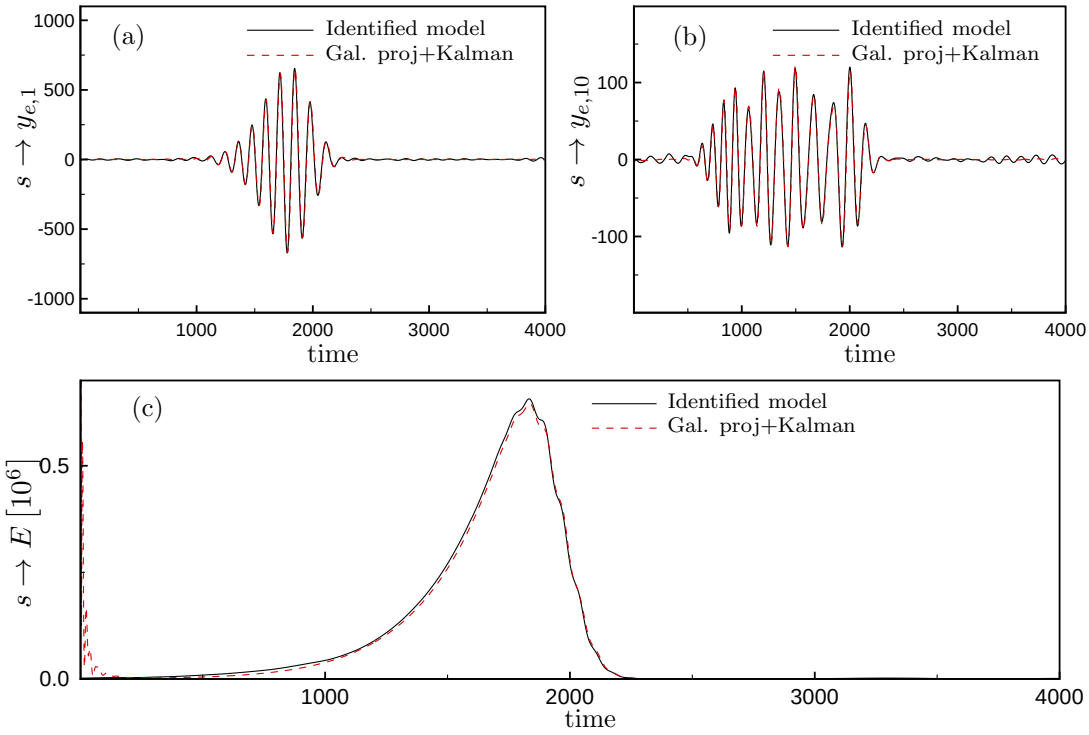

FIGURE 2.13: Galerkin-based ROM vs. estimated model impulse responses. (a) from s to $y_{e,1}$, (b) from s to $y_{e,10}$ and (c) from s to the perturbation energy $E = \mathbf{Y}_e^* \mathbf{Y}_e$.

on a common basis. To this end, we have chosen to project the estimated state $\mathbf{X}_e$ onto the POD basis U used to obtain the identified model.

2.5.2 Comparison with model obtained by LSE

Linear stochastic estimation (LSE) postulates a static linear relationship between a set of input signals (measurements from sensors) and a set of output variables of the flow. The LSE estimator can be formulated as

$$\mathbf{Y}_e(n) = \widetilde{\mathsf{R}}\mathbf{S}(n), \tag{2.17}$$

where $\mathbf{Y}_e(n) \in \mathbb{R}^k$ and $\mathbf{S}(n) \in \mathbb{R}^m$ are vectors containing, respectively, the k estimated output variables by LSE at time n and the measurements from m sensors at time n, and $\widetilde{\mathsf{R}}$ is a matrix obtained by minimizing the mean-squared error between the true output and the one predicted by the model, in other words, $\|\mathbf{Y} - \mathbf{Y}_e\|^2$.

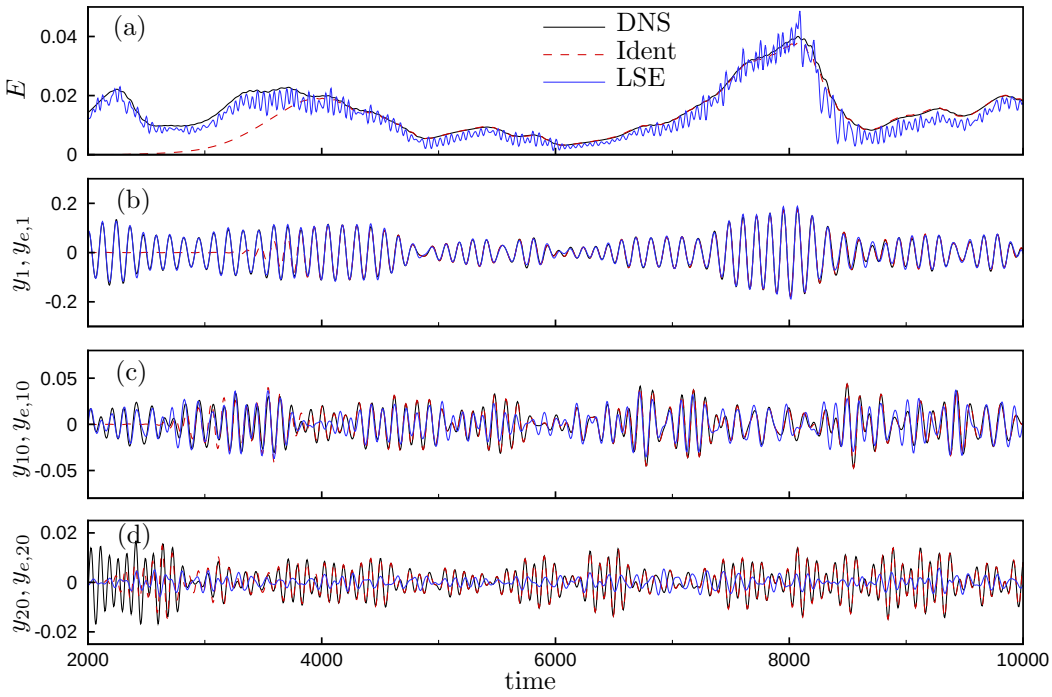

FIGURE 2.14: Performance of LSE compared to the dynamic observer. The input data used by the LSE model comes from ten equispaced shear-stress sensors between $x = 500$ to $x = 950$, while the dynamic observer uses a single sensor located at $x_s = 200$. (a-d) Comparison between the linearised DNS (black), the identified dynamic observer prediction (red dashed) and the LSE model (blue) for three variables from the testing dataset: (a) the energy of the system and (b-d) the POD coefficients y_i for the first, tenth and twentieth mode, respectively.

In our numerical experiments, a linear estimator has been computed based on input from ten shear-stress sensors (equispaced between $x = 500$ to $x = 950$) and 20 POD modes representing the flow state. Figure 2.14 shows a comparison of DNS results with results obtained from applying either LSE or a dynamic observer. It appears that, in the case of LSE, a great many more sensors are required to obtain a model of similar quality (performance) than the one provided by the dynamic observer. This observation corroborates the need of the estimator to correctly identify the wavelengths of the Tollmien-Schlichting waves – a requirement that can be met with very closely spaced sensors. By comparing different POD coefficients, this point can be further substantiated. For instance, in figure 2.14, the first POD coefficient y_1 (corresponding to a structure with large wavelengths) is well represented by the model, while the tenth and twentieth POD coefficients (y_{10} and y_{20}), associated with far shorter wavelengths, deviate more noticeably from the DNS results. Moreover, the energy predicted by the LSE-model appears rather

noisy compared to the DNS. This feature arises, again, from the poor representation of the shorter wavelengths of the flow, but it also stems from the inherent lack of accuracy of first-order truncated stochastic models. This second source of inaccuracies can be alleviated by considering higher-order terms, while adding closer-spaced sensors will achieve a better representation of the poorly estimated wavelengths. It is also important to notice that the linear stochastic estimator does not contain a transient phase, as the dynamic observer does. Furthermore, it needs fewer POD modes: the dynamic observer requires a large number of POD modes to fulfill the observability condition discussed in §2.4.6, whereas the linear stochastic estimator is not subjected to this constraint. It has been verified that including more than 20 POD modes does not further improve the performance of the LSE model.

Figure 2.15 represents snapshots of the streamwise disturbance velocity at a given instant ($t = 8000$) for six different cases. The first two snapshots represent results from the DNS and from a reconstruction by the identified dynamic observer based on a single sensor located at $x_s = 200$, respectively. The last four snapshots are obtained via LSE using different numbers of sensors placed at different positions. In the first of the LSE-cases (figure 2.15(c)), seventeen equispaced sensors, located between $x = 150$ and $x = 950$, are considered. A satisfactory prediction of the velocity field is obtained with this configuration, even though the structures far upstream are not as well represented when compared to the dynamic observer. In figures 2.15(d,e) ten sensors have been placed equidistantly, in one case, between $x = 500$ and $x = 950$ and, in a second case, between $x = 150$ and $x = 600$. When the ten sensors are concentrated in the downstream part of the domain, upstream information is lost and vice versa for an upstream placement of the sensors. Finally, figure 2.15(f) uses only two sensors (at $x = 200$ and $x = 950$): this time, LSE fails to recover any relevant information about the flow structures. These results underline the fact that linear stochastic estimation requires spatial support of the input information (sensors) over the whole domain due to the strong convection, while the dynamic observer only needs information from a localized input signal. In summary, the above numerical experiments show that a dynamic observer model is preferable over a linear stochastic estimator (LSE) model in providing an accurate approximation of the flow field from localized and sparse measurements.

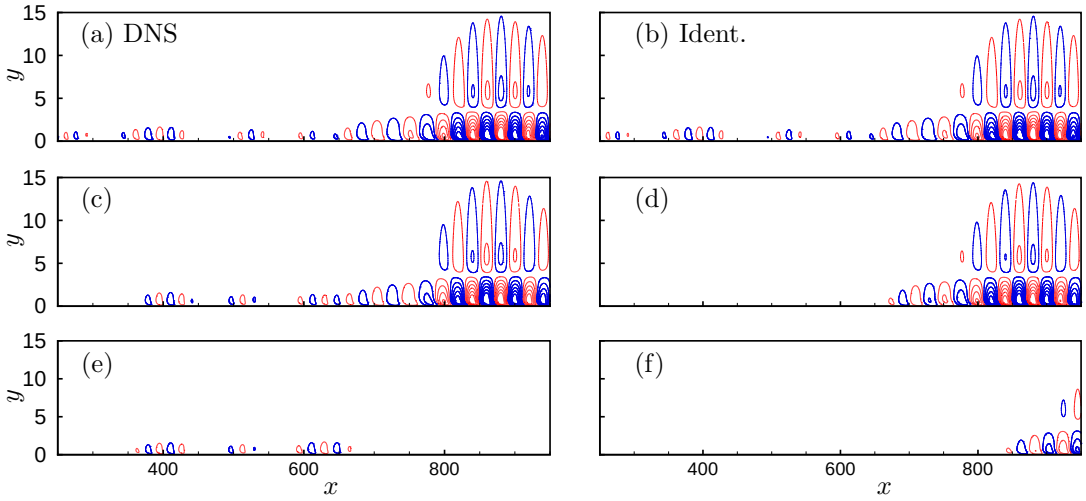

FIGURE 2.15: Snapshots of the streamwise disturbance velocity at $t = 8000$ obtained (a) from linearized direct numerical simulations (DNS), (b) recovered from a single sensor via the identified dynamic observer, (c-f) recovered from shear-stress sensors via a LSE model: (c) from seventeen sensors equispaced between $x = 150$ to $x = 950$, (d) from ten sensors equispaced between $x = 500$ to $x = 950$, (e) from ten sensors sensors equispaced between $x = 150$ to $x = 600$ and (f) from two sensors placed at $x = 150$ and $x = 950$.

2.6 Application of optimal control

The successful recovery of full-state information from single wall shear-stress measurements by a dynamic observer enables the design of a variety of effective control schemes, which we demonstrate next. For this purpose, a control signal u is placed at $(x_u, y_u) = (250, 1)$ (downstream of the sensor s), which constitutes a feedforward control configuration. The governing equations (2.6) of the dynamic observer are modified to reflect this addition. We have

$$\mathbf{Y}_e(n+1) = \widetilde{\mathsf{A}}_s \mathbf{Y}_e(n) + \widetilde{\mathbf{L}} s(n) + \widetilde{\mathbf{B}}_u u(n). \tag{2.18}$$

Following Hervé et al. (2012), the system is excited with a frequency-rich signal u in order to identify the new term $\widetilde{\mathbf{B}}_u$. The unknown system matrices $\widetilde{\mathsf{A}}_s$, $\widetilde{\mathbf{L}}$ and $\widetilde{\mathbf{B}}_u$ may then be determined in a similar way as described in § 2.4. From there, the true linear system matrix $\widetilde{\mathsf{A}}_w$ which governs the perturbation dynamics ((2.14) with added control term) can be extracted following (2.15). This matrix is then used for the design of an LQR-optimal controller $u(n) = \mathbf{K}\mathbf{Y}(n)$, which minimizes the cost functional $\sum_{n=0}^{\infty} \mathbf{Y}(n)^* \mathsf{Q} \mathbf{Y}(n) + \ell^2 |u(n)|^2$, where Q is a positive definite weight matrix and ℓ is a user-specified parameter to balance disturbance energy and exerted control energy. Following standard procedure (see Burl (1999)), the

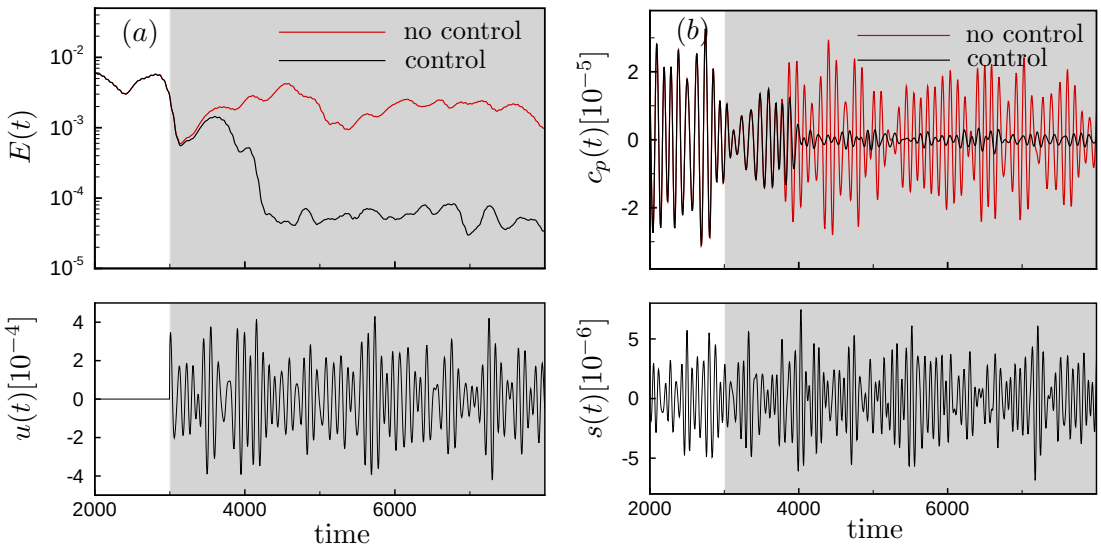

FIGURE 2.16: Results of the LQR-control design based on the dynamic observer. (a) Temporal evolution of the perturbation energy $E(t)$ for the uncontrolled simulation (red) and the controlled simulation targeting the energy (black), together with the control signal $u(t)$ obtained in the case of the energy objective (see supplementary movie 2). (b) Time signal of the friction sensor $c_p(t)$ placed at $(x_{c_p}, y_{c_p}) = (600, 0)$ for the uncontrolled (red) and controlled simulation targeting the sensor signal c_p (black), together with the sensor signal s, which is the same in all simulations discussed in this figure.

control gain $\mathbf{K}$ can be obtained by solving a Riccati equation involving $\widetilde{\mathsf{A}}_w$, $\widetilde{\mathbf{B}}_u$, Q and ℓ.

Two different control objectives Q have been considered: (i) the suppression of the energy $E(t)$ inside the velocity window ($\mathsf{Q} = \mathsf{I}$) and (ii) the control of the signal variance recorded by the downstream friction-sensor c_p ($\mathsf{Q} = \widetilde{\mathbf{C}}_p^* \widetilde{\mathbf{C}}_p$, with $\widetilde{\mathbf{C}}_p$ as the measurement vector associated with c_p and obtained with the least-squares technique introduced in § 2.4.3 to obtain $\widetilde{\mathbf{C}}_s$). We use a model that comprises 50 modes computed on a shorter domain ($\Omega_{\text{snap}} = (200, 700) \times (0, 40)$). In the controlled simulation, the measurement s is used to reconstruct the full perturbation field $\mathbf{Y}_e$ based on the identified model, and the control law is obtained by applying the control gain $\mathbf{K}$ to this state. Results are shown in figure 2.16 together with the control signal $u(t)$ and the friction-sensor signal s. In both cases, a substantial reduction in the respective objectives can be accomplished. The energy $E(t)$ has been reduced by nearly two orders of magnitude (a reduction of 96.81% in the mean perturbation energy), while the rms-value of the friction sensor signal has been lowered by about 88.01%.

2.7 Summary and conclusions

A dynamic observer recovering full-state information from single wall shear-stress measurements has been designed that relies on a POD basis (from measured snapshots) and system identification techniques. For noise-amplifier flows, it successfully reproduces the perturbation dynamics (velocity fields) throughout the full sampling domain and furnishes information about the flow that can subsequently be used by itself, for flow diagnostics or, in a second step, for LQR-control design.

Within the limits of linear perturbation dynamics, the design process for the dynamic observer extracts the system matrix from a sequence of snapshots; this system matrix describes a globally stable flow configuration that is sustained by selectively amplified random perturbations from the noise environment. The proposed method thus successfully separates the intrinsic, stable perturbation dynamics from the external noise excitation, which previously could only be quantified in its entirety.

A wide variety of flow analyses is possible once the system matrix has been extracted. In the present case, we chose to design a closed-loop control scheme which, owing to the known system matrix, could now be accomplished using full-state information control (LQR) algorithms. As a consequence, a significant reduction of the perturbation energy or sensor signal rms-values could be achieved. Even though system identification could have been used to determine a direct input-to-output control law targeting the variance of a downstream wall-sensor (Hervé et al., 2012), the retrieval of full-state information gives a far more physical and structural view of dynamic processes.

The input data for the design procedure of the dynamic observer are readily available in experiments, and an application of a dynamic observer in a suitable experiment is currently planned and will be explored in a future effort. However, difficulties not accounted for in the present paper are expected to arise in an experimental situation: noise corrupting the PIV and friction measurements, the presence of non-localized external forcing or the presence of non-linearities are some examples. These challenges will be addressed in a forthcoming study.

Acknoledgements

The authors would like to thank J.C. Robinet and A. Hervé for fruitful conversations, as well as J.C. Loiseau for his support with `Nek-5000`.

Chapter 3

Recovery of the inherent dynamics of noise-driven amplifier flows

This chapter is presented in the form of a self-contained article submitted to the *Journal of Fluid Mechanics*. The authors of this paper are J. Guzmán Iñigo, D. Sipp and P. J. Schmid. In this article, we use the dynamic observer introduced in Chapter 2 to separate the intrinsic dynamics from the external noise in a noise-driven amplifier flow. The global modes of the reduced-order model are then computed and qualitatively compared to global modes of the full-order system reported in the literature. The frequency response of the ROM has also been computed.

Abstract

A reduced-order model which accurately predicts the dynamics of a two-dimensional boundary layer along a flat plate is determined from time-dependent input-output data. A system-identification approach is used to extract such a model from time-synchronous velocity field snapshots and wall-shear stress measurements. The spectrum and frequency response of the model is subsequently computed and qualitatively compared to results reported for the full-order system. This comparison confirms that the main characteristics of the boundary-layer are well captured by

the reduced-order model. This data-driven technique represents a system-theoretic attempt of separating the globally stable, linear flow dynamics from the driving by an external noise environment that ultimately maintains the flow in a statistically stationary state.

3.1 Introduction

Unsteadiness in open flows can be classified into two main categories: (i) oscillator-type flows, which are defined by a global instability resulting in self-sustained oscillatory fluid behaviour (intrinsic dynamics); and (ii) noise amplifiers, which are characterised by selectively amplifying environmental noise that is present in the upstream flow (extrinsic dynamics). Dynamic mode decomposition (Rowley et al., 2009; Schmid, 2010) provides a powerful post-processing tool for analysing oscillator-type flows from a sequence of measurement snapshots. DMD assumes that a linear mapping $\mathscr{A}$ links the n-th flow field $\mathbf{u}(n)$ to the subsequent flow field $\mathbf{u}(n+1)$, that is $\mathbf{u}(n+1) = \mathscr{A}\mathbf{u}(n)$. This technique has been proven to successfully recover the oscillatory modes and frequencies in flows with self-sustained oscillations (Schmid et al., 2011; Schmid, 2011; Seena and Sung, 2011; Bagheri, 2013).

The recovery of the intrinsic dynamics of amplifier flows, on the other hand, is a more challenging problem. Amplifier flows are globally stable, but selectively amplify upstream disturbances by convective instabilities. Consequently, the system dynamics are entirely driven by the environmental noise. The assumption of a linear mapping $\mathscr{A}$, made by DMD, is thus only partially satisfied, and the driving term remains undetermined. For this reason, an alternative data-based technique, which takes into account the noise-driven characteristics of the flow, is needed for the case of amplifier flows. In this article, we propose to separate the noise from the inherent dynamics using a localised sensor together with system identification. Over the past few years, system identification has proven to be a promising approach for the extraction of amplifier-flow models from input-output data. Several applications to closed-loop control have been successfully carried out in numerical simulations (Hervé et al., 2012; Juillet et al., 2013) and experimental setups (Juillet et al., 2014; Gautier and Aider, 2014). While in previous studies the models focus on the dynamics between one upstream and one downstream sensor, Guzmán Iñigo et al. (2014) extended the technique to capture the

dynamics between upstream measurements and the entire perturbation field. In this work, we employ this latter technique to extract the inherent dynamics of a boundary layer. More specifically, the eigenvalues, associated eigenvectors and the frequency response of the identified model will be extracted from data sequences of the noise-driven flow and, the flow characteristics will be compared to results reported previously in the literature (Ehrenstein and Gallaire, 2005).

The article is organised as follows. § 3.2 briefly describes the flow configuration and the governing equations. § 3.3 presents the equations of the dynamic observer and analyses the intrinsic dynamics of the system that can be extracted from such a model. The particular methodology to extract the unknown state-space matrices of the system from the data is described in § 3.4. A summary of results and conclusions are given in § 3.5.

3.2 Flow configuration and governing equations

The flow configuration chosen to illustrate the proposed techniques and concepts consists of a transitional two-dimensional boundary layer over a flat plate. This flow constitutes a classical and generic example of a noise amplifier, i.e., a globally stable system which selectively amplifies upstream disturbances by convective instabilities. In a low-amplitude noise environment, two-dimensional Tollmien-Schlichting waves appear as a result of this convective instability mechanism.

We consider the spatio-temporal evolution of small-amplitude disturbances $\mathbf{u}$ about a given base-flow $\mathbf{U}_0$, which we take as a zero-pressure gradient boundary layer. The disturbances $\mathbf{u}$ are driven by an external forcing term, $\mathbf{F}_w w(t)$, which represents and models an upstream disturbance source of unknown origin. For simplicity, we assume that $w(t)$ is a random process of zero mean and variance W, while $\mathbf{F}_w$ describes a spatial two-dimensional Gaussian distribution centred at $(x_w, y_w) = (50, 0.95)$, of width $(\sigma_x, \sigma_y) = (1, 0.1)$ and amplitude $A = 0.1$. The spatio-temporal evolution of the entire flow field, $\mathbf{U}_{\text{tot}} = \mathbf{U}_0 + \mathbf{u}$, is governed by the incompressible Navier-Stokes equations, augmented by the forcing term. With the base flow $\mathbf{U}_0$ as a solution of the unforced steady Navier-Stokes equations, the evolution of the perturbations is given by the following equations

$$\partial_t \mathbf{u} + \mathbf{U}_0 \cdot \nabla \mathbf{u} + \mathbf{u} \cdot \nabla \mathbf{U}_0 = -\nabla p + Re_{\delta_0^*}^{-1} \Delta \mathbf{u} + \mathbf{F}_w w(t), \qquad \nabla \cdot \mathbf{u} = 0, \quad (3.1)$$

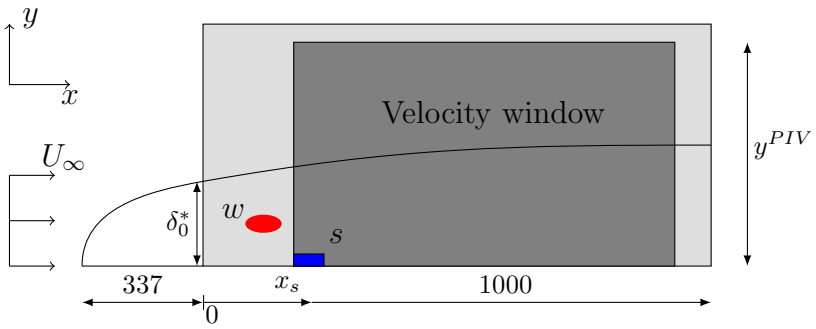

FIGURE 3.1: Sketch of the flow configuration. The computational domain Ω is of size $(0, 1000) \times (0, 40)$, represented by the light gray box. The upstream receptivity of the boundary layer to external perturbations is modelled by the noise w which is placed at $(x_w, y_w) = (50, 0.95)$. A sensor located at $(x_s, y_s) = (200, 0)$ will identify incoming perturbations, while a velocity window of extent $(200, 900) \times (0, 40)$ (represented by the dark gray box) is used to quantify the effect of the forcing on the velocity field.

where the nonlinear term $\mathbf{u} \cdot \nabla \mathbf{u}$ has been omitted since only low-amplitude noise $W \ll 1$ will be considered. This assumption ensures linear perturbation dynamics, as well as a linear response to the noise w. During the direct numerical simulations (DNS), white noise is imposed via $w(t)$ to mimic upstream excitations of unknown source and distribution (mimicking conditions in physical experiments). For the temporal evolution, we use a time step of $dt_{\text{dns}} = 0.1$ ($CFL = 0.379$). The flow variables are non-dimensionalised using the displacement thickness δ_0^* of the boundary layer at the computational inlet ($x_0 = 0$) and the free-stream velocity U_∞. Consequently, the Reynolds number is defined as $Re_{\delta_0^*} = U_\infty \delta_0^* / \nu$. All simulations were performed at $Re_{\delta_0^*} = 1000$, which guarantees strong amplification produced by the Tollmien-Schlichting instability.

The governing equations (3.1) are solved in a computational domain Ω of size $(0, 1000) \times (0, 40)$, sketched in figure 3.1. A Blasius profile of unit displacement thickness is prescribed at the left boundary, outflow conditions are employed at the upper and right boundaries, and a no-slip condition is imposed at the wall. We use the spectral-element code `Nek5000` (see https://nek5000.mcs.anl.gov) to perform the computations below.

Two different measurements are extracted from the simulations in order to compute the reduced-order model. Special emphasis is directed towards the use of data that may be readily available in an experiment, since the application of our technique to an experimental setup is the final objective of the procedure described in this article. We first consider a wall-friction sensor s (see figure 3.1), located at

$x_s = 200$ and of spatial streamwise extent $\Delta x = 5$, which records the wall shear-stress s_{tot}. The fluctuating component s may be obtained by subtracting the time-averaged value of s_{tot} from the signal s_{tot}. For the case of low-amplitude forcing, i.e., for linear perturbation dynamics, the time-averaged value also corresponds to the base-flow value. In addition to the wall-friction sensor s, we also consider velocity snapshots $\mathbf{u}_{\text{snap}}$, taken in a given domain Ω_{snap} of size $(200, 900) \times (0, 40)$, (see figure 3.1). The fluctuating components of the velocity field may again be obtained by subtracting the time-averaged snapshots from the total snapshot sequence. In what follows, we will consider time series of composite data comprising skin-friction measurements and velocity snapshots. The reduced-order model will be extracted from these data.

3.3 A dynamic observer to recover the dynamics of noise-amplifier flows

3.3.1 A reduced-order dynamic observer

Considering Eq. (3.1), the evolution of small-amplitude perturbations $\mathbf{u}$ about a given base flow for the case of a noise amplifier can be represented in the time-discrete domain by $\mathbf{u}(n+1) = \mathscr{A}\mathbf{u}(n) + \mathbf{F}w(n)$, where $\mathscr{A}$ denotes the linear system operator, $\mathbf{F}w(n)$ represents the driving by external perturbations and n stands for the n^{th} time-step. Noise-amplifier flows are characterised by selectively amplifying external perturbations – despite being globally stable systems. This feature arises from the non-normality of the operator $\mathscr{A}$ (Chomaz, 2005). As a consequence, the system dynamics are entirely driven by the term $\mathbf{F}w(n)$, which generally represents a random external noise of unknown distribution that would be difficult, or even impossible, to measure in experimental situations. An indirect quantification method is thus necessary to separate the intrinsic dynamics from the noise. In the present work, we propose to capture the influence of the forcing term $\mathbf{F}w(n)$ by means of a localised sensor, specifically wall-shear stress measurements $s(n)$. This approach implies the loss of the receptivity information by correlating the effect of the noise at a single point with the effect on the entire domain.

A dynamic observer which describes the dynamics of $\mathbf{u}_e(n)$ based on the input $s(n)$, instead of $\mathbf{F}w(n)$, is introduced according to

$$\mathbf{u}_e(n+1) = \mathscr{A}_s \mathbf{u}_e(n) + \mathscr{L} s(n). \tag{3.2}$$

The matrices $\mathscr{A}_s$ and $\mathscr{L}$ are chosen to render the temporal evolution of $\mathbf{u}_e$ as close as possible to the temporal evolution of $\mathbf{u}$. We use the approach introduced by Guzmán Iñigo et al. (2014) which consists of the extraction of the above matrices from time-evolving data using system-identification techniques. However, the large number of degrees of freedom contained in the snapshots $\mathbf{u}$ makes direct application of identification techniques excessively expensive. It is thus mandatory to reduce the dimensionality of the measured data. To this end, we use proper orthogonal decomposition (POD) modes Lumley (1967); Sirovich (1987) to form a reduced basis. We process a sequence of m velocity snapshots extracted from the simulation in the presence of the upstream noise w. The proper orthogonal decomposition then enables us to compute a ranked orthonormal basis $\{\mathbf{\Phi}_i\}_{i=1..m}$ of flow fields, satisfying $\langle \mathbf{\Phi}_i, \mathbf{\Phi}_j \rangle = \delta_{ij}, \quad i,j = 1,2,...,m$, which can be expressed most conveniently as a linear combination of these m snapshots. Here, the scalar-product $\langle \cdot \rangle$ denotes the energy-based inner product: $\langle \mathbf{u}^1, \mathbf{u}^2 \rangle = \int_\Omega (u^1 u^2 + v^1 v^2)\, dx\, dy$. Any velocity field $\mathbf{V}$ from the domain Ω can then be projected onto the first k POD-modes according to

$$y_i = \langle \mathbf{\Phi}_i, \mathbf{V} \rangle, \qquad i = 1,2,...,k, \tag{3.3}$$

to produce the approximate flow field $\mathbf{V}' = \sum_{i=1}^{k} \mathbf{\Phi}_i y_i$. Properties of the POD guarantee that, for all k, the error $\|\mathbf{V} - \mathbf{V}'\|^2 = \langle \mathbf{V} - \mathbf{V}', \mathbf{V} - \mathbf{V}' \rangle$ is minimal for the set of m measured snapshots. For the following derivations, we define the reduced output vector given by the k POD-coefficients by $\mathbf{Y} = [y_1, y_2, \ldots, y_k]^T$ and denote the reduced POD basis by $\mathsf{U} = [\mathbf{\Phi}_1, \mathbf{\Phi}_2, \ldots, \mathbf{\Phi}_k]$. The velocity snapshots $\mathbf{u}$ are projected onto these modes to obtain the time-evolving POD coefficients $\mathbf{Y}(n)$ which constitute the new output of the system. The equation governing the dynamic observer (3.2) can be projected as well onto the POD basis, leading to the equation

$$\mathbf{Y}_e(n+1) = \widetilde{\mathsf{A}}_s \mathbf{Y}_e(n) + \widetilde{\mathbf{L}} s(n), \tag{3.4}$$

where $\widetilde{\mathsf{A}}_{s;i,j} = \langle \mathbf{\Phi}_i, \mathscr{A}_s \mathbf{\Phi}_j \rangle$ and $\widetilde{\mathbf{L}}_i = \langle \mathbf{\Phi}_i, \mathscr{L} \rangle$. In what follows, we will seek to recover and analyse the dynamics of the system by computing these reduced-order

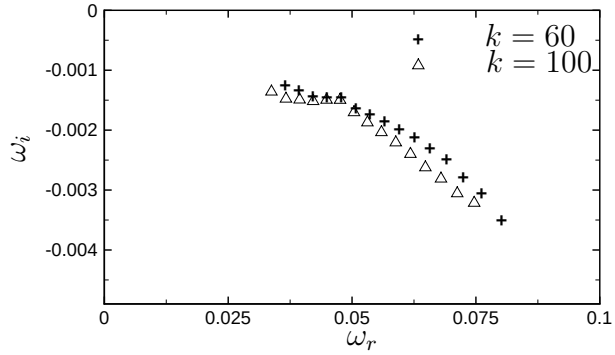

FIGURE 3.2: Eigenvalue spectrum in the (ω_r, ω_i)-plane for two different, identified reduced-order models using 60 and 100 POD-modes.

matrices from the projected data.

Our choice of the discrete-time formulation emerges naturally when data-based methods are considered to analyse experimental situations. However, some of the concepts of dynamical-systems theory that are introduced in the subsequent sections, such as modal analysis or the frequency response, have a more direct physical interpretation and definition when a continuous-time framework is employed. The continuous formulation of the dynamic observer (equation (3.4)) reads

$$\mathrm{d}\mathbf{Y}_e/\mathrm{d}t = \widetilde{\mathsf{A}}'_s \mathbf{Y}_e(t) + \widetilde{\mathbf{L}}' s(t). \tag{3.5}$$

The time coordinate t is related to the time-index n by $t = n\Delta t$, with Δt representing the sampling time. A relation between the matrices of equation (3.4) and equation (3.5) can be derived, resulting in $\widetilde{\mathbf{L}} = \int_0^{\Delta t} \exp[\widetilde{\mathsf{A}}'_s(\Delta t - \tau)]\widetilde{\mathbf{L}}'\, d\tau$ associated with the discrete driving term and $\widetilde{\mathsf{A}}_s = \exp(\widetilde{\mathsf{A}}'_s \Delta t)$ denoting the evolution matrix over a time interval Δt; see Antoulas (2005) for a more comprehensive description of the discrete-to-continuous time transformation.

3.3.2 Global modes

The unknown matrices of equation (3.4) have been determined using a system-identification technique presented in more detail in §3.4. Equation (3.4) then allows the computation of the temporal global spectrum of the system via the common assumption of an exponential time-dependence $\mathbf{Y}_e(t) = \widehat{\mathbf{Y}}_e \mathrm{e}^{-i\omega t}$. We

consequently obtain a generalised eigenvalue problem for $(\omega, \widehat{\mathbf{Y}}_e) \in \mathbb{C}$ of the form

$$\widetilde{\mathsf{A}}'_s \widehat{\mathbf{Y}}_e = -i\omega \widehat{\mathbf{Y}}_e. \tag{3.6}$$

The eigenvalues $\omega = \omega_r + i\omega_i$ are displayed in figure 3.2. The horizontal and vertical axes correspond, respectively, to the frequency ω_r and the growth rate ω_i. The figure is symmetric with respect to $\omega_r = 0$, and eigenvalues in the half plane $\omega_i < 0$ represent stable eigenmodes.

Two different models have been used with $k = 60$ and $k = 100$ POD-modes, respectively. We observe that, for both models, all extracted eigenvalues are stable and show similar growth rates. The robustness of the spectrum with respect to the number of used POD-modes reveals that the extracted modal dynamics appears to be intrinsically related to the flow. The associated eigenvectors can be recovered using the relation $\widehat{\mathbf{V}} = \mathbf{U}\widehat{\mathbf{Y}}_e$. Based on the spectrum of the model composed of 60 POD-modes, the modal structure for eigenvalues with $\omega_r \approx 0.036$, $\omega_r \approx 0.05$, $\omega_r \approx 0.059$ and $\omega_r \approx 0.08$ are displayed in figure 3.3. Contours of the real part of the streamwise velocity component $\widehat{\mathbf{V}}$ are depicted, and the perturbations are seen to be located near the wall, with the typical wavelength of the structures decreasing with increasing frequency. The amplitudes of the modes grow in the downstream direction for the three lowest frequencies, while the highest frequency presents a maximum that can be linked to the branch-II location for that particular frequency. A qualitative comparison between these results and the spectrum obtained by Ehrenstein and Gallaire (2005) or Alizard and Robinet (2007) from the full linearised operator $\mathscr{A}$ reveals that the most significant characteristics are well-captured by the identified reduced-order model. A quantitative comparison, however, is a non-trivial task due to the difficulty of defining representative boundary conditions. Indeed, Ehrenstein and Gallaire (2005) demonstrates that some of the eigenvalues are highly sensitive to the boundary conditions as well as to the length of the domain. Brandt et al. (2011) showed that this phenomenon is observed when branch I and branch II-locations (these define the upstream and downstream boundaries of the wave-maker region) of the considered global mode are not both included in the computational domain (which is the case for all the global modes presented here). This feature is commonly observed for noise-amplifier flows and stems from the non-normality of the operator $\mathscr{A}$(Sipp et al., 2010).

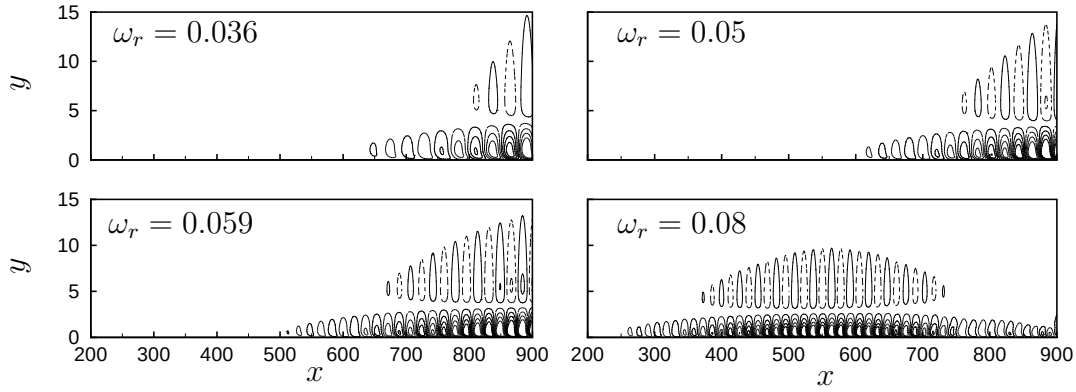

FIGURE 3.3: Contours of the real part of the eigenmodes associated with four of the eigenvalues depicted in figure 3.2 corresponding to the model based on $k = 60$ POD-modes.

3.3.3 Frequency response

A more robust alternative for studying the dynamics of noise amplifiers involves the frequency response. Assuming that the system 3.4 is forced by a harmonic input $s(t) = \mathrm{e}^{i\omega t}$, a response is sought in the form $\mathbf{Y}_e(t) = \overline{\mathbf{Y}}_e \mathrm{e}^{i\omega t}$, which leads to the expression

$$\mathbf{R}(\omega) = \mathbf{Y}_e(\omega)/s(\omega) = \left(i\omega \mathsf{I} - \widetilde{\mathsf{A}}'_s\right)^{-1} \widetilde{\mathbf{L}}', \tag{3.7}$$

where $\mathbf{R}(\omega)$ is defined as the frequency response and links the harmonic forcing to its associated response. The frequency response from the input s to the first $k = 60$ POD-modes can also be computed from the full-order model. In this case, we cannot rely on an explicit matrix expression for $\mathbf{R}_f(\omega)$. Instead, we need to apply an impulse in w to the system, compute the Fourier-transform of the responses in s and Y and finally apply the relation $\mathbf{R}_f(\omega) = \mathbf{Y}(\omega)/s(\omega)$.

In figure 3.4(a) the 2-norm of the vector $\mathbf{R}(\omega)$ at each ω (which represents the square-root of the kinetic energy of the perturbation) is shown (using a blue-solid line) for the full-order system and (using a red-dashed line) for the reduced-order model composed of $k = 60$ POD-modes. We can report a close agreement between both models over a wide (and interesting) range of frequencies. Keeping in mind that the frequency response for the full-order system has been based on an impulse on w, the former result implies that the bulk of the forcing noise is transmitted through the boundary layer and can be detected by a wall sensor. The response of the reduced-order model at a given frequency can be expressed in the

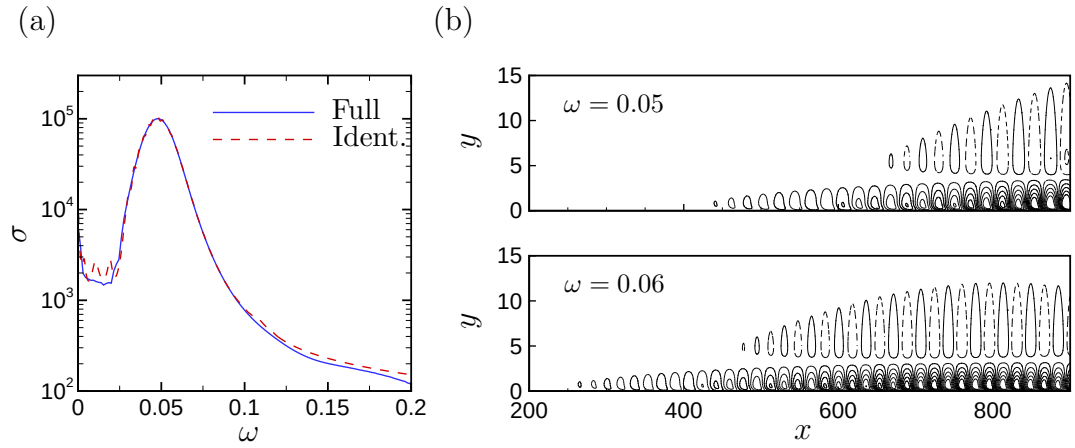

FIGURE 3.4: (a) Transfer function from s to the first 60 POD-coefficients of the full-order system (blue, solid line) and of an identified reduced-order model of size $k = 60$ (red, dashed line). (b) Streamwise component of the real part of the transfer function (frequency response) from s to the velocity field V for two given frequencies, $\omega = 0.05$ and $\omega = 0.06$. The velocity field has been reconstructed from the identified reduced-order model depicted in (a).

full-order state using, once more, the relation $\overline{\mathbf{V}}(\omega) = \mathbf{U}\overline{\mathbf{Y}}_e(\omega)$. The streamwise component of the real part of the frequency response for $\omega \approx 0.05$ and $\omega \approx 0.06$ are depicted in figure 3.4(b). The response for both frequencies is located near the wall, and decreasing wavelengths are observed as the frequency is increased. These characteristics have also been observed in the eigenmodes computed in section 3.3.2.

The two-dimensional temporal modes exhibit a growth in amplitude as they progress downstream; this growth may be quantified by computing $A(x) = \sqrt{\int_0^{y^{PIV}} |\overline{\mathbf{V}}|^2 \mathrm{d}y}$, where $|\cdot|$ denotes the complex modulus, and compared to the amplitude growth due to a convective instability, as predicted by a local stability analysis with $\mathbf{u} = \widehat{\mathbf{u}}(y)\mathrm{e}^{i(\alpha x - \omega t)}$ and ω and α as the frequency and streamwise wavenumber of the perturbation, respectively. The comparison between the streamwise growth of the global mode and the locally parallel flow prediction has been undertaken for the two frequencies depicted in figure 3.4. The corresponding $A(x)/A(0)$ are compared in figure 3.5. We notice a similar trend for the two approaches (local analyses and identified global structures), which means that a identified reduced-order model robustly captures the intrinsic dynamics of the flow. The slight disagreement between the curves can be attributed to the non-parallelism of the flow (Gaster, 1974).

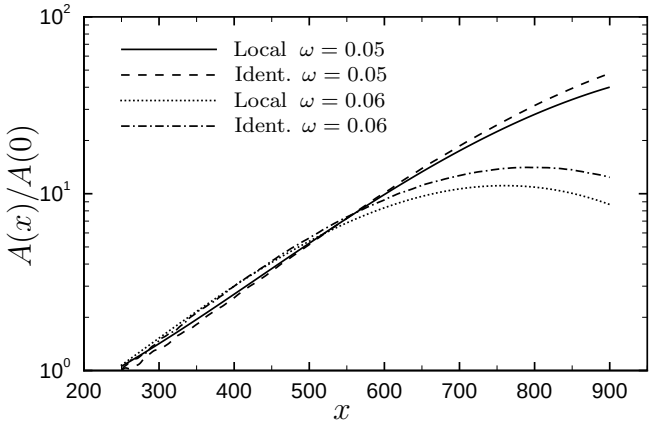

FIGURE 3.5: Normalised amplitude $A(x)/A(0)$ as a function of the streamwise distance x for the reconstructed velocity field at the two frequencies shown in figure 3.4(b); comparison with a local stability analysis (solid and dotted lines).

3.4 Computation of system matrices using system identification

An objective of this article is the recovery of the intrinsic dynamics of experimental noise amplifiers using a reduced-order observer (3.4). To this end, the unknown coefficients of the system, the matrices $\widetilde{\mathsf{A}}_s$ and $\widetilde{\mathbf{L}}$, need to be computed using a technique which solely relies on input-output data. We propose the approach introduced by (Guzmán Iñigo et al., 2014), which is based on system-identification algorithms. For the sake of completeness, a brief review of the methodology is given in this section.

3.4.1 System-identification techniques

System identification aims at determining the system matrices such that $\widetilde{\mathbf{Y}}_e(n)$ recovers as close as possible $\mathbf{Y}(n)$ from the time-series of input-output data $\{s(n), \mathbf{Y}(n)\}$ with $n = n_0, \ldots, n_f$ using statistical methods. A wide range of system-identification algorithms are available. For our case, subspace identification is a particularly convenient choice since our formulation relies on a state-space formulation (see eq. (3.4)). A detailed explanation of the algorithm is beyond the scope of this work; a comprehensive description is given, e.g., in Qin (2006). More specifically, the `N4SID`-algorithm (Van Overschee and De Moor, 1994) has been used to obtain all models in this study.

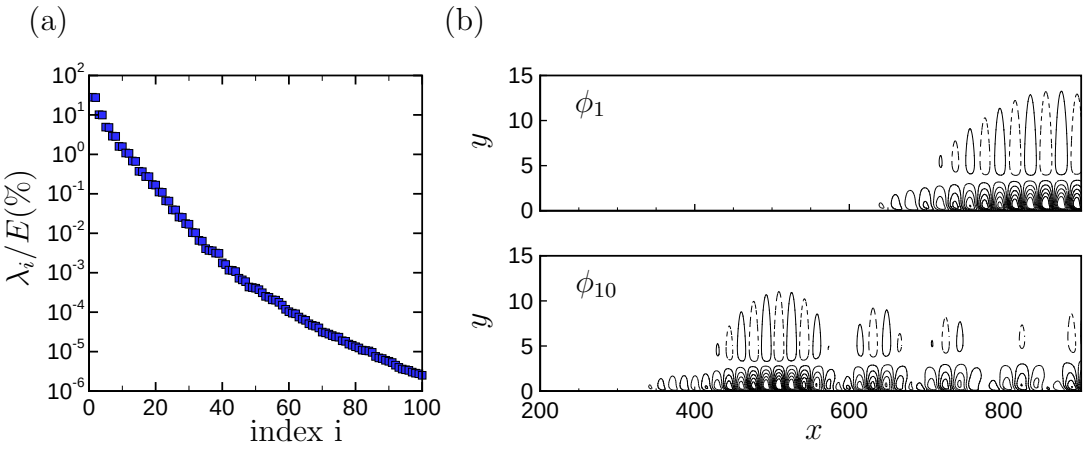

FIGURE 3.6: (a) First 100 POD eigenvalues λ_i of the correlation matrix. (b) Contours of the streamwise velocity component of the first ($\mathbf{\Phi}_1$) and tenth ($\mathbf{\Phi}_{10}$) POD-mode.

3.4.2 Direct numerical simulation for learning and testing

We obtain data for the system identification by performing a linearised direct numerical simulation of the boundary layer in the presence of unknown noise. We use a sampling interval $\Delta t = 5$ for the velocity snapshots and the shear-stress measurements s. A dataset of length $N_{snap} = 4000$ ($T = 20000$) has been extracted from the simulation. A POD-basis has been computed for each dataset using a total of 1500 snapshots. Guzmán Iñigo et al. (2014) reported that this length is sufficient to capture the slowest time scale (frequency) of the system by a factor of 8. Figure 3.6(a) shows the corresponding eigenvalues of the correlation matrix for the second case, confirming a steady decay over about three decades in the first thirty modes (95% of the energy is contained in the first ten modes). Two representative POD-modes, $\mathbf{\Phi}_1$ and $\mathbf{\Phi}_{10}$, are displayed in figure 3.6(b).

The datasets to be processed are composed of the input signal from the sensor s and several outputs y_i corresponding to the projection of the snapshots onto the basis of POD-modes $\mathbf{\Phi}_i$ (figure 3.6). Using the `N4SID` algorithm (Van Overschee and De Moor, 1994), the model parameters $\widetilde{\mathsf{A}}_s$ and $\widetilde{\mathbf{L}}$, can then be determined by fitting the model output to the true, measured output, as the model is forced by the recorded input. The ability of the model to capture the dynamics of the system is then assessed on a different part of the data. For this purpose, we use the perturbation kinetic energy $E = \langle \mathbf{u}_{snap}, \mathbf{u}_{snap} \rangle \approx \mathbf{Y}^*\mathbf{Y}$, taken from the system measurements and predicted by the model $\widetilde{E}(t)$. The quality of the model can be quantified based on the fit between the temporal evolution of both magnitudes.

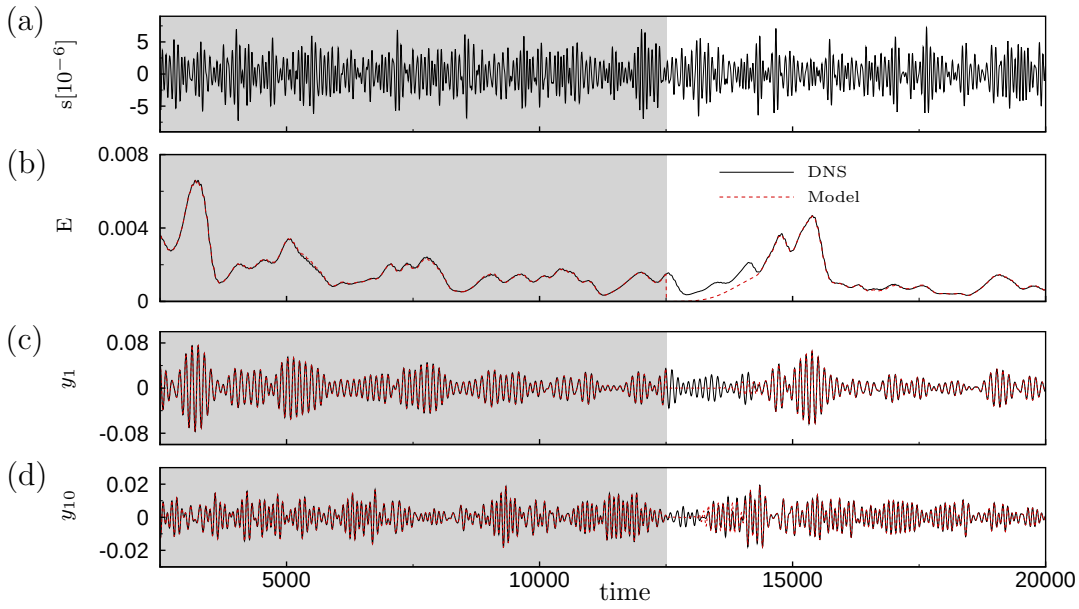

FIGURE 3.7: Learning and validation datasets: a model is obtained using a segment of the data (with length $T = 10000$ (grey box)); the performance of the model is then assessed in a different interval, initialised by $\mathbf{Y}_e = 0$ at $t = 12500$. The input of the system is (a) the measurement obtained from the wall-shear sensor s capturing the influence of external noise. (b-d) Comparison between the DNS (black) and the model prediction (red) recovered from the input for three variables: (b) the perturbation energy of the system, and (c) and (d) the POD-coefficients y_i for the first and tenth mode, respectively.

Figure 3.7 shows a reduced-order model determined using $k = 60$ POD-modes and a learning data set of length $T = 10000$. Figure 3.7(a) displays the measurement from the shear-stress sensor s from which all the subsequent variables (figure 3.7(b-d)) can be recovered using the identified model. The plotted outputs correspond to the energy (b), and the first and tenth POD-coefficients (c-d). The gray box represents the data falling within the interval $t \in (2500, 12500]$ used to compute the model to $\mathsf{FIT}_{ener} = 96.87\%$. The model is then initialised to $\mathbf{Y}_e = 0$ at $t = 12500$ and, after a transient period, the performance is evaluated within the interval $t \in (14500, 20000]$, which yields a relative match of $\mathsf{FIT}_{ener} = 97.26\%$.

3.5 Summary and conclusions

The extraction and analysis of the inherent dynamics of noise amplifiers from experimental data represents an important challenge due to the difficulty of separating the intrinsic (globally stable) behaviour from the surrounding noise environment that continuously drives and maintains the system.

A dynamic observer which accurately recovers *full-state* information from a *single* wall shear-stress measurement has been designed that relies on a POD-basis and system identification techniques. Within the limitations of linear perturbation dynamics, the design process for the dynamic observer extracts the system matrix from a sequence of snapshots and shear-stress measurements. The spectrum of the system matrix describes a globally stable flow configuration that is sustained by selectively amplified random perturbations from the noise environment. The proposed method thus successfully separates the intrinsic, stable perturbation dynamics from the external noise excitation; previously only the combined (statistically stationary) dynamics could be described.

A principal limitation, however, resides in the restriction to a linear dynamics. An extension of the present approach to nonlinear identification is possible, but its higher computational cost and difficult convergence characteristics make this extension a nontrivial undertaking.

Chapter 4

Comparison between the Kalman filter and a data-extracted estimator

An estimator of a dynamical system is a system which approximates as best as possible the state of the full system based solely on the limited information given by a sensor. In this chapter, we compare the performance of two estimators: (i) the data-based dynamic observer introduced in Chapter 2, and (ii) a Kalman filter based on an exact model. The Kalman filter is a good benchmark since it represents the optimal estimator of the state where optimal is defined in terms of minimizing the mean square estimation error.

Generally (but not always (Semeraro et al., 2013b)), the computation of a Kalman filter involves solving a Riccati equation. Nevertheless, the high number of degrees of freedom in fluid mechanics applications $\mathcal{O}(10^6)$ makes the direct computation of the Kalman filter a difficult task. To work around this issue, the order of the system is first reduced and, subsequently, the Riccati equation is solved for the reduced order model (ROM). A classical approach to obtain such a ROM is to project the full-order Navier-Stokes equations onto a reduced basis which captures the most important features of the system dynamics. Proper orthogonal decomposition (POD) and balanced proper orthogonal decomposition (BPOD)-bases have been widely used in flow control applications for this purpose (see (Noack et al., 2003; Rowley et al., 2004; Rowley and Juttijudata, 2005) for POD and (Rowley, 2005; Bagheri et al., 2009; Barbagallo et al., 2009) for BPOD). ROMs resulting

from a projection of the full-order system onto BPOD-modes guarantee stability and present *a priori* bounds for the truncation error. However, the computation of a ROM using BPOD is expensive since it requires the simulation of impulse responses of the direct and adjoint linearised-Navier-Stokes equations. An alternative technique to compute the balanced ROM is the eigensystem realisation algorithm (ERA) (Juang and Pappa, 1985; Ma et al., 2011). ERA only needs a time-evolving simulation of an impulse applied to the full-order system; the requirement of adjoint modes is avoided and, therefore, the resulting algorithm is computationally cheaper. ERA is considered to be the state of the art in reduced-order modelling and, consequently, we use this approach in the following.

We then design a Kalman filter based on this ROM. ERA yields ROMs with more states than outputs; the Kalman filter has the same dimension as the model from which it was obtained. In order to perform a *fair* comparison between the Kalman filter and the estimators obtained by identification, the size of the internal states of both estimators should be the same. However, in the previous chapters, the size of the internal states and outputs of the identified models were forced to be equal (which gave a strong physical meaning to all elements of the dynamic observer). Therefore, in this chapter, we additionally report on the potential of considering the size of the internal states of the identified system as a new parameter.

The two estimators are compared for two different settings: (i) the estimation sensor is ideal (the measurement is noise-free), and (ii) the estimation sensor is corrupted by white noise. This is motivated by the capabilities of the Kalman filter to take white noise into account. The identified observer does not have this ability and, thus, a stronger performance loss with increasing levels of noise is expected.

The chapter is organized as follows. Section 4.1 briefly reviews some concepts of systems theory. The two estimators are compared in Section 4.2 for ideal sensors and in Section 4.3 for corrupted measurements. The influence of the number of elements of the states on the identification process is studied in Section 4.4. A summary of the results and conclusions are given in Section 4.5.

4.1 Problem formulation

In this section, we introduce the concepts necessary to obtain a Kalman filter and to compare it with the identified estimator proposed in Chapter 2. Section 4.1.2 briefly introduces ERA and the resulting structure of the ROM. Section 4.1.3 presents the equations which govern: (i) an estimator, and (ii) the error between the real and estimated states. The frequency response, as well as the H_2- and H_∞-norms of a system, are defined in Section 4.1.4 to assess the performance of the estimators.

4.1.1 Configuration

In this chapter, we consider the same configuration as the one used in Chapters 2 and 3. The driving term w is still located at $(x_w, y_w) = (50, 0.95)$, while an actuator u is placed at $(x_u, y_u) = (250, 1)$. The velocity measurement Ω_{snap} has an extension of $(200, 900) \times (0, 40)$ and the estimation sensor s is located at $(x_s, y_s) = (200, 0)$.

4.1.2 Reduced-order equations based on POD output projection

As in the previous chapters, we consider the vector given by the k POD-coefficients $\mathbf{Y} = [y_1, y_2, ..., y_k]^T$ as the output of the system. The linearised Navier-Stokes equations can be reduced by a Galerkin projection onto the computed POD basis. However, a better reduced-order model can be obtained by projecting the equations onto a balanced basis and a subsequent truncation of the degrees of freedom. In systems theory, a balanced realization implies that the degree of reachability and the degree of observability of each state are the same (Moore, 1981). While not optimal, a reduced-order model obtained by balanced truncation presents a priori bounds for the error and preserves stability. Balanced truncation is not computationally feasible, so we use an approximation known as the Eigensystem Realisation Algorithm (ERA) (Juang and Pappa, 1985; Ma et al., 2011). To compute the ROM, ERA only requires the Markov parameters of a system, which we obtain by measuring the time-evolving outputs of the system ($\mathbf{Y}$, s) when an impulse is applied to each input individually (w, u) (see Belson et al. (2013)). The

details of the algorithm, as well as the performance of this system (to represent the large-scale dynamics), are given in appendix B.

The input-output relation of the full linearised Navier-Stokes equations can be approximated by the following ROM

$$\mathbf{X}(n+1) = \mathsf{A}_w \mathbf{X}(n) + \mathsf{B}\mathbf{U}(n), \tag{4.1a}$$

$$\mathbf{Y}(n) = \mathsf{C}_\mathrm{y} \mathbf{X}(n), \tag{4.1b}$$

$$s(n) = \mathsf{C}_\mathrm{s} \mathbf{X}(n), \tag{4.1c}$$

where $\mathbf{X} \in \mathbb{R}^{\mathbf{N}_\mathrm{x}}$ is the reduced state, and A_w, B, C_y and C_s are the reduced-order matrices. The vector $\mathbf{U}$ contains the two inputs of the system $\mathbf{U}(n) = \begin{pmatrix} w(n) & u(n) \end{pmatrix}^T$; the matrix B can be decomposed into $\mathsf{B} = \begin{pmatrix} \mathbf{B}_w & \mathbf{B}_u \end{pmatrix}$.

4.1.3 Equations governing the estimator and the estimation error

In this thesis, a wall measurement s is used by an estimator to obtain an approximated output $\mathbf{Y}_e$ which aims at being as close as possible to the true output $\mathbf{Y}$. Generally, a linear estimator of the ROM described by Equation 4.1 can be defined by the following equations

$$\mathbf{X}_e(n+1) = \mathsf{A}_s \mathbf{X}_e(n) + \overline{\mathbf{B}}_u u(n) + \mathbf{L} s(n), \tag{4.2a}$$

$$s(n) = \mathbf{C}_\mathrm{s} \mathbf{X}(n) + g_s(n), \tag{4.2b}$$

$$\mathbf{Y}_e = \mathbf{C}_\mathrm{y} \mathbf{X}_e(n), \tag{4.2c}$$

where the unknown term $\mathbf{B}_w w(n)$ is replaced by $\mathbf{L}s(n)$. In real life applications, the estimation sensor s is corrupted by a measurement error. Here, we model this bias by a noise $g_s(n)$ of standard deviation G. For convenience, we define G/W as the ratio between the standard deviations G and W of, respectively, the corrupting noise $g_s(n)$ and the driving term $w(n)$. The corrupting noise $g_s(n)$ can then be replaced by a new input $g(n) = Wg(n)/G$ of standard deviation W. This change of variables will prove to be very useful in comparing the transfer functions $(w \to \mathbf{Y}_e)$ (or $(w \to \mathbf{Z})$) and $(s \to \mathbf{Y}_e)$ (or $(w \to \mathbf{Z})$) since the ratio G/W for which the estimator was designed is automatically applied.

The estimation error can be defined by $\mathbf{Z} = (\mathbf{Y} - \mathbf{Y}_e)$; its evolution is then described by a dynamical system of the form

$$\begin{pmatrix} \mathbf{X}(n+1) \\ \mathbf{X}_e(n+1) \end{pmatrix} = \begin{pmatrix} \mathsf{A}_w & 0 \\ \mathsf{L}\mathsf{C}_\mathrm{s} & \mathsf{A}_s \end{pmatrix} \begin{pmatrix} \mathbf{X}(n) \\ \mathbf{X}_e(n) \end{pmatrix} + \begin{pmatrix} \mathbf{B}_w & \mathbf{B}_u & \mathbf{0} \\ \mathbf{0} & \overline{\mathbf{B}}_u & \mathbf{L}\ G/W \end{pmatrix} \begin{pmatrix} w(n) \\ u(n) \\ g(n) \end{pmatrix}, \tag{4.3a}$$

$$\mathbf{Z}(n) = \begin{pmatrix} \mathsf{C}_\mathrm{y} & -\mathsf{C}_\mathrm{y} \end{pmatrix} \begin{pmatrix} \mathbf{X}(n) \\ \mathbf{X}_e(n) \end{pmatrix}. \tag{4.3b}$$

This description of the error is a convenient choice to investigate the performance of the estimator since the norms that will be defined in Section 4.1.4 can directly be applied to Equation (4.3).

Two different methods to compute the matrices which govern the estimator dynamics are considered in this work: (i) an identification technique which extracts the matrices from time-dependent measured data (see Chapter 2), and (ii) a Kalman filter computed from the ROM (4.1). The first technique has been widely discussed in the previous chapters of this thesis, while the second one has been briefly covered in Chapter 2. A brief reminder is given in this section.

A Kalman filter is formally defined as an estimator which minimizes the mean square estimation error $\mathrm{E}\left[\mathbf{Z}(\mathrm{n}) \cdot \mathbf{Z}(\mathrm{n})\right]$, with $\mathrm{E}\left[\cdot\right]$ the expected value $\mathrm{E}\left[\mathrm{f(n)}\right] = (1/\mathrm{N_{snap}}) \sum_{\mathrm{n=1}}^{\mathrm{N_{snap}}} (\mathrm{f(n)})$ and N_{snap} the number of time-steps. It can be proven that the gain $\mathbf{L}$ which satisfies this requirement is obtained by solving a Riccati equation (see Burl (1999)). The matrix A_s is then given by $\mathsf{A}_s = \mathsf{A}_w - \mathbf{L}\mathsf{C}_\mathrm{s}$ and $\overline{\mathbf{B}}_u = \mathbf{B}_u$. For the identified estimator, the matrices A_s, $\mathbf{L}$, $\overline{\mathbf{B}}_u$ and C_s which appear in Equation 4.3 correspond to the matrices defined in Chapter 2 $\widetilde{\mathsf{A}}_s$, $\widetilde{\mathbf{L}}$, $\widetilde{\mathbf{B}}_u$ and $\widetilde{\mathsf{C}}_s$, respectively.

4.1.4 Frequency response and norms

In this section, we define the frequency response, the H_2- and H_∞-norms of a linear system. These ideas are used in Sections 4.2 and 4.3 to assess the performance of the estimators. The continuous-time formulation is the most convenient choice for the definition of these concepts; however, ERA yields a discrete-time model given by Equation (4.1). For the sake of clarity, we transform the discrete-time equations to the equivalent ones given in the continuous-time framework. For

instance, equation (4.1) reads

$$\mathrm{d}\mathbf{X}(t)/\mathrm{dt} = \mathsf{A}'_w\mathbf{X}(t) + \mathsf{B}'\mathbf{U}(t), \qquad \mathbf{Y}(t) = \mathsf{C}'_{\mathrm{y}}\mathbf{X}(t), \qquad s(t) = \mathsf{C}'_{\mathrm{s}}\mathbf{X}(t). \tag{4.4}$$

when continuous-time is used. The continuous-discrete transformation of the matrices is given in Chapters 2 and 3.

Assuming that the system is forced by a harmonic input $\mathbf{U} = \mathbf{U}_0\ \mathrm{e}^{i\omega t}$, a response is sought in the form $\mathbf{Y}(t) = \mathbf{Y}_0(\omega)\mathrm{e}^{i\omega t}$, which leads to the expression

$$\mathsf{R}(\omega) = \mathsf{C}'_{\mathrm{y}}\left(i\omega\mathsf{I} - \mathsf{A}'_w\right)^{-1}\mathsf{B}', \tag{4.5}$$

where $\mathsf{R}(\omega)$ is defined as the frequency response and links the harmonic forcing to its associated response $\mathbf{Y}_0(\omega) = \mathsf{R}(\omega)\mathbf{U}_0$.

The gain of a system can be defined as the magnitude of the output divided by the magnitude of the input at some given frequency: $\mathrm{G} = \|\mathbf{Y}_0(\omega)\|_2/\|\mathbf{U}_0\|_2 = \|\mathsf{R}(\omega)\mathbf{U_0}\|_2/\|\mathbf{U}_0\|_2$, with $\|\cdot\|_2$ denoting the Euclidean norm. For the case considered here, with the POD-coefficients as the outputs of the system, the gain G represents the perturbation energy at a given frequency. For MIMO systems, a unique gain cannot be defined, but rather a range of gains depending on the frequency ω and the input $\mathbf{U}_0$. The singular value decomposition of the frequency response $\mathbf{R}(\omega)$ determines the upper and lower bounds of the gain of a system (forced by an input of unit magnitude), which correspond to the maximum σ_{max} and minimum σ_{min} singular values, respectively (Burl, 1999). The number of singular values for an input-output system is given by $\min(N_{in}, N_{out})$, with N_{in} the number of inputs and N_{out} the number of outputs. For instance, a system with one input and several outputs only has one singular value, while the same system with two inputs has two.

The previous concepts can be used to define the H_∞-norm of the system (4.5) as follows

$$\|\mathbf{Y}\|_\infty = \max_\omega \left[\sigma_{max}\left(\mathbf{R}(\omega)\right)\right]. \tag{4.6}$$

Moreover, the trace of a matrix being the sum of the eigenvalues, the H_2-norm of the same system is defined by

$$\|\mathbf{Y}\|_2 = \sqrt{\frac{1}{2\pi}\int_{-\infty}^{\infty}\mathrm{tr}\left[\mathbf{R}^{\mathrm{H}}(\omega)\mathbf{R}(\omega)\right]\mathrm{d}\omega} = \sqrt{\frac{1}{2\pi}\int_{-\infty}^{\infty}\sum_{i=1}^{min(N_{in},\ N_{out})}(\sigma_i^2)\,\mathrm{d}\omega}, \tag{4.7}$$

where $\mathbf{R}^H$ denotes the Hermitian operation (complex conjugate transpose) of $\mathbf{R}$. Note also that the square of the H_2-norm of a system with several outputs and two inputs is given by the sum of the squares of the norms of the two systems which are obtained by considering each input separately. This can be proved by writing the frequency response as $\mathbf{R} = \begin{pmatrix} \mathbf{R}_w & \mathbf{R}_u \end{pmatrix}$. The square of the H_2-norm of the system is then given by

$$\|\mathbf{Y}\|_2^2 = \frac{1}{2\pi}\int_{-\infty}^{\infty} \left[\mathbf{R}_w^2 + \mathbf{R}_u^2\right] \mathrm{d}\omega = \|\mathbf{Y}_\mathrm{w}\|_2^2 + \|\mathbf{Y}_\mathrm{u}\|_2^2. \tag{4.8}$$

4.2 Performance with an ideal estimation sensor

In this section, we compare the performance of the identified estimator and the performance of the Kalman filter when noise-free ($g = 0$) sensors are considered. The estimation performance of both models will be assessed in Section 4.2.1, while, in Section 4.2.2, we report on the control performance when the estimators are used in a closed-loop control application.

4.2.1 Estimation

The identification of a system simultaneously forced by the inputs w and u represents a more challenging task for an identification algorithm than a system solely forced by w. This feature is naturally explained by the necessity for the algorithm to separate the effect of each input on the various outputs of the system. In order to assess the bias involved when the system is excited by both inputs, we studied the estimation ($w \neq 0$, $u = 0$) and control ($w \neq 0$, $u \neq 0$) cases separately.

Two POD-bases (one for each case) were extracted from datasets composed of $N_\mathrm{snap} = 1500$ snapshots with a sampling time $\Delta\, t = 5$ units of time . In both cases, the eigenvalues of the correlation matrix and the structure of the POD-modes are similar to the ones represented in figures 2.5 and 3.6. In the control case, the snapshots were taken with the noise w and the control signal u simultaneously forcing the system. The control signal u was selected to be a random binary signal (RBS) which excites the characteristic frequencies of the system. Two reduced-order outputs $\mathbf{Y}$, which comprise 60 and 70 components, were defined for

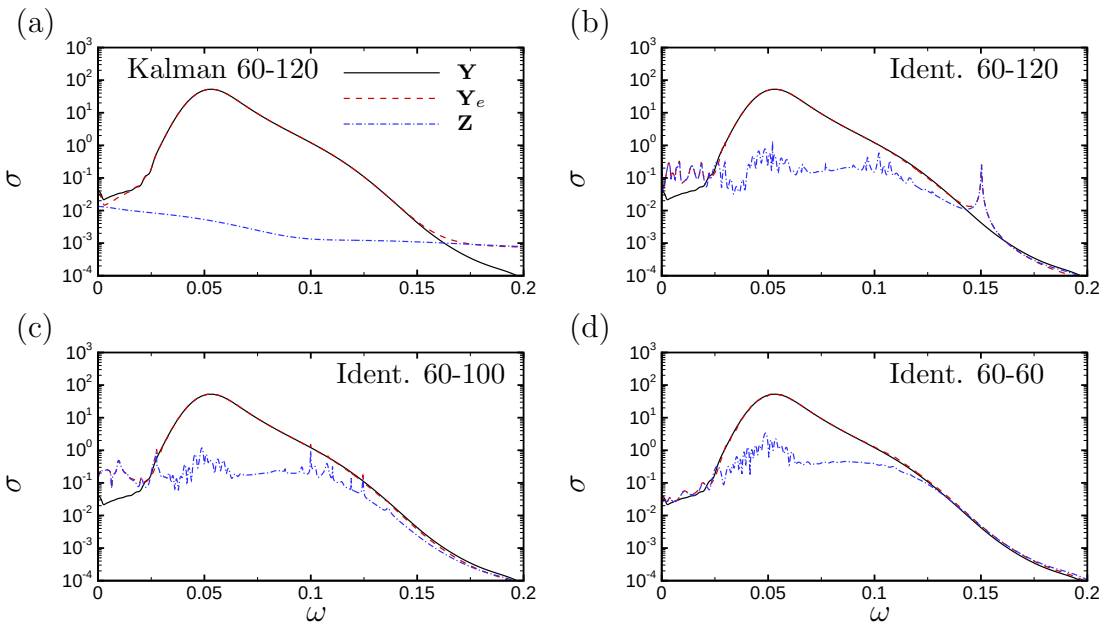

FIGURE 4.1: Comparison of the frequency response of four different models used to estimate the input-output relation from w to the first 60 POD-coefficients. (a) Kalman filter obtained from a ROM composed of 120 states, (b) identified estimator using 120 states, (c) 100 states and (d) 60 states. The black solid line represents the exact ROM obtained using ERA ($\mathbf{Y}$), while the red dashed and blue dashed-dotted lines refer to the estimator ($\mathbf{Y}_e$) and the error ($\mathbf{Z} = \mathbf{Y} - \mathbf{Y}_e$), respectively.

the estimation and control cases, respectively. Both bases capture 99.99% of the perturbation energy of the system.

A ROM (Eq. 4.1) which approximates the transfer function from w and u to $\mathbf{Y}$ was computed using ERA (see appendix B). The ROM was composed of $N_\mathrm{x} = 120$ states and yields a maximum error of 0.1% with respect to the full-order system. To compute this error, we applied an impulse to w and u individually in the full- and reduced-order systems. Subsequently, we computed the difference between the time-evolution of the outputs (the first 60 POD-coefficients) for the two impulses and we Fourier-transformed these two errors to obtain the frequency response from each input. The error relative to a given input is defined as the $H_\infty-$norm of the error divided by the $H_\infty-$norm of the full-order system. For simplicity's sake, we took the ROM as the true (full-order) transfer function in equation (4.3).

We first consider the estimation case with $u = 0$. Figure 4.1 compares the performance of four different estimators: (a) a Kalman filter computed in the large-gain limit ($G/W \ll 1$ meaning that the measurement is not corrupted) from the ROM with 60 outputs and 120 states, and (b-d) data-identified estimators based on 60

outputs and using (b) $N_{\mathrm{x}} = 120$, (c) $N_{\mathrm{x}} = 100$ and (d) $N_{\mathrm{x}} = 60$ states. In each subplot, the gain is presented as a function of frequency for the exact ROM (black solid line), the estimator (red dashed line) and the error (blue dash-dotted line) systems. The Kalman filter (a) shows a good agreement with respect to the ROM for the entire range of frequencies. This error does not account for the inaccuracies related to the model order reduction, but still remains several orders of magnitude below the error of an identified model of the same size (b). The three identified models (b-d) are extracted from the same dataset of length $N_{\mathrm{snap}} = 2000$ and match a validation dataset of length $N_{\mathrm{snap}} = 1100$ up to (b) $FIT_{\mathrm{ener}} = 99.23\%$, (c) $FIT_{\mathrm{ener}} = 99.06\%$ and $FIT_{\mathrm{ener}} = 96.06\%$, respectively. The differences for the two largest models (b-c), in terms of fit and error, are insignificant. On the other hand, the smallest model (d) presents an obvious loss of performance: the gain of the error is increased by one order of magnitude. Despite the poorer performance, the small model exhibits a smoother error across the entire range of frequencies, while the two others show strong peaks of the error at certain frequencies. This fact may stem from a slight over-fitting of the models, which is made possible due to the higher number of degrees of freedom in the state, or, in other words, the excessive addition of more states than necessary to capture the system dynamics. For the three cases, the maximum error is located around the frequency responsible for the maximum gain.

A similar comparison can be made for a system excited by w and u. In this case, a ROM composed of 120 states approximates the transfer function (from u and w to the reduced output $\mathbf{Y}$ containing 70 POD-coefficients) up to a relative error of 3 %. We identified and tested two models using a learning and a validation dataset composed of $N_{\mathrm{snap}} = 2500$ and $N_{\mathrm{snap}} = 1100$ snapshots, respectively. These datasets lead to a fit for the validatation dataset of $FIT_{\mathrm{ener}} = 98.78\%$ and $FIT_{\mathrm{ener}} = 90.18\%$ for models composed of 120 and 70 states, respectively. The obtained results are compared to a Kalman filter in Figure 4.2. The black, green, red, and blue lines represent the ROM, a Kalman filter, an identified model formed by 70 states, and an identified model formed by 120 states, respectively. The frequency responses depicted in this figure correspond to the input-output relation: (a) ($w \to \mathbf{Y}_e$), (b) ($w \to \mathbf{Z}$), (c) ($u \to \mathbf{Y}_e$) and (d) ($u \to \mathbf{Z}$). The difference of performance between the Kalman filter and the identified estimators is more noticeable in this case because the identification algorithm needs to separate the contribution of each input. The results with two inputs are nonetheless similar to the estimation case ($u = 0$):

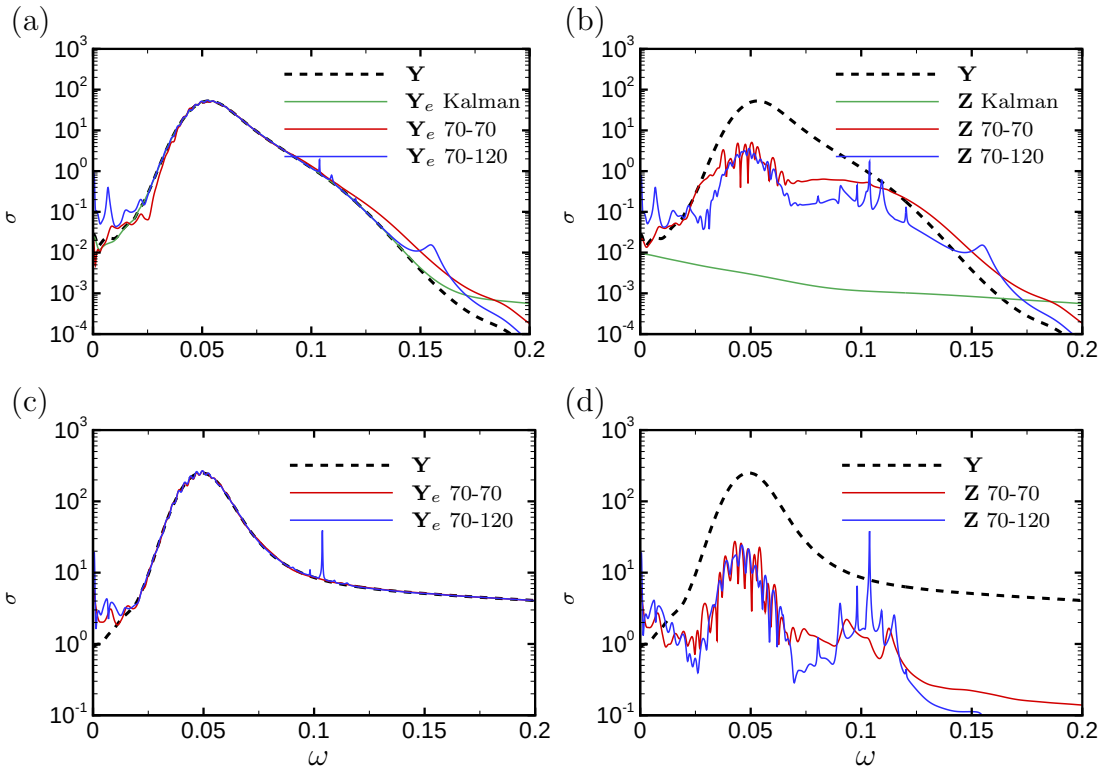

FIGURE 4.2: Comparison of the singular values of the transfer function of three different models used to estimate the input-output relation from w and u individually to the first 70 POD-coefficients: (green) Kalman filter computed from an exact ROM composed of 120 states, and identified estimators using (red) 70 and (blue) 120 states, respectively. The black dashed line represents the exact ROM based on 70 outputs and 120 states obtained using ERA. Frequency response of (a) ($w \to \mathbf{Y}_e$), (b) ($w \to \mathbf{Z}$), (c) ($u \to \mathbf{Y}_e$), and (d) ($u \to \mathbf{Z}$).

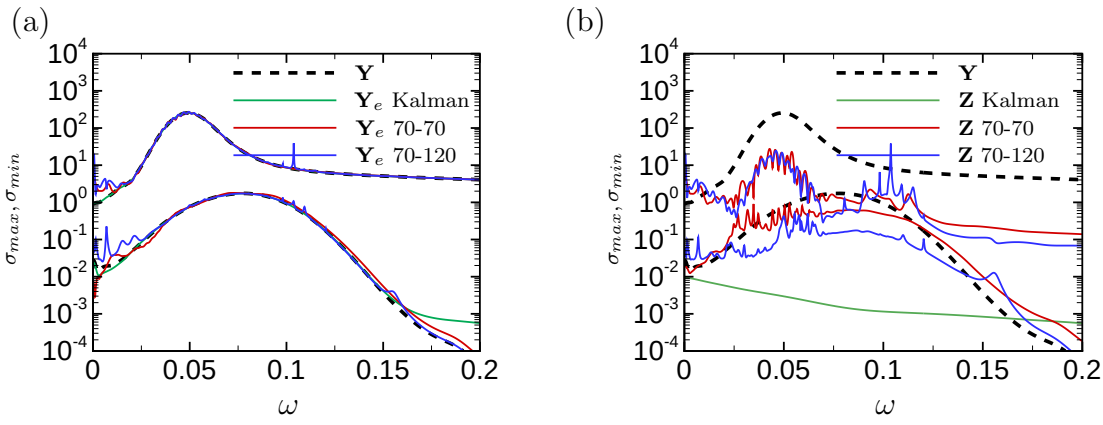

FIGURE 4.3: (a) Comparison of the singular values of the transfer function of three different models used to estimate the input-output relation from w and u to the first 70 POD-coefficients: (green) Kalman filter computed from a ROM composed of 120 states, and identified estimators using (red) 70 and (blue) 120 states, respectively. (b) Frequency response of the error system $\mathbf{Z} = (\mathbf{Y} - \mathbf{Y}_e)$ for the identified models depicted in (a).

the maximum error is located around the frequency leading to the maximum gain, and sharp error peaks are found at certain frequencies for the largest model.

The estimators with two inputs can also be studied by considering the two gains of the two inputs considered simultaneously: σ_{max} and σ_{min}. The frequency responses of $((w,\ u) \rightarrow \mathbf{Y}_e)$ and $((w,\ u) \rightarrow \mathbf{Z})$ for the three proposed estimators are presented in Figures 4.3(a) and 4.3(b), respectively. The estimation errors shown in Figure 4.2 must be inside the envelope given by Figure 4.3(b).

4.2.2 Closed-loop control

In this section, a closed-loop control strategy is considered in order to weaken or suppress the amplification of the perturbations. The approach taken in our study is based on the linear quadratic regulator (LQR) control framework already introduced in Chapter 2 (see Burl (1999)). The LQR proposes a control law of the form $u(n) = -\mathbf{K}\mathbf{X}$, which minimizes the cost functional $J = \mathrm{E}\left[\mathbf{X}(\mathrm{n})\mathsf{Q}\mathbf{X}(\mathrm{n}) + \mathrm{l}^2|\mathrm{u}(\mathrm{n})|^2\right]$, where Q is a positive definite weight matrix and l is a user-specified parameter to balance disturbance energy and exerted control energy. Following a standard procedure, the control gain $\mathbf{K}$ can be obtained by solving a Riccati equation involving A_w, $\mathbf{B}_u$, Q and l.

The state $\mathbf{X}$ is required in order to compute the control law u; however, the estimated state $\mathbf{X}_e$ may be used in its place since the former remains unknown. The combination of an LQR controller together with a Kalman filter is called Linear Quadratic Gaussian control (LQG), and the system which takes the measurement s and computes the control law u is called a compensator. Figure 4.4 shows the schematic representation of the control set-up.

The performance assessment of the compensator will follow the frequency-based framework outlined in section 4.2.1. Considering the state-space system (4.1) driven by an excitation w, the response of the compensated system reads

$$\begin{pmatrix} \mathbf{X}(n+1) \\ \mathbf{X}_e(n+1) \end{pmatrix} = \begin{pmatrix} \mathsf{A}_w & -\mathbf{B}_u\mathbf{K} \\ \mathsf{LC}_\mathrm{s} & \mathsf{A}_s - \mathbf{B}_u\mathbf{K} \end{pmatrix} \begin{pmatrix} \mathbf{X}(n) \\ \mathbf{X}_e(n) \end{pmatrix} + \begin{pmatrix} \mathbf{B}_w \\ \mathbf{0} \end{pmatrix} w(n), \tag{4.9a}$$

$$\mathbf{Y}(n) = \begin{pmatrix} \mathsf{C}_\mathrm{y} & 0 \end{pmatrix} \begin{pmatrix} \mathbf{X}(n) \\ \mathbf{X}_e(n) \end{pmatrix}. \tag{4.9b}$$

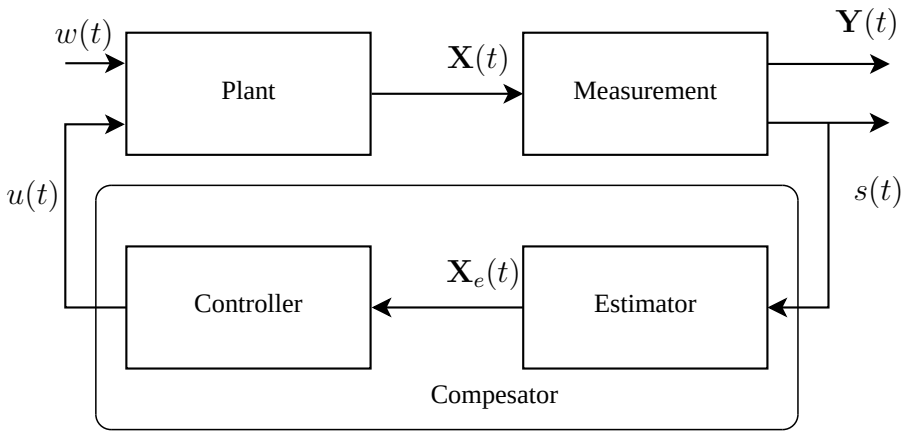

FIGURE 4.4: Sketch of the control set-up.

Since the estimation sensors were considered to be ideal ($g = 0$) in this section, the controllers are computed in the large gain limit ($G/W \ll 1$). Figure 4.5(a) compares the frequency response of the uncontrolled case (black solid line) to two controlled systems using: (i) an LQR controller (red dashed), and (ii) an LQG compensator (green dash-dotted). The control objective in all cases was chosen to be the perturbation energy $E = \mathbf{Y} \cdot \mathbf{Y}$, which leads to $\mathsf{Q} = \mathsf{C}_\mathrm{y}^T \mathsf{C}_\mathrm{y}$. The maximum gain of the system is reduced by nearly two orders of magnitude for either control strategies. It turns out that this gain is very close to the minimum open-loop gain of the system forced simultaneously by w and u (blue solid line). The good agreement between the LQR-controlled and the LQG-compensated systems indicates that the location of the sensor is optimal. This fact is not surprising: feedforward configurations are proven optimal for strongly convective noise-amplifier flows (Juillet et al., 2013).

A similar comparison can be performed with the data-based dynamic observers. Yet, in this case, to compute $\mathbf{K}$, we solve the Riccati equation involving the identified matrix $\widetilde{\mathsf{A}}_s$ instead of $\mathbf{A}_w$ [1]. The matrix $\widetilde{\mathsf{A}}_s$ corresponds to the dynamics of the estimator: we therefore compute an LQR-controller for a system with input s rather than w. In strongly convective flows, minimizing the transfer function $w \to \mathbf{Y}$ is indeed nearly equivalent to minimizing $s \to \mathbf{Y}$ since the vast majority of perturbations generated by w can be detected by s.

Figure 4.5(b) compares the compensated systems obtained by two controllers based on the two identified models depicted in Figure 4.3. The reduction of the energy

[1] In chapter 2, the matrix A_s was converted to A_w using $\widetilde{\mathsf{A}}_w = \widetilde{\mathsf{A}}_s + \widetilde{\mathbf{L}}\widetilde{\mathsf{C}}_s$. Here, we preferred to use $\widetilde{\mathsf{A}}_s$ since this approach is not robust because the identification algorithm does not exactly recover $\widetilde{\mathsf{A}}_s = \widetilde{\mathsf{A}}_w - \widetilde{\mathbf{L}}\widetilde{\mathsf{C}}_s$.

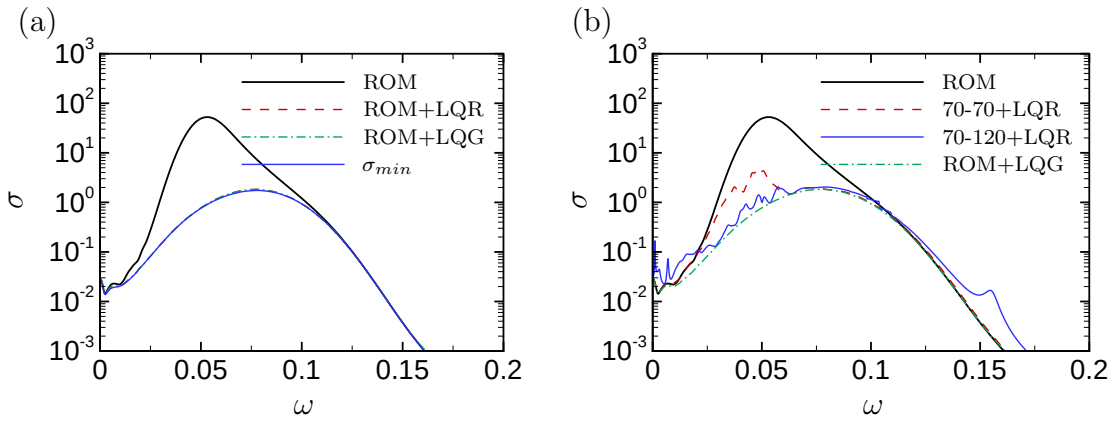

FIGURE 4.5: Frequency response of the closed-loop system. (a) The uncontrolled ERA model (black solid line) is compared to the LQR-based (red dashed line) and LQG-based (green dashed-dotted line) controlled systems. The blue solid line represents the smallest singular value of the transfer function from the inputs (u and w) to the first 70 POD-coefficients. (b) The uncontrolled ERA model (black solid line) is compared to two compensated systems using two controllers computed from identified models composed of 70 (red dashed line) and 120 states (blue solid line), respectively.

obtained with the largest model ($N_x = 120$) is very close to the one obtained with LQG control, with poorer performances for the range of frequencies where the estimation is worse. The smallest model shows a similar trend, though with an overall reduction in performance.

Finally, the performance of the three compensators considered above is assessed using a DNS simulation of the full-order system. Figure 4.6 presents the perturbation energy of the uncontrolled case (black line), the LQG (red line), and the controllers based on the identified models composed of 70 (green line) and 120 (blue line) states. An effective reduction of the mean perturbation energy of about two orders of magnitude is observed for the three cases. The ROM+LQG-compensator shows the largest reduction in energy, closely followed by the identified model composed of 120 states+LQR; and, finally, the one composed of 70 states+LQR. The differences in the control signal u are nearly unnoticeable.

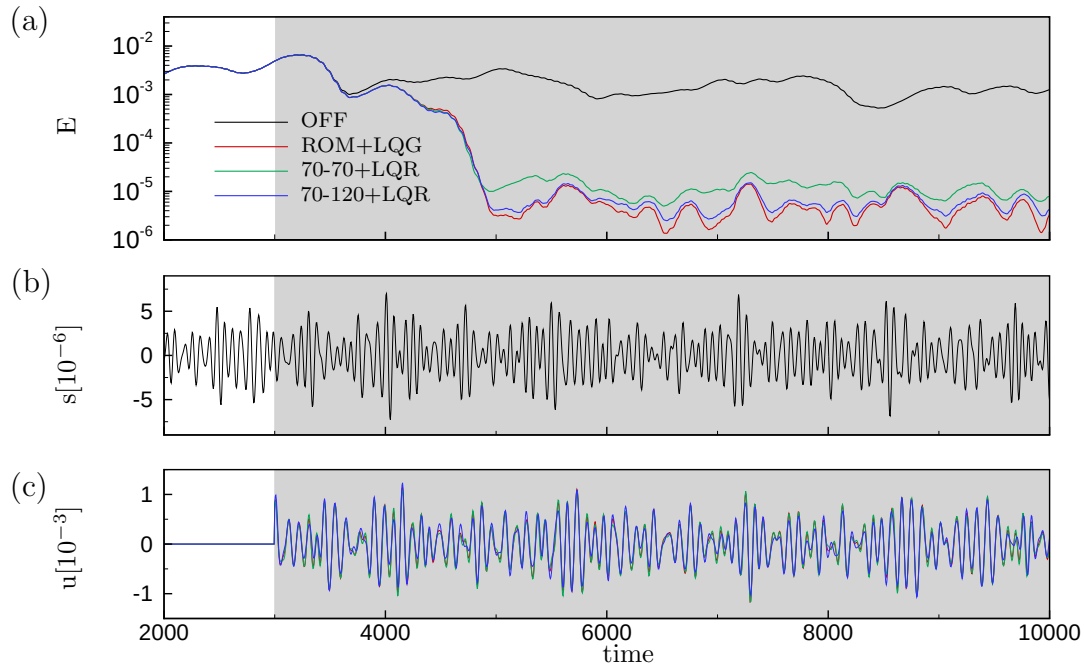

FIGURE 4.6: Results of the closed-loop simulations based on three controllers computed from three different models: (red line) LQG-based control obtained from the ERA model, and (green line) and (blue line) LQR-based controllers computed from identified models composed of 70 and 120 states, respectively. (a) Temporal evolution of the perturbation energy $E(t)$ for the uncontrolled simulation (black) and the three controlled simulations. (b) Sensor signal $s(t)$, which is the same in all simulations discussed in this figure. (c) Control signal $u(t)$ obtained for the three controllers.

4.3 Performance with noise corrupting the estimation sensor

In this section, we study the performance of the estimator when the sensor s is corrupted by white noise $g(n)$. This noise is defined by the parameter $G/S(\%)$, which represents the standard deviation of the corrupting noise G over the standard deviation of the (noise-free) measurement S. This situation is specially difficult to deal with in the case of noise amplifiers since these flows are fully governed by an external driving term. The estimation sensor, which aims at capturing the influence of the external forcing, has no mechanism to separate the corrupting noise from the physical perturbations due to the wide band of frequencies which characterises these flows. Moreover, since the system amplifies the perturbations, the estimator will amplify the corrupting noise.

Figure 4.7 depicts the frequency response of the estimation error versus the level

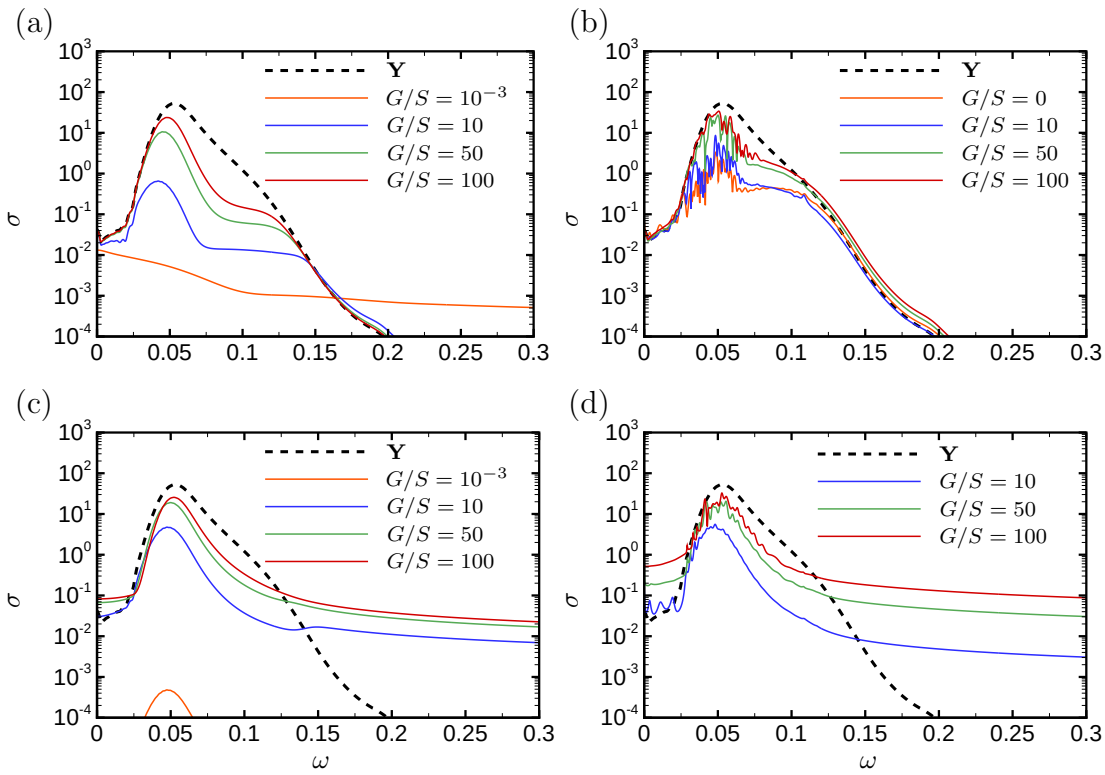

FIGURE 4.7: Performance of different estimators versus frequency using sensors corrupted by different levels of noise $G/S(\%)$. Frequency response of the estimation error $\mathbf{Z} = (\mathbf{Y} - \mathbf{Y}_e)$ for the Kalman filter: (a) $w \to \mathbf{Z}$ and (c) $g \to \mathbf{Z}$. Frequency response of the estimation error for an identified model based on 60 outputs and 60 states: (b) $w \to \mathbf{Z}$ and (d) $g \to \mathbf{Z}$.

of noise for two estimators: a Kalman filter obtained from a ROM based on 60 states and 120 outputs (Figure 4.7(a) and (c)), and an identified model of size $k = N_{\mathrm{x}} = 60$ (extracted using corrupted measurements)(Figure 4.7(b) and (d)). The corrupting noise affects the performance of the estimators via two mechanisms: (i) the error introduced directly by g (the transfer function $g \to \mathbf{Z}$), and (ii) the loss of performance indirectly caused by g (the transfer function $w \to \mathbf{Z}$). The first term is proportional to the gain of the estimator $\mathbf{L}$. Consequently, a good estimator should reduce it to improve the performance, which may yield simultaneously an increase of the error of $w \to \mathbf{Z}$. The Kalman filter balances the two contributions and delivers the optimal estimator. For the identified model, the error induced by the second term is explained by a reduction of the quality of the identification due to noise. Figure 4.7 shows that, in the large-gain limit (low level of noise), the Kalman filter is far superior to the identified models: the error is several orders of magnitude lower. In contrast, when the sensor is strongly corrupted by noise, the performance of the Kalman filter dramatically decreases and recovers the results obtained for the identified model.

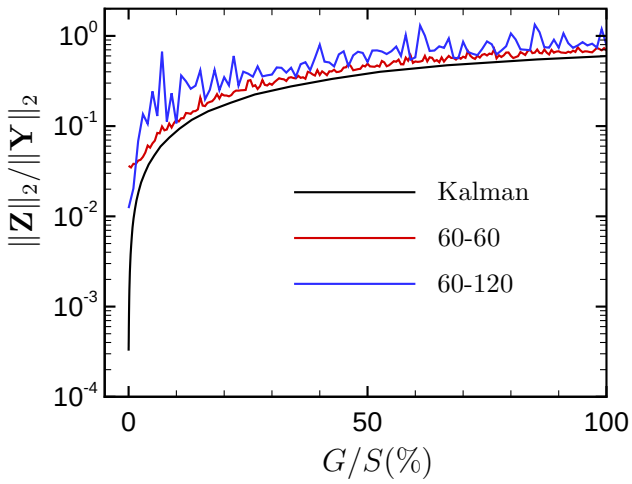

FIGURE 4.8: Comparison between the normalized performance of the Kalman filter and the identified models for different levels of noise corrupting the estimation sensor s. The identified models comprise 60 outputs and 60 states (red line), and 60 outputs and 120 states (blue line).

An instructive way of assessing the performance of an estimator across all frequencies is to directly compute the H_2-norm (see equation (4.7)) of the error system normalized by the H_2-norm of the ROM. When this quantity is close to unity, the estimation process has failed with a 100% estimation error; the smaller the value, the better performing the estimator. This quantity is displayed in figure 4.8 versus the noise parameter $G/S(\%)$ for the Kalman filter, and for two identified estimators composed of 60 and 120 states, respectively. For noise-to-signal ratios above 100%, the sensor noise prohibits a correct estimation, resulting in an estimation error close to 100%. As the noise-to-signal ratio diminishes, the performance of the estimators progressively increases until it reaches the large-gain limit. The black curve corresponds to the performance of the Kalman filter which represents the optimal estimation and, consequently, can be used to assess the capabilities of the data-extracted models. In the large-gain limit (clean sensors, $G/S \ll 1$), both identified models are far from the optimal error ($3\ 10^{-4}$); the largest model ($N_\mathrm{x} = 120$) performs better than the smaller one ($N_\mathrm{x} = 60$). However, the tendency is inverted when the level of noise is increased: the additional degrees of freedom included in the model help to obtain better results in a deterministic situation, but when the sensor is corrupted by noise the same degrees of freedom compromise the algorithm due to overlearning.

4.4 The number of elements of the state as a parameter

In Chapter 2, the number of elements of the state was selected to match the number of outputs. This constraint gave a strong physical meaning to the state of the identified system since a link to a ROM, obtained by a Galerkin projection of the governing equations onto the POD basis, can be established. In that case, a requirement for the minimum number of POD-modes was given based on the observability of the reduced basis at the sensor location: the POD-coefficients must be able to approximate the signal of the sensor s by $s(n) \approx \widetilde{\mathsf{C}}_s \mathbf{Y}(n)$. Physically, this condition implies that the basis must represent the flow at the position of the sensor. In this chapter, the number of elements of the state and the output may differ. The state $\mathbf{X}_e$ can no longer be interpreted as a projection of the velocity field onto the POD-modes, but onto an unknown basis, and the requirement for the minimum size of the system must be modified. The criterion is straightforwardly extended by considering that the unknown basis (onto which the velocity field is projected) must again be observable at the sensor location. This requirement is given by $s(n) = \widetilde{\mathsf{C}}_y \mathbf{X}_e$, where the true state $\mathbf{Y}$ has been replaced by the estimated state $\mathbf{X}_e$. However, this condition may only be verified *a posteriori* (when the estimator is available), which makes it impractical. In this section, we provide some empirical guidelines for a correct choice of the size of the system.

Figure 4.9(a) shows the FIT for the validation dataset versus the size of the state for three groups of identified models: (solid) the number of POD modes k varies with the number of states $k = N\mathrm{x}$, (dashed) and (dotted) the number of POD-modes k is fixed to 20 and 30, respectively. The measurement $s(n)$ can be reconstructed from the state of the system by the relation $\widetilde{\mathsf{C}}_s \mathbf{X}_e$, where $\widetilde{\mathsf{C}}_s$ was obtained using the least-squares technique introduced in Chapter 2. The error between the true measurement s and approximated measurement $\widetilde{\mathsf{C}}_s \mathbf{X}_e$ is depicted in Figure 4.9(b) for the three cases. The FIT obtained for the three groups of models drastically grows when the error between the true and the estimated measurement s falls below about 20%, which confirms the need for observability of the sensor. The error between the signal s and its reconstruction from the POD-modes $\widetilde{\mathsf{C}}_s \mathbf{Y}$ is also represented in Figure 4.9(b) by the + symbols. For the first model (for which $k = N_x$), the latter error should be close to the former, because the state and the

POD-coefficients are equivalent. The disagreements, however, can be explained by the error induced by the inaccuracies of the identification.

Two different trends are observed for the three cases. Cases one and three present a similar behaviour: the performance is very poor until a critical value of 40 states is reached and the FIT suddenly increases up to values close to 100 %.. The performance of case three is slightly superior to the first one; this can be explained by the extra degrees of freedom for the same number of outputs. On the other hand, the FIT of the second group grows very slowly, reaching 90 % for about 60 states; it requires 20 more states than cases one and three. The difference of behaviour is explained by the evolution of the error between the true measurement and the measurement reconstructed from the projection of the velocity field onto the POD basis $\widetilde{\mathsf{C}}_s\mathbf{Y}$ (figure 4.9(b), + symbols). For the third case, the output of the models is composed of 30 POD-coefficients, which yields an error of 40 %, while in the second case the models are composed of 20 POD-coefficients, with an error close to 100 %. In case three, the identification process converges to a basis which correctly extracts the signal from the sensor; this is not true for the second case and, hence, the identification process will have to construct a non-trivial correlation between a limited number of states and the measurement.

A rule of thumb for the choice of the size of the system is to (i) determine the number of POD-coefficients required to approximately capture the behaviour of the measurement (the same criterion as in Chapter 2), and to (ii) select a slightly larger basis to obtain better accuracy. We want to stress that this criterion is only valid for the case of ideal estimation sensors. As shown in section 4.3, the optimal choice when the sensor is corrupted by noise is a model with as many states as outputs (adding more degrees of freedom to the state may lead to overlearning).

4.5 Summary of results and conclusions

The performance of the identified dynamic observers has been assessed with respect to the Kalman filter, which is optimal in the sense of minimizing the H_2-norm of the estimation error. This has been achieved by considering the system coupling the exact dynamics of the system (ROM) and the different estimators. In order to make the comparison as fair as possible, the number of elements in the state vector has been included as a new parameter in the subspace identification algorithm.

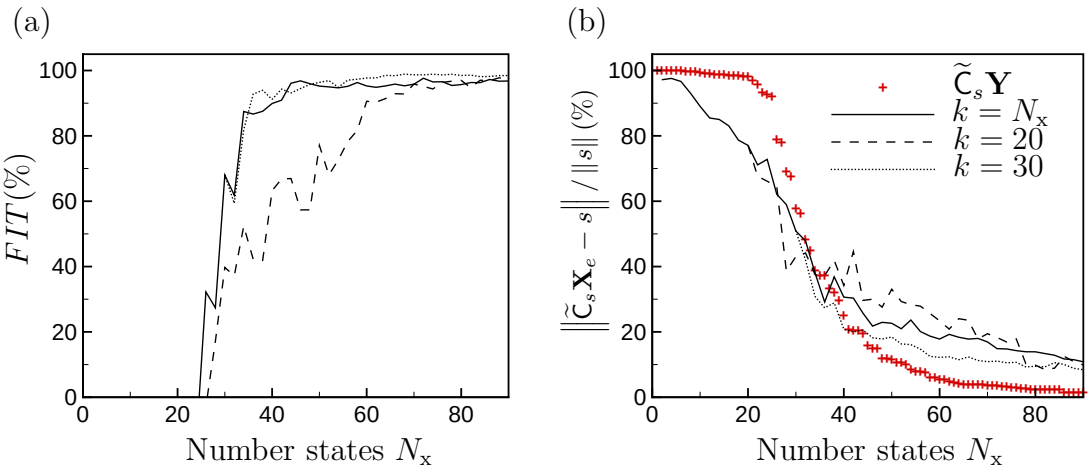

FIGURE 4.9: Influence of the number of internal states N_x on the quality of the identification. (a) Mean of the validation fit computed from samples of ten models obtained from different learning datasets. (b) Relative error between the signal $s(t)$ obtained by DNS and the signal reconstructed from the state of the system $\widetilde{\mathsf{C}}_s\widetilde{\mathbf{X}}_e(t)$ for different numbers of states N_x. Three cases have been investigated: (solid) the number of POD modes k varies with the number of states $k = N_\mathrm{x}$; and (dashed-line), and (dotted-line) the number of POD modes k is set to 20, and 30, respectively. The + symbols represent the relative error between $s(t)$ reconstructed from the exact POD coefficients $\mathbf{Y}$. $\|\cdot\|$ indicates the 2-norm on the vertical axis.

We have compared the estimators for two scenarios: (i) when the estimation sensor is ideal and (ii) when it is corrupted by noise. In the first case, the Kalman filter is far superior to the identified models across the entire range of frequencies and the error shows a flat spectrum. The identified models, on the other hand, present an error spectrum concentrated near the frequencies linked to the highest gains of the system. A better performance can be achieved by including extra states in the identification process; however, the extra degrees of freedom may lead to some overfitting by the algorithm. For the case (i), the closed-loop control performance has also been quantified. An optimal controller has been computed from the ROM and coupled to the Kalman filter to reduce the perturbation energy of the system. The results show that this strategy leads to the minimum possible gain of the system. The controllers obtained using system identification also lead to controlled systems that are very close to the minimum possible gain, with the poorest performances located in the range of frequencies with the highest estimation error.

When the estimation sensor is corrupted, the performance of the Kalman filter quickly deteriorates and tends towards the performance of the identified estimators. These identified estimators exhibit a surprising resilience to noise. Finally, we have shown that an identified model composed of as many outputs as states is

more robust to noise than a model with a state vector larger than the number of outputs.

Chapter 5

On the role of the estimation sensor on the performance of the identification

In this thesis, we propose a data-based technique to obtain reduced-order models (ROMs) for noise amplifier flows which predict the global dynamics of the flow from localized measurements. Such models have several applications, e.g., the estimation and control of the perturbation field, addressed in Chapter 2; or the recovery of the inherent dynamics of the flow (Chapter 3). For these applications, the proposed approach performs better than existing data-based techniques. Despite these encouraging results, the implementation of the dynamic observer in an experimental setting remains a challenging problem due to three main limitations inherent in experiments: three-dimensionality, non-linearities and non-ideal measurements. The first two constraints are not investigated in this thesis and are left for future work; however, we will investigate the influence of the quality of the two measurements involved in the dynamic observer, i.e., the estimation sensor and the velocity field measurement.

In this chapter, we address the influence of the estimation sensor. Specifically, we report on the effect of noise corrupting the measurement on the quality of the identification. For simplicity, the measurement error is generally modelled by white noise. However, such errors usually arise from a combination of different physical processes (e.g. electric noise from the circuitry, or external electromagnetic fields) which yield a coloured spectrum. Here, we investigate white (Section 5.2.1) and

coloured (Section 5.2.2) noise spectra. White noise was already introduced in Chapter 4 to compare the performances of the identified dynamic observer and a Kalman filter. In this chapter, we investigated the effect of the identification parameters (number of POD-modes and length of the learning dataset) on the performance of the estimation when white noise corrupts the sensor.

Another important consideration when setting up an experiment is the spatial distribution of the various sensors. In this chapter, we determine the optimal position of the sensor relative to the velocity window. The results of this study may be of help in future experimental applications of data-extracted dynamic observers.

The chapter is organized as follows. Section 5.1 addresses the study of the relative position between the estimation sensor and the velocity measurements; Section 5.2 investigates the effect of noise corrupting the measurement s; and a summary of results and conclusions is given in Section 5.3.

5.1 Influence of the position of the sensor on the estimation performance

In this section, we report on the effect of the position of the estimation sensor on the performance of the dynamic observer. We demonstrate that the absolute position of the sensor itself is not the governing parameter (at least for boundary layers), but its relative position with respect to the velocity window. Two different scenarios are studied based on the relative location of the estimation sensor and the velocity window: the estimation sensor is placed inside (Section 5.1.1) or upstream (Section 5.1.2) of the velocity window.

Here, we consider the boundary layer already investigated in previous chapters. The driving term w, as well as the actuator u, remain unchanged; the position of the different measurements is modified. Specifically, we use a shorter velocity window Ω_{snap} characterised by $(500, 900) \times (0, 40)$ and we study different positions for the estimation sensor x_s. We define a new parameter $\delta x = (x_s - x_0^{PIV})$, where x_0^{PIV} corresponds to the location of the upstream edge of the velocity window (here $x_0^{PIV} = 500$). If δx is positive, the sensor is inside the velocity window; if δx is negative, the sensor is upstream of it.

5.1.1 Sensor placed inside the velocity window

We determined three different identified estimators using 20 and 40, 40 and 40, and 60 and 60 outputs and states, respectively. Figure 5.1 presents the mean and standard deviation of the validation fit obtained from ten learning datasets versus the relative position δx for the three models. The optimal placement for the sensor is found at $\delta x = 0$, which corresponds to a sensor placed at the left edge of the velocity window. At this position, the system yields a fit of nearly 100% which gradually deteriorates as the sensor moves inside the velocity window. The performances of the three models yield identical results; hence, it does not depend on the size of the identified systems, but solely on the relative position of the elements. Further insight was gained by computing the relative error between the velocity field obtained from the DNS and the one recovered from a sensor placed at $x_s = 700(\delta x = 200)$ via the model. The relative error, depicted in Figure 5.2(c) and (d), shows that the model accurately predicts the velocity field downstream of the estimation sensor, while it fails to recover any valuable information upstream of it. This conclusion can be extended to the other positions of s.

The previous analysis was also applied to a configuration with a moving velocity window and a fixed sensor s. For the sake of brevity, the results are not included in this thesis, but the findings are equivalent. Therefore, we can conclude that the dynamic observer can only effectively estimate the velocity information located downstream of the sensor.

For a Kalman filter, on the other hand, the previous conclusions apply only partially. In the interest of a fair comparison, we considered an identified estimator of the same dimension as the Kalman filter. The Kalman filter was obtained by solving a Riccati equation (in the large gain-limit $G/W \ll 1$) based on a ROM composed of 20 outputs and 100 states. Such a ROM is computed from an impulse in w of the full-order system using ERA. Figure 5.3 shows a comparison between the performance of this Kalman filter and two identified estimators characterized by 20 outputs/100 states and 20 outputs/40 states. We can see that all models exhibit a fit close to 100% when $\delta x = 0$, which decreases as the sensor is moved downstream. Yet, for interior positions ($\delta_x > 0$), we observe that the Kalman filter is far superior to the identified models. This higher performance can be explained again by computing the relative error between the velocity field obtained from the DNS and the one recovered from a sensor placed at $x_s = 700$ via the

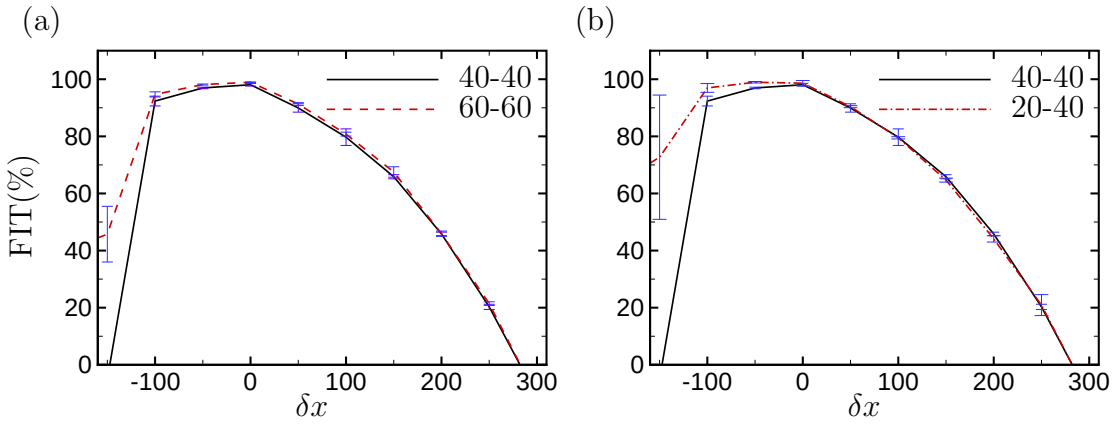

FIGURE 5.1: Influence of the relative position of the sensor with repect to the velocity window $\delta x = (x_s - x_0^{PIV})$ on the quality of the identification. (a-b) Mean and standard deviation of the validation fit computed from samples of ten models obtained from different learning datasets. The velocity window position is fixed at $x_0^{PIV} = 500$; the sensor position varies between $x_s = 350$ to $x_s = 800$. (a) The identified models are composed of (solid) 40 outputs and 40 states, and (dashed) 60 outputs and 60 states. (b) The identified models are composed of (solid) 40 outputs and 40 states, and (dashed) 20 outputs and 40 states.

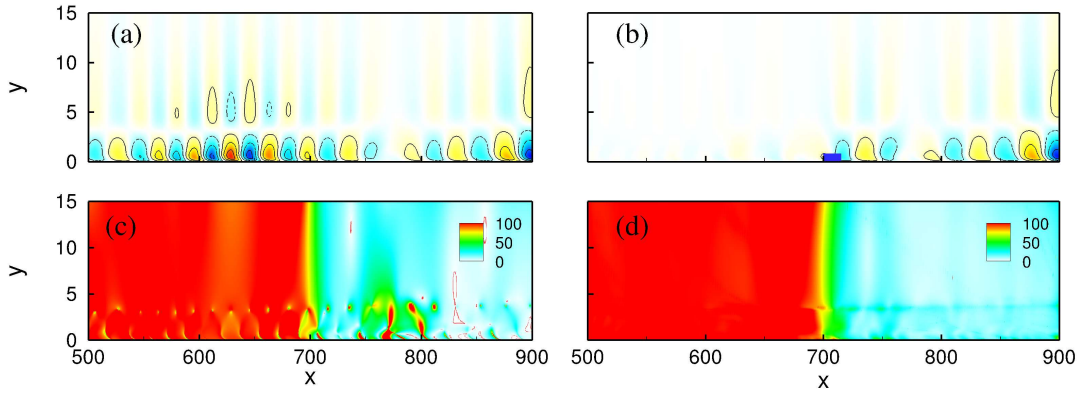

FIGURE 5.2: Snapshot of the streamwise disturbance velocity component obtained (a) from the DNS and (b) recovered from $s(t)$ via an identified model composed of 40 outputs and 40 states for $t = 20000$. The model computes the input-output relation between a sensor placed at $x_s = 700$ and a velocity window extending from $x_0^{PIV} = 500$ to $x_f^{PIV} = 900$. The blue box represents the position of the sensor. (c) Relative error between the two velocity snapshots. (d) Temporal mean of the relative error from $t = 20000$ to $t = 25000$.

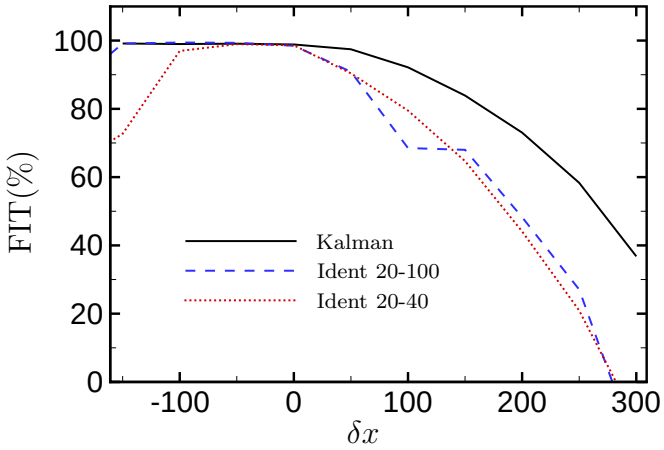

FIGURE 5.3: Influence of the relative position of the sensor with respect to the velocity window $\delta x = (x_s - x_0^{PIV})$ on the quality of the estimation using a Kalman filter. The configuration is the same as in Figure 5.1. The black solid line stands for the validation fit obtained for the Kalman filter. Comparison with identificatied estimators: mean of the validation fit computed from samples of ten models obtained from different learning datasets using (blue dashed) 20 outputs and 100 states, and (red dotted) 20 outputs and 40 states.

Kalman filter. Figure 5.4 depicts this error (c) at the time instant $t = 20000$ and (d) time-averaged over the interval $t \in (20000\ 25000]$. For this case, the velocity field is also correctly estimated in the region that is situated closely upstream of the sensor, which explains the better fit and performance of the Kalman filter. Although this result may seem surprising (the estimator does not receive any information about the perturbation before it reaches the sensor), the Kalman filter is capable, to some extent, of predicting future states of the system. This ability can be explained by the *a priori* knowledge of statistical information of the driving term that is required for its computation: the variance of the noises w and g. Here, this forecasting skill translates into upstream *visibility*.

The mean fit of the identified model depicted in Figure 5.3 presents an unexpected feature when $\delta x = 100$: the performance is lower than for $\delta x = 150$. Again, we believe that this fact arises from the over-fitting of the model. This hypothesis is corroborated by the results in Figure 5.3, obtained for an identified model that is formed by the same number of outputs but only by 40 states; the results are overall similar, but smoother.

Going back to Figure 5.1, we see that, for negative δx, the identification fails. This situation corresponds to the estimation sensor placed upstream of the velocity window. In this case, a time-delay exists between the measurement s and all states

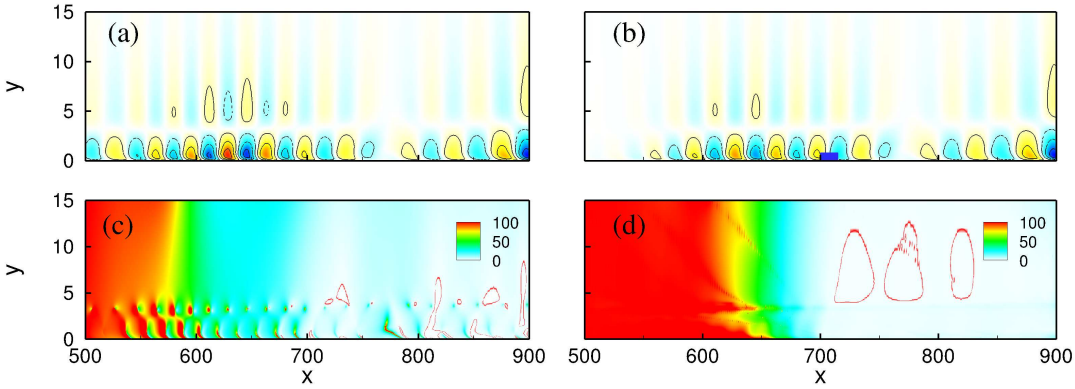

FIGURE 5.4: Snapshot of the streamwise disturbance velocity component obtained (a) from the DNS and (b) recovered from $s(t)$ via a Kalman filter composed of 20 outputs and 100 states for $t = 20000$ with the same configuration as in Figure 5.2. (c) Relative error between the two velocity snapshots. (d) Temporal mean of the relative error from $t = 20000$ to $t = 25000$.

of the system, which explains the failure. Adding further elements to the state of the system may solve the problem: the supplementary degrees of freedom may be used to account for the delay. Figure 5.3 illustrates this statement: at $\delta x = -150$, an identified model based on 40 states fails to recover the system dynamics, while a model which includes 60 additional states ($N_\mathrm{x} = 100$) successfully captures it. However, this solution requires the addition of many unnecessary states. A more natural way of taking the time-delay into account is to explicitly include it into the structure of the identified model. This strategy is investigated in the next section.

5.1.2 Sensor placed upstream of the velocity window

By placing the estimation sensor at $x = 200$ ($\delta x = -300$), as previously stated, the instantaneous measured velocity field exhibits a time-delay with respect to the estimation measure. For ROMs composed of as many states as outputs, the state of the model is a projection of the velocity field onto the POD-modes and, consequently, it is delayed with respect to the measurement s. Due to this fact, the identification fails to recover a valid model. To solve this problem, we explicitly include a time-delay n_d in the state-space formulation of the system

$$\widetilde{\mathbf{Y}}_e(n+1) = \widetilde{\mathsf{A}}_s \widetilde{\mathbf{Y}}_e(n) + \widetilde{\mathsf{L}} s(n - n_d). \tag{5.1}$$

Figure 5.5 shows the performance of the identified models versus the time-delay. An optimum is found at $n_d \approx 140$ (or $t_d \approx 700$ in time units); the performance

quadratically decays for greater delays, and the estimation fails for smaller ones. These results are reminiscent of the results obtained for a moving estimation sensor (Figure 5.1), suggesting that the time delay can be interpreted as a virtual change of position of the sensor.

More insight can be gained by applying an impulse in w and observing the evolution of a wave-packet. Figure 5.6 depicts the time-evolving measurement of the impulse response recorded by two sensors: (a) the sensor used to identify the models, $x_s = 200$; and (b) a sensor located at the left edge of the velocity window, $x = 500$. The wave-packet disperses while evolving downstream which makes it difficult to accurately determine the time that it takes to propagate from one sensor to the next. To work around this issue, we defined the energy-weighted x centroid $x_c = \int_\Omega(\mathbf{u}^2\ x\mathrm{dv})/\int_\Omega(\mathbf{u^2}\ \mathrm{dv})$. The instant at which the centroid reaches the sensors is represented by the vertical black lines in figure 5.6, and corresponds to $t = 352$ and $t = 1100$ for $x_s = 200$ and $x = 500$, respectively. The time it takes the centroid to go from one sensor to the other is $\Delta t = 748$, which is in close agreement with the time-delay leading to the best performance in Figure 5.5: $t_d = 700$. We thus conclude that, for a configuration where the estimation sensor is located far upstream of the velocity window, the state-space model requires a time-delay equal to the travelling time of a wave-packet from the estimation sensor to the upstream edge of the velocity window, which corresponds to the optimal position to place a sensor with zero delay.

In experimental situations, the external driving term w is unknown and, generally, is continuously forcing the flow. It is thus not possible to apply an impulse to the system and, consequently, it is difficult to determine the convective velocity of a wave-packet using the previous methodology. An alternative approach is to use the cross-correlation of two signals: the measurements from the estimation sensor and from a sensor placed at the left edge of the velocity window. The cross-correlation of two signals $x(n)$ and $y(n)$ of length N is defined by

$$R_{xy}(m) = \sum_{1}^{N-m} x(n+m)y(n). \tag{5.2}$$

The maximum (or minimum, in case the functions are negatively correlated) of the cross-correlation function indicates the point in time where the signals are optimally aligned, i.e., the time delay between them. Figure 5.7 represents the cross-correlation function of the two sensors previously considered. The maximum

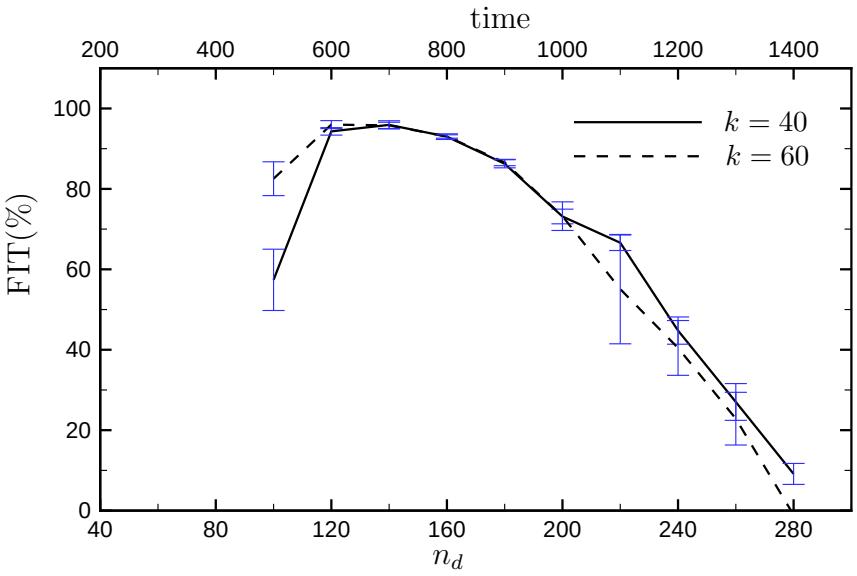

FIGURE 5.5: Mean and standard deviation of the validation fit computed from samples of ten models obtained from different learning datasets for different time-delays n_d introduced in the state-space model. The estimation sensor is placed at $x_s = 200$ and the velocity window extends from $x_0^{PIV} = 500$ to $x_f^{PIV} = 900$, which implies a relative position $\delta x = -300$. The investigated models have as many outputs as states.

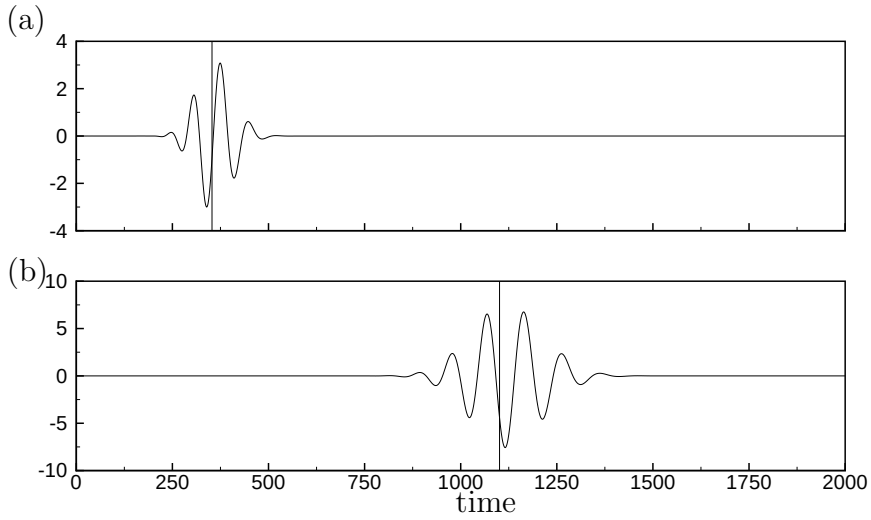

FIGURE 5.6: Measured impulse response at two sensor locations: (a) $x_s = 200$ and (b) $x = 500$. The solid black vertical lines indicate the times when the energy-based $x-$centroid of the wavepacket x_c reaches the sensor.

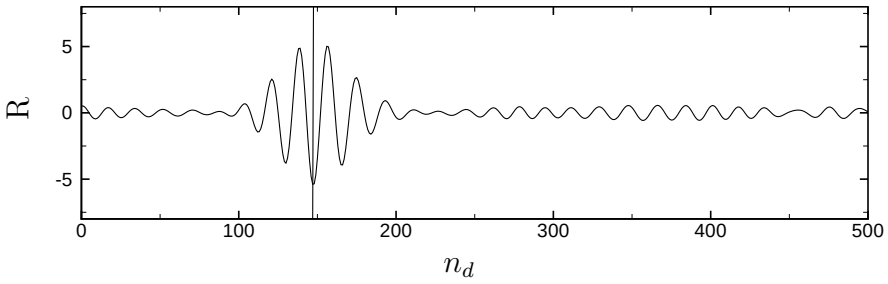

FIGURE 5.7: Cross-correlation between the signals measured from two sensors placed at $x_s = 200$ and $x = 500$, respectively. The solid black vertical line indicates the maximum value of the cross-correlation function and corresponds to a delay of $n_d = 147$ ($t = 735$).

of the absolute value of the function corresponds to $n_d = 147$ ($t_d = 735$ in time units) which is close to the time determined using the impulse response of the full-order system $t_d = 748$.

We now turn to the minimum number of POD-modes required to obtain a valid model when a time-delay is introduced in the state-space formulation of the identified system. Figure 5.8(a) shows the mean and standard-deviation of the validation fit for ten models versus the number of POD-modes; the selected time-delay is the optimal one: $n_d = 140$. For models with only few modes, the identification fails to recover any valid information. Beyond a threshold number of POD-modes, the model successfully recovers the flow dynamics. Here, this threshold value corresponds to 20 POD-modes. To interpret this result, the criterion given in previous chapters, which requires the observability of the sensor by the basis, must be adapted. We propose that the time-delayed signal of the sensor must be observable by the basis: $s(n - n_d)$ must be well represented by $\widetilde{\mathbf{C}}_s\mathbf{Y}(n)$. The matrix $\widetilde{\mathbf{C}}_s$ can be obtained by solving the following overdetermined linear system

$$\left(\mathbf{Y}(1 + n_d), \cdots, \mathbf{Y}(N_{\text{snap}} + n_d)\right)^T \widetilde{\mathbf{C}}^T = \left(s(1), \cdots, s(N_{\text{snap}})\right)^T . \tag{5.3}$$

Figure 5.8(b) shows the relative error between the time-delayed measurement of the estimation sensor $s(n - n_d)$ and the reconstruction $\widetilde{\mathbf{C}}_s\mathbf{Y}(n)$. The relative error never falls below 60 %. This stems from the fact that the boundary layer filters certain frequencies as the perturbation passes from the estimation sensor to the velocity window and, consequently, those filtered frequencies (present in s) cannot be correlated to the velocity snapshots further downstream. On the other hand, the error for an estimation sensor placed at $x_s = 500$ with a zero-time-delay ($n_d = 0$) drops below 10% when more than 20 POD-modes are used. This result

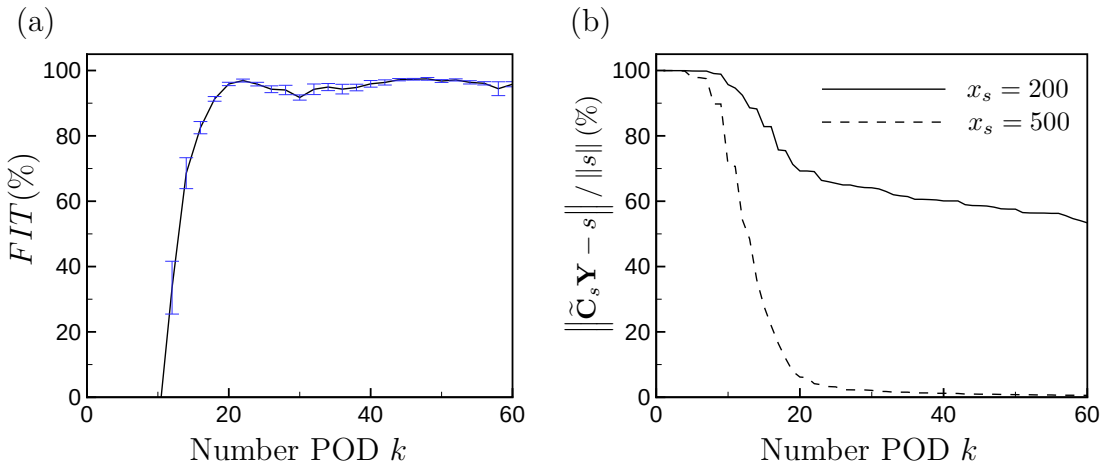

FIGURE 5.8: (a) Mean and standard deviation of the validation fit computed from samples of ten models obtained from different learning datasets for the configuration investigated in figure 5.5 and a delay $n_d = 140$. The investigated models have as many outputs as states. (b) Relative error between the signal $s(n - n_d)$ obtained by DNS and the signals given by $\widetilde{\mathbf{C}}_s\mathbf{Y}(n)$ for different numbers of POD modes and for two different positions of the sensor: (solid) $x_s = 200$, $n_d = 140$, and (dashed) $x_s = 500$, $n_d = 0$. $\|\cdot\|$ indicates the 2-norm.

suggests that the appropriate number of POD modes (even in the case of an upstream-placed estimation sensor) corresponds to the number of modes required to accurately predict the signal of a sensor placed at the left-edge of the velocity window.

5.2 Effect of noise corrupting the sensor

In Chapter 4, we investigated the effect of noise corrupting the estimation sensor on the performance of two estimators: an identified model and a reduced-order Kalman filter. The motivation in that case was to compare both estimators over a wide range of working conditions. Here, we report on a similar study with a different objective: we aim at providing guidelines for a future experimental implementation.

Noise corrupting the estimation sensor was proven to be particularly harmful for noise-amplifier flows. In Section 4.3, we determined that two factors contribute to the loss of estimator performance: (i) the error introduced directly by g ($g \to \mathbf{Z}$) and (ii) the one introduced indirectly during the more difficult learning process. The magnitude of the error arising from the first source is similar for both the identified model and the Kalman filter. In contrast, the error produced indirectly

by g is more significant for the identified estimator than for the optimal estimator (Kalman filter): the quality of the identification is greatly deteriorated by the presence of noise. To improve the performance of identified estimators in the case of noisy sensors, we investigated in Section 5.2.1 the effect of selected parameters, i.e, the number of POD-modes and the length of the learning datasets, on the identification process.

Commonly, white noise is considered a good model for the measurement error. In reality, however, it is coloured for most sensors. Section 5.2.2 deals with coloured noise corrupting the sensor. This study provides useful information about the colour of the noise sources that are most detrimental for the estimator.

We consider the same configuration as in Chapter 4: the estimation sensor s is placed at $x_s = 200$ and the velocity window extends over the rectangle $(200, 900) \times (0, 40)$.

5.2.1 White noise

A corrupting white noise $g(n)$ was added to the measurement of the estimation sensor. The amplitude of the noise is given by the parameter $G/S(\%)$, which defines the ratio between the rms-value of the noise G and the clean measurement S. Furthermore, we added white noise to both the learning and validation datasets. Figure 5.9(a-b) shows the time evolution of the signal s corrupted by different levels of noise: (a) $G/S = 10\%$ and (b) $G/S = 50\%$. The effect of the noise on the estimation performance is illustrated in Figure 5.9(c). A dataset of length $N_{snap} = 1000$ snapshots was used to identify, in the presence of noise, the two models composed of $k = 70$ outputs and 70 states. As expected, a higher level of corrupting noise leads to lower performance. More specifically, the model obtained with 10% of noise matches the dataset depicted in Figure 5.9(c) to $FIT_{ener} = 66.50\%$ and the model obtained with 50% to $FIT_{ener} = -18.52\%$. In view of this fit, it appears, at first sight, that the identification process has completely failed for the second case; however, if we look at the velocity field, this conclusion is not true. Figure 5.10 depicts the velocity field at $t = 20000$ and $t = 23500$ (a) obtained from the DNS, and (b) and (c) recovered from the identified models in presence of 10% and 50% of corrupting noise, respectively. As we can observe the results predicted by the first model are rather close to the DNS. In the second case, there are some important differences, but the model manages to capture the

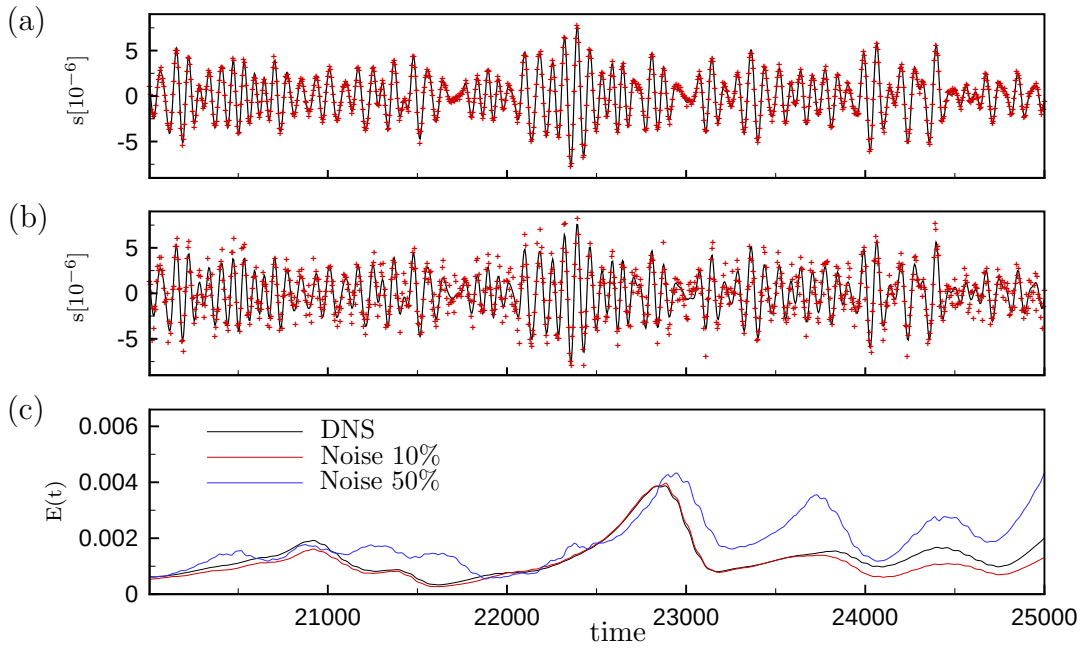

FIGURE 5.9: (a-b) Noisy signal s corrupted by 10% and 50% of the rms of s, respectively. The black solid lines represent the exact noise and the red symbols the corrupted signal. (c) Temporal evolution of perturbation energy of the system obtained (black) from the DNS, and (red) and (blue) recovered from the noisy signals (a) and (b) via identified models.

general behaviour of the velocity field. These results show that matching based on energy is a quite demanding criterion to quantify the performance of an estimator. In experimental configurations, an alternative indicator may be the norm of the error system introduced in Chapter 4. For instance, a model obtained with the estimation sensor corrupted by 100% of noise matches the validation dataset to $FIT_{ener} = -10\%$, while the norm of the error is $\|\mathbf{Z}\|_2/\|\mathbf{Y}\|_2 \approx 60\%$. For a system subjected to a stationary white noise input w, the norm of the error system $\mathbf{Z}$ is approximated by $\|\mathbf{Z}\|_2^2 = \mathrm{E}\left[\mathbf{Z}^{\mathrm{T}}(\mathrm{n})\mathbf{Z}(\mathrm{n})\right]/\mathrm{S_w}$, with $\mathrm{E}[\cdot]$ the expected value and S_w the spectral density of w. Nevertheless, evaluating this norm requires rather long validation datasets.

We now turn our attention to the influence of the identification parameters when the estimation sensor is corrupted by noise. To this end, we computed again the mean and standard deviation of the validation fit for ten models obtained from different learning datasets for each value of the parameter of interest. The total simulation has a length of $N_{snap} = 5000$ snapshots (25000 time-units), and the validation dataset is chosen within $t = 20000$ and $t = 25000$. The models were identified using ten learning datasets of length $N_{snap} = 2000$ snapshots (10000 time-units) with an overlap between consecutive datasets equal to 95%.

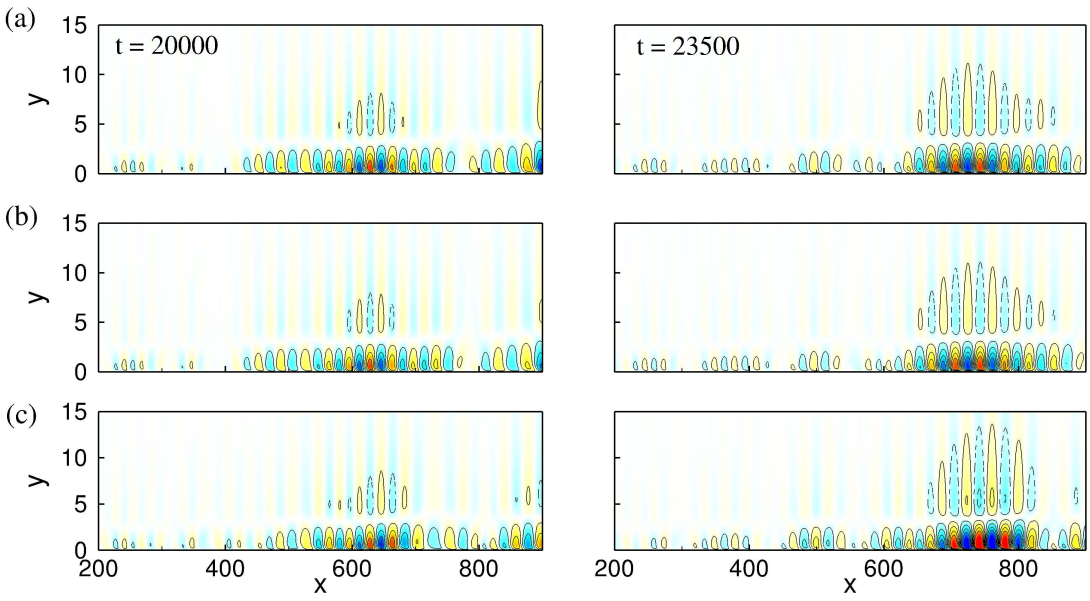

FIGURE 5.10: Snapshots of the streamwise disturbance velocity component obtained (a) from the DNS, and (b) and (c) recovered from the noisy signal s(n) via the model for $t = 20000$ and $t = 23500$. The signals $s(n)$ are corrupted by 10% and 50% of the rms of s for (b) and (c), respectively.

Figure 5.11(a) shows the performance of the identification process versus the corrupting noise level for models obtained from the described datasets and composed of 40, 50 and 70 outputs (and states). The performance, as expected, diminishes as the level of noise increases; however, no effect is noticed when increasing the number of POD-coefficients involved in the identification process. Figure 5.11(b) illustrates the influence of the length of the learning dataset on the quality of the identification. In this case, $k = 90$ POD-modes are included in the model, and the length of the learning dataset varies from $N_{snap} = 1000$ to $N_{snap} = 3000$ snapshots with the maximum overlap between consecutive portions equal to 97.5%. The performance drop due to corrupting noise is more pronounced for the shortest learning dataset, i.e., $N_{snap} = 1000$. Yet, for datasets longer than $N_{snap} = 2000$ snapshots, the performance remains the same, so that additional data does not translate into further improvement.

Finally, we used the models obtained in presence of noise to design an effective controller seeking to reduce the perturbation energy of the boundary layer. The control framework is the same as already introduced in chapters 2 and 4: the identified models are introduced in a Riccati equation to obtain the control gain $\mathbf{K}$ which minimizes the perturbation energy; the control law is given by the expression $u(n) = -\mathbf{K}\mathbf{Y}_e(n)$, where $\mathbf{Y}_e(n)$ is obtained by time-marching the identified

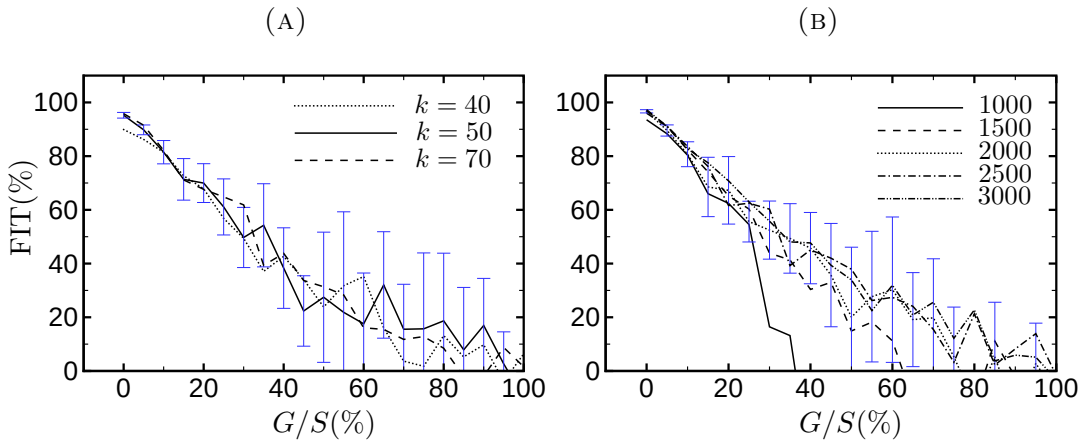

FIGURE 5.11: Mean and standard deviation of the validation fit computed from samples of ten models obtained from different learning datasets for estimation sensors corrupted by different levels of noise. (a) The considered models are extracted from learning datasets of length $L = 2000$ and comprise as many outputs as states: (dotted) $k = 40$, (solid) $k = 50$ and (dashed) $k = 70$, respectively. (b) The models comprise 90 outputs and 90 states and are computed from learning datasets of different lengths: (solid) $L = 1000$, (dashed) $L = 1500$, (dotted) $L = 2000$, (dash-dotted) $L = 2500$ and (double-dash-dotted) $L = 3000$.

dynamic observer. The controllers are then introduced into the DNS simulation and used with corrupted estimation measurements. Figure 5.12 depicts the performance of the controllers for different levels of noise: the mean of the perturbation energy in the interval $t \in (5000,\ 8000]$ is reduced by 99.6%, 98.14%, 77.17% and 53% for noise levels of 0%, 10%, 50%, 100%, respectively. The performance of the controller is reduced as the amplitude of the noise is increased. However, the controllers are remarkably robust in terms of performance: a significant reduction of the energy is obtained even with noise at the same level as the measurement. Feed-forward control theoretically guarantees infinite stability robustness margins of the compensated system; in other words, the controller never renders the system unstable for these configurations. Nevertheless, there is no theoretical result concerning the performance-robustness, i.e., the ability of the controller to achieve (to a certain extent) the task it has been designed to accomplish. We believe that, in our case, the successful control observed for high levels of noise is due to the sufficiently accurate prediction of the structures of the velocity field (see Figure 5.10).

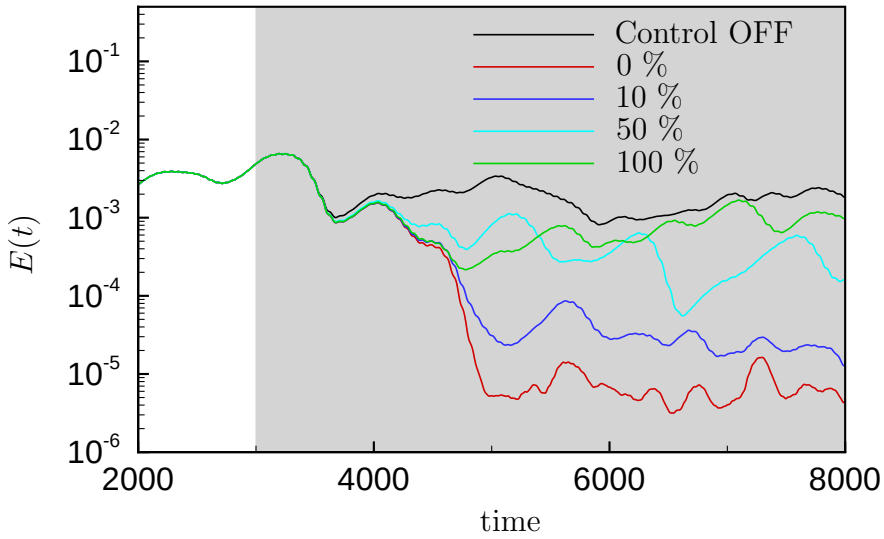

FIGURE 5.12: Effect of noisy sensors on the overall controller performance, measured by the perturbation energy. Noise levels are expressed in percentage of the rms of the exact signals.

5.2.2 Coloured noise

In this section, coloured noise was added to the estimation sensor. To obtain such a noise, we generated a white noise and subsequently filtered it to retain a user-specified band of frequencies. The rms-value of the signal is reduced by the filtering process; we therefore rescaled the amplitude of the signal to obtain the same rms-value as the original white noise. Following this methodology, we obtain noise with the same rms-value, but with a higher spectral content in specific frequency bands.

Figure 5.13(a) depicts the frequency content of three corrupting noises. The blue line, hereafter called low-frequency noise, is filtered to remove the frequencies higher than $\omega_c = 0.02$, the red line (denoted high-frequency noise) to remove the frequencies lower than $\omega_c = 0.18$, and the green line (medium-frequency noise) by a pass-band filter covering the range $\omega \in [0.04\ 0.05]$. The amplitudes were selected as $G/S = 100\%$, $G/S = 20\%$ and $G/S = 500\%$, for the low-, medium- and high-frequency noise, respectively. The temporal evolution of the corrupted measurements is presented in Figure 5.13(b-d). The low- and high-frequency-noise-corrupted measurements are greatly distorted due to the selected amplitudes. On the other hand, the differences between the measurement corrupted by medium-frequency noise and the measurement without any noise are rather insignificant. Under these circumstances, we may expect a successful identification using the

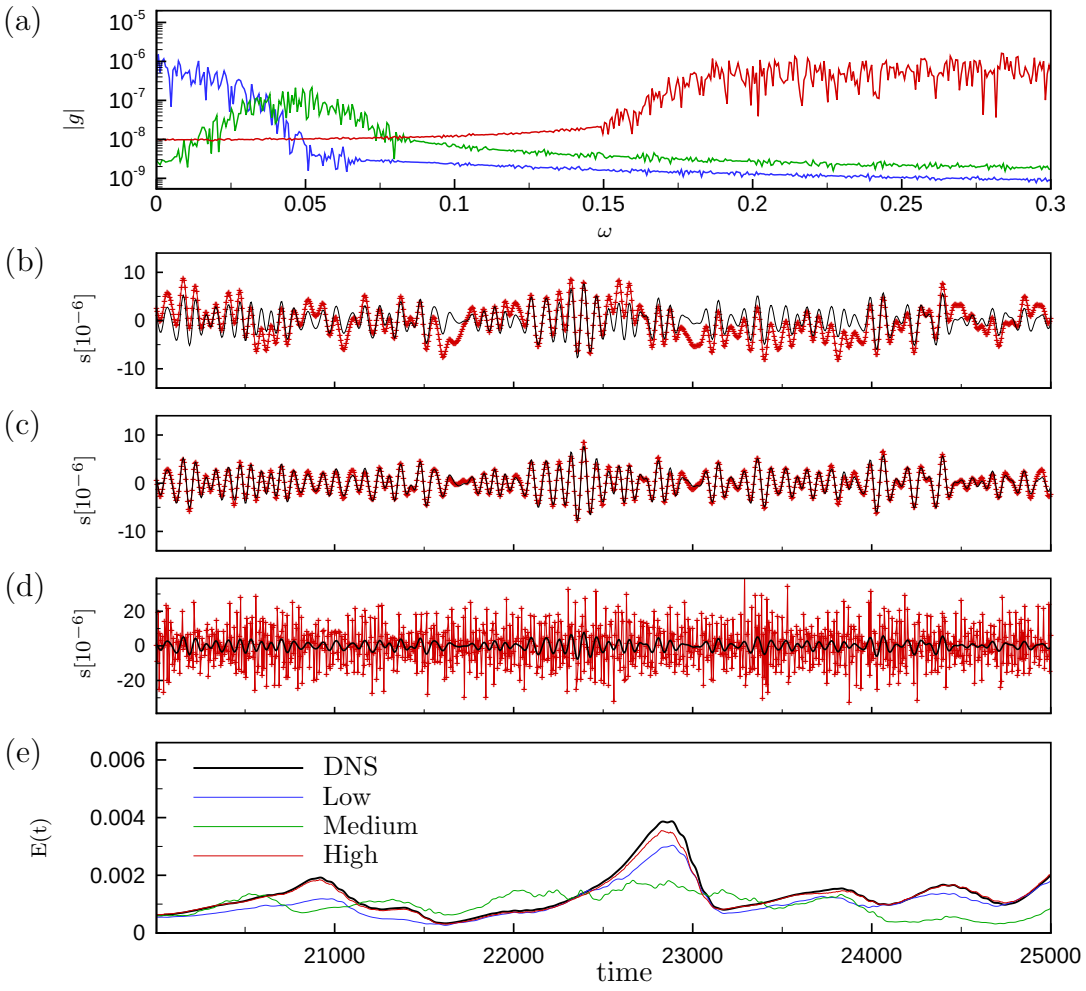

FIGURE 5.13: Influence of frequency-band-limited noise corrupting the estimation sensor s on the quality of the identification. Three configurations are investigated: (blue) low-, (green) medium- and (red) high-frequency noise. (a) Amplitude of the frequency spectrum of the noise. (b-d) Exact (black) and corrupted (red symbols) measurement s for the low-, medium- and high- frequency noise, respectively. (e) Estimation performance.

latter signal and a failure using the former ones. However, this is not the case. Figure 5.13(e) illustrates the performance obtained for each noise. Three models composed of 60 outputs were computed from a learning dataset of length $N_{snap} = 1000$ ($t = 5000$ time units). The models matches the validation dataset presented in figure 5.13(e) to 53.92%, -1.12% and 85.36% for the low-, medium- and high-frequency noises, respectively. Surprisingly, the models with the largest noise-amplitudes are successful in predicting the dynamics of the flow. In contrast, the model with the lowest level of noise (medium-frequency noise) fails.

To gain further insight, we computed the frequency response from the sensor s to the first 60 POD-coefficients of the full-order system (Figure 5.14(a)). This choice

was motivated by Equation (4.2). For an accurate estimation process, the transfer function considered here $s \rightarrow \mathbf{Y}$ is close to $s \rightarrow \mathbf{Y}_e$ which is equivalent to the transfer function from the noise to the estimated state $g \rightarrow \mathbf{Y}_e$. Consequently, for low-amplitude noise, the most harmful frequencies are the ones where $s \rightarrow \mathbf{Y}$ is large. This reasoning may appear overly simplistic since it does not take into account the loss in performance due to poor identification; nevertheless, it will prove to be a good estimate.

Four zones were defined in different frequency-ranges depending on the amplitude of the frequency response: zones 2 and 3 are located in the ranges with the largest gains, while zones 4 and 1 correspond to the lowest gains. The estimation sensor was again corrupted by successively adding noise coloured according to each zone. Different models composed of 60 outputs were identified from a learning dataset of length $N_{snap} = 2000$ using the noise-corrupted measurements. Figure 5.14(b) shows the performance versus the level of noise for the four zones as well as for white noise. For zones 1 and 4 the performance is almost independent of the level of noise: the quality of the identification is not significantly altered. On the other hand, zones 2 and 3 present significantly lower agreement compared to the white-noise-corrupted measurements. Therefore, we can conclude that noise acting on the range of frequencies where high gains of the system are located is most harmful for the estimator performance. The poorer performance of zones 3 and 4 compared to the white-noise scenario arises from the larger power spectral density levels in the sensitive frequency bands for these two zones. Moreover, we observe that zone 1 performs better than zone 4 which is again easily explained by considering the magnitude of the gains for each zone.

Figure 5.15 presents the transfer function from w and g to the error of the estimator $\mathbf{Z}$ for the three identified models depicted in Figure 5.13. As expected, the quality of the learning process $w \rightarrow \mathbf{Y}$ is greatly deteriorated for the medium-frequency case, but not for the low- and high-frequency models. The transfer function $g \rightarrow \mathbf{Y}$ is large in the range of frequencies leading to highest gains of the system in the three cases and, consequently, for the low- and high-frequency cases the decrease of performance due to this term is very low.

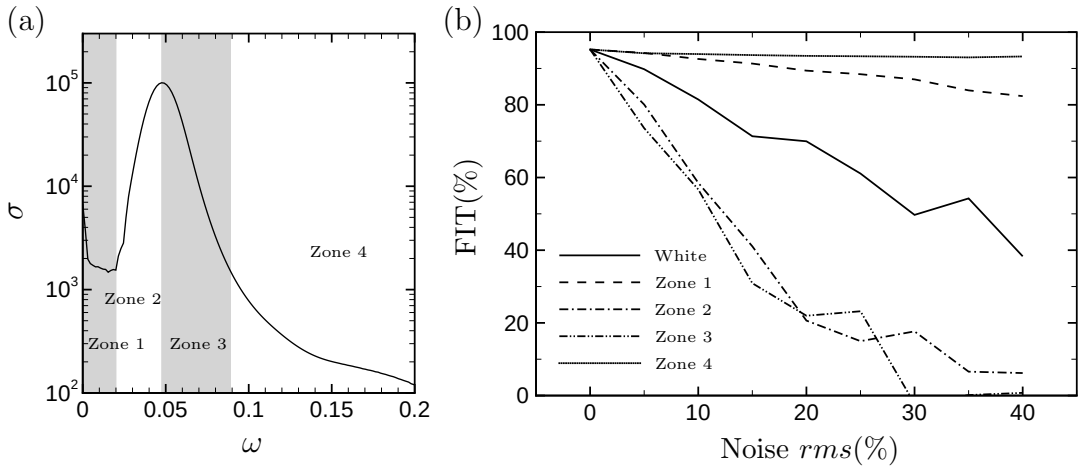

FIGURE 5.14: Influence of band-limited noise corrupting the estimation sensor s on the quality of the identification. (a) Singular value of the transfer function from s to the first 60 POD coefficients of the full-order system. Four zones are defined for different bands of frequencies corresponding to the noise corrupting the sensor.(b) Mean of the validation fit computed from samples of ten models obtained from different learning datasets for different types of noise.

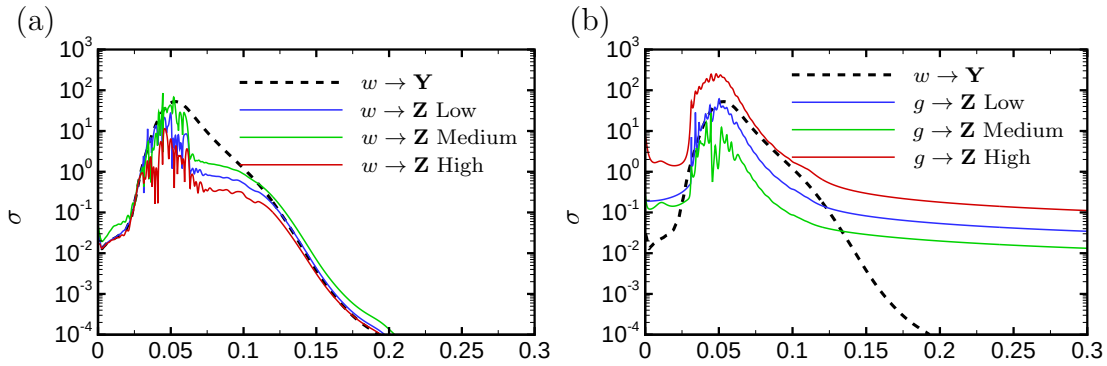

FIGURE 5.15: Frequency response of the estimation error for the identified models depicted in Figure 5.13: (a) $w \to \mathbf{Z}$, and (b) $g \to \mathbf{Z}$.

5.3 Summary of results and conclusions

The influence of the estimation sensor characteristics on the identification process has been investigated. Specifically, two situations of interest have been considered: (i) the position of the sensor with respect to the velocity window and (ii) the influence of adding corrupting noise on the quality of the estimation. Regarding the relative position of the estimation sensor and the upstream position of the velocity window, the optimal location for the sensor has been found to be the upstream edge of the velocity window. In fact, the identified dynamic observer fails to recover any information about the velocity field when situated upstream of the estimation sensor. However, this conclusion does not hold for a Kalman filter, which has

the capability of recovering some information (to a certain extent) upstream of the sensor. If the sensor is located upstream of the velocity measurement, the identification process fails due to the time-delay between the measurement s and the state of the system inside the velocity window. To overcome this difficulty, a time-delay can be explicitly introduced into the state-space model. An optimal delay has been determined to be equivalent to the time that a wave-packet takes to travel from the estimation sensor to the upstream edge of the velocity window.

The effect of white noise corrupting the measurement has also been studied. As expected, increasing the amplitude of the noise reduces the performance. For levels of noise higher than 100% the quality of the models is rather poor. However, such models still capture the general shape of the velocity field. We therefore conclude that matching based on the energy is too demanding a criterion to assess the performance of a model. In experimental implementations, thus, a less restrictive criterion should be selected. Moreover, the models obtained have been used to design a closed-loop control strategy. The compensated systems are stable for all considered levels of noise which is due to the properties of our feed-forward design. Nevertheless, the ability of the controller to effectively reduce the energy, even with the estimation measurements corrupted by noise with an amplitude of 100%, is remarkable.

We also examined the corruption of the estimation sensor by coloured noise. In this case, we have shown that the effect of the noise on the estimation performance greatly depends on the characteristic range of frequencies of the noise. In fact, we have shown that the most detrimental frequencies correspond to the ones with the highest system gains. In practical implementations, this information can be used to judiciously select the kind of sensor used for the identification.

Chapter 6

Concluding remarks

A data-based technique to obtain an estimator of noise-amplifier flows has been proposed. In Chapter 2, the technique was introduced and illustrated on a transitional two-dimensional boundary layer over a flat plate. In Chapter 3, the technique was used to approximate the global modes of a system and to estimate the frequency response between the estimation sensor and the full velocity field. In Chapter 4, the performance of the estimator was assessed with respect to the optimal estimator: the Kalman filter. Guidelines for a future implementation of the dynamic observer in experimental settings were given in Chapter 5.

6.1 Summary of work completed

In chapter 2, a technique to obtain a dynamic observer recovering full-state information from single wall-stress measurements has been introduced that relies on a POD basis (from measured snapshots) and system identification techniques. For noise-amplifier flows, it successfully reproduces the perturbation dynamics (velocity field) throughout the full sampling domain. The information produced by the dynamic observer can be used by itself, for flow diagnostics or used to design a closed-loop controller seeking to reduce the perturbation energy. The control capabilities have been illustrated using an LQR-control design and a reduction of nearly two orders of magnitude of the mean perturbation energy has been achieved.

The estimation performance of the proposed model has been compared with a classical data-based estimator: the linear stochastic estimator (LSE) (Adrian, 1979).

LSE proposes a static observer (the state of the system at a given time instant is correlated to the measurements of the sensors at the same time instant) which minimizes the mean-square estimation error of the system. For highly convective flows, the dynamic approach proposed here has been proven to be far superior to the static one (LSE) since the coherent structures are highly correlated in time, but not in space. As a consequence, LSE requires many closely-spaced sensors to overcome the lack of temporal information.

Within the limits of linear perturbation dynamics, the design process for the dynamic observer extracts the system matrix from a sequence of snapshots; this system matrix describes a globally stable flow configuration that is sustained by selectively amplified random perturbations from the noise environment. The proposed method thus successfully separates the intrinsic, stable perturbation dynamics from the external excitation noise. A wide variety of flow analysis is possible once the system matrix has been extracted. In Chapter 3, the global modes of the dynamic observer have been computed and qualitatively compared to results reported in the literature (Ehrenstein and Gallaire, 2005) for the full-order system. The most significant characteristics of the global modes are captured by the identified reduced-order model. A quantitative comparison, however, was not provided due to the difficulty to define representative boundary conditions. The dynamic observer has been proven to be an alternative to DMD for noise-amplifier flows, since the latter cannot separate the extrinsic from the intrinsic dynamics.

The performance of the estimator was assessed with respect to a reduced-order Kalman filter in Chapter 4. The Kalman filter is an optimal estimator in the sense of minimizing the mean-square estimation error and, consequently, is a good benchmark to compare with. The Kalman filter was computed using a classical approach which consists of first reducing the order of the system using a balanced projection and, then, solving a Riccati equation of the ROM to compute the elements of the Kalman filter. The Kalman filter is far superior to the data-based dynamic observer when noise-free measurements are employed. In contrast, when noise-corrupted sensors are considered, the performance of the identified model tends towards the optimal estimation. For noise-free estimation sensors, adding supplementary states to the identified model was proven to greatly improve its estimation performance; when dealing with noise-corrupted sensors the additional states are detrimental. The models obtained with either strategy have been compared in an optimal closed-loop application, showing that the control performances

are in close agreement.

Finally, in Chapter 5, guidelines to an experimental application of the dynamic observer have been given. Specifically, the relative position between the estimation sensor and the velocity window has been investigated and two configurations have been considered: (i) the sensor is inside, or (ii) upstream of the velocity window. An optimal placement for the sensor has been found to be at the upstream edge of the velocity window. The dynamic observer cannot provide any information from the region placed upstream of the estimation sensor. In contrast, the Kalman filter shows upstream *visibility*. In the second case, the identified model fails to recover any valid information due to an existing delay between the measurement of the estimation sensor and the state of the system. To overcome this difficulty, a time delay has been explicitly introduced in the identified model. This delay has been proven to be equivalent to move the sensor position, and an optimal delay has been found to be the time that it takes for a wave-packet to travel from the estimation sensor to the upstream edge of the velocity window.

The effect of adding corrupting noise to the estimation sensor has been assessed using white and coloured noises. The identified model has proven to be surprisingly resilient when the coloured noise is located in specific ranges of frequencies. More insight has been gained by computing the transfer function from the estimation sensor to the reduced-order state. The most pernicious frequencies for the estimator are in close agreement with the frequencies leading to highest gains of the system.

6.2 Main conclusions and limitations

A powerful technique to obtain reduced-order models from data that may be readily available in experiments has been proposed for noise amplifier flows. Within the limits of linear perturbation dynamics, our estimator performs better than existing data-based techniques for various applications. For instance, the estimation performance is superior to LSE. Furthermore, the model can separate the intrinsic from the extrinsic dynamics and provides meaningful global modes of the system, while the alternative technique (DMD) delivers modes containing the external noise.

A main limitation of the proposed approach resides in the assumption of linear dynamics. Although an extension of the approach dealing with non-linear identification is possible, its higher computational cost and difficult convergence characteristics make this extension a non-trivial undertaking.

6.3 Further work

An experimental implementation of the data-based dynamic observer is a key step to demonstrate the capabilities of the technique. This task has been partially done in the framework of a collaborative project with J. L. Aider and E. Varon. The obtained results are encouraging.

In the same way that the effect of noise corrupting the estimation error was assessed, the effect of noise corrupting the PIV window can be studied. In experimental boundary layers, we expect rather noisy PIV images due to the strong velocity gradient and the small amplitude of the perturbations. However, the projection of the velocity measurements onto the POD-modes should filter the error.

The large number of POD-modes required to compute suitable models suggests that alternative bases should be considered for noise-amplifier flows. A possibility is to use POD-modes weighted by a function of the x-coordinate which takes into account the spatial growth rate of the perturbations.

An extension of the technique to three-dimensional configurations is necessary. In that case, three-dimensional PIV (tomographic-PIV) measurements may be used or two-dimensional PIV planes containing the important dynamical features. An array of estimation sensors will also be necessary to determine the spanwise wave-number of the incoming perturbations.

Non-linearities must be included into the identified model in order to make the proposed framework a general and powerful technique. A plausible approach is the use of Hammerstein-Wiener models which connect linear systems with static non-linearities such as saturation and dead zone. POD-modes do not account for dissipation and, consequently, extra equations modelling it may be required to guarantee the stability of the models.

Appendix A

Subspace identification algorithms

Subspace identification algorithms consider the state-space formulation of a stochastic linear system. Such a system can be written in the following *process form*

$$x(n+1) = \mathcal{A}x(n) + \mathcal{B}u(n) + w(n) \tag{A.1a}$$

$$y(n) = \mathcal{C}x(n) + \mathcal{D}u(n) + v(n) \tag{A.1b}$$

where $y(n) \in \mathbb{R}^{n_y}$, $x(n) \in \mathbb{R}^n$, $u(n) \in \mathbb{R}^{n_u}$, $w(n) \in \mathbb{R}^n$, $v(n) \in \mathbb{R}^{n_y}$ are the system output, state, input, state noise, and output measurement noise, respectively. The matrices $\mathcal{A}$, $\mathcal{B}$, $\mathcal{C}$ and $\mathcal{D}$ are system matrices of appropiate dimensions. The noise covariances of the system are defined as

$$\mathcal{E}\left\{ \begin{pmatrix} w_j \\ v_j \end{pmatrix} \begin{pmatrix} w_i \\ v_i \end{pmatrix}^T \right\} = \begin{pmatrix} \mathcal{Q} & \mathcal{S} \\ \mathcal{S}^T & \mathcal{R} \end{pmatrix} \delta_{ij} \tag{A.2}$$

where $\mathcal{E}\{x\}$ stands for the expected-value operator.

The general problem of subspace identification consists of obtaining the system matrices $\mathcal{A}$, $\mathcal{B}$, $\mathcal{C}$ and $\mathcal{D}$, as well as the covariance matrices $\mathcal{Q}$, $\mathcal{S}$, and $\mathcal{R}$, from observing a set of input-output measurements.

A.1 Reformulation of the state-space system

The state-space system (A.1) can be rearranged into two equivalent formulations that emphasize either prediction or estimation (Qin, 2006). Considering either

formulation, the one-step linear equations can be written as a multi-step matrix-based expression which will form the foundation of subspace system-identification techniques.

Assuming that the system is observable, a Kalman filter can be designed to estimate the state variable. We have

$$\widehat{x}(n+1) = \mathcal{A}\widehat{x}(n) + \mathcal{B}u(n) + \mathcal{K}\left[y(n) - \mathcal{C}\widehat{x}(n) - \mathcal{D}u(n)\right] \tag{A.3}$$

which (omitting the $\widehat{\ }$) leads to the following *innovation form*

$$x(n+1) = \mathcal{A}x(n) + \mathcal{B}u(n) + \mathcal{L}e(n) \tag{A.4a}$$

$$y(n) = \mathcal{C}x(n) + \mathcal{D}u(n) + e(n) \tag{A.4b}$$

where $\mathcal{L}$ is the Kalman gain (which can be obtained from a Riccati equation) and $e(n) = y(n) - \mathcal{C}\widehat{x}(n) - \mathcal{D}u(n)$ is the measurement error.

A third equivalent representation, the *predictor form*, can be written as follows

$$x(n+1) = \mathcal{A}_e x(n) + \mathcal{B}_e \mathbf{z}(n) \tag{A.5a}$$

$$y(n) = \mathcal{C}x(n) + \mathcal{D}u(n) + e(k) \tag{A.5b}$$

where $\mathbf{z}(n) = \left[u^T(n), y^T(n)\right]^T$, $\mathcal{A}_e = \mathcal{A} - \mathcal{L}\mathcal{C}$, and $\mathcal{B}_e = [\mathcal{B} - \mathcal{L}\mathcal{D}, \mathcal{L}]$. It should be stressed again that the three model forms can represent the input and ouput data $(u(n), y(n))$ exactly. We thus have the choice of using any of these models according to convenience.

As a next step, the above one-step vector-based linear difference equations are recast into multi-step matrix-based expressions. We first define an extended state sequence $\mathbf{X}(n) = \Big(x(n),\ \ x(n+1),\ \ \ldots,\ \ x(n+N-1)\Big)$ which contains N columns describing the state at N consecutive time steps. By iterating p times the predictor form (A.5) it is straightforward to derive the following extended equation,

$$\mathbf{X}(n) = \mathcal{L}_p \mathbf{Z}_p + \mathcal{A}_e^p \mathbf{X}(n-p) \tag{A.6}$$

where

$$\mathcal{L}_p = \left(\mathcal{B}_e, \quad \mathcal{A}_e\mathcal{B}_e, \quad \ldots, \quad \mathcal{A}_e^{p-1}\mathcal{B}_e\right), \tag{A.7a}$$

$$\mathbf{Z}_p = \begin{pmatrix} \mathbf{z}(n-1) & \mathbf{z}(n) & \ldots & \mathbf{z}(n+N-2) \\ \mathbf{z}(n-2) & \mathbf{z}(n-1) & \ldots & \mathbf{z}(n+N-3) \\ \vdots & \vdots & \ddots & \vdots \\ \mathbf{z}(n-p) & \mathbf{z}(n-p+1) & \ldots & \mathbf{z}(n-p+N-1) \end{pmatrix}. \tag{A.7b}$$

Under the assumption that all eigenvalues of the estimator matrix $\mathcal{A}_e$ fall strictly inside the unit circle and in the limit $p \to \infty$, the term $\mathcal{A}_e^p$ can be neglected. This result can be proven valid even for finite p (Van Overschee and De Moor (1994), Van Overschee and De Moor (1996)). Equation (A.6) can then be simplified to

$$\mathbf{X}(n) = \mathcal{L}_p\mathbf{Z}_p. \tag{A.8}$$

In addition, if a similar recursive iteration technique is applied to the innovation form (A.4) we obtain

$$\mathbf{Y}_f = \mathcal{O}_f\mathbf{X}(n) + \mathcal{H}_f\mathbf{U}_f + \mathcal{G}_f\mathbf{E}_f \tag{A.9}$$

where the subscript $_f$ denotes the future horizon. Next, the input, output and innovation data are arranged into Hankel matrices, denoted respectively by $\mathbf{U}_f$, $\mathbf{Y}_f$ and $\mathbf{E}_f$. The structure of these matrices is as follows

$$\mathbf{U}_f = \begin{pmatrix} u(n) & u(n+1) & \ldots & u(n+N-1) \\ u(n+1) & u(n+2) & \ldots & u(n+N) \\ \vdots & \vdots & \ddots & \vdots \\ u(n+f-1) & u(n+f) & \ldots & u(n+f+N-2) \end{pmatrix}, \tag{A.10}$$

and similar for $\mathbf{Y}_f$ and $\mathbf{E}_f$.

Furthermore, $\mathcal{O}_f$ is the extended observability matrix, and $\mathcal{H}_f$, $\mathcal{G}_f$ are Toeplitz matrices of the form

$$\mathcal{O}_f = \begin{pmatrix} \mathcal{C} \\ \mathcal{C}\mathcal{A} \\ \vdots \\ \mathcal{C}\mathcal{A}^{f-1} \end{pmatrix}, \tag{A.11a}$$

$$\mathcal{H}_f = \begin{pmatrix} \mathcal{D} & 0 & \dots & 0 \\ \mathcal{C}\mathcal{B} & \mathcal{D} & \dots & 0 \\ \vdots & \vdots & \ddots & \vdots \\ \mathcal{C}\mathcal{A}^{f-2}\mathcal{B} & \mathcal{C}\mathcal{A}^{f-3}\mathcal{B} & \dots & \mathcal{D} \end{pmatrix}, \tag{A.11b}$$

$$\mathcal{G}_f = \begin{pmatrix} \mathcal{I} & 0 & \dots & 0 \\ \mathcal{C}\mathcal{K} & \mathcal{I} & \dots & 0 \\ \vdots & \vdots & \ddots & \vdots \\ \mathcal{C}\mathcal{A}^{f-2}\mathcal{K} & \mathcal{C}\mathcal{A}^{f-3}\mathcal{K} & \dots & \mathcal{I} \end{pmatrix}. \tag{A.11c}$$

Combining (A.8) and (A.9) we obtain

$$\mathbf{Y}_f = \mathcal{H}_{fp}\mathbf{Z}_p + \mathcal{H}_f\mathbf{U}_f + \mathcal{G}_f\mathbf{E}_f \tag{A.12}$$

where $\mathcal{H}_{fp} = \mathcal{O}_f\mathcal{L}_p$ is the product of the process observability matrix and the predictor controllability matrix. Equation (A.12) plays an essential role in subspace identification algorithms.

A.2 Extraction of the observability matrix $\mathcal{O}_f$

The goal of the subsequent steps is to recover the matrix $\mathcal{H}_{fp}\mathbf{Z}_p$, and then $\mathcal{O}_f$ from it. First, $\mathbf{U}_f$ is eliminated from equation (A.12) by post-multiplying by the projection onto its orthogonal complement $\mathcal{P}^{\perp}_{U_f} = \mathcal{I} - \mathbf{U}_f^T(\mathbf{U}_f\mathbf{U}_f^T)^{-1}\mathbf{U}_f$. In addition, if we assume that the innovation sequence $e(n)$ is composed of a stationary, white noise completely uncorrelated with the input $u(n)$ we have $\mathbf{E}_f\mathcal{P}^{\perp}_{U_f} = \mathbf{E}_f$ which yields

$$\mathbf{Y}_f \mathcal{P}_{U_f}^{\perp} = \mathcal{H}_{fp} \mathbf{Z}_p \mathcal{P}_{U_f}^{\perp} + \mathcal{G}_f \mathbf{E}_f. \tag{A.13}$$

It is also known from Kalman filter theory that $\mathbf{E}_f$ is uncorrelated to $\mathbf{Z}_p$. Consequently, the noise term $\mathbf{E}_f$ can be removed by multiplying (from the right) equation (A.13) by $\mathbf{Z}_p^T$ which yields

$$\mathbf{Y}_f \mathcal{P}_{U_f}^{\perp} \mathbf{Z}_p^T = \mathcal{H}_{fp} \mathbf{Z}_p \mathcal{P}_{U_f}^{\perp} \mathbf{Z}_p^T, \tag{A.14}$$

and

$$\mathcal{H}_{fp} \mathbf{Z}_p = \mathbf{Y}_f \mathcal{P}_{U_f}^{\perp} \mathbf{Z}_p^T (\mathcal{P}_{U_f}^{\perp} \mathbf{Z}_p^T)^{-1}. \tag{A.15}$$

Finally, from equation A.8 we obtain that $\mathcal{H}_{fp} \mathbf{Z}_p = \mathcal{O}_f \mathbf{X}(n)$. Assuming that the input $u(n)$ is sufficiently rich in temporal behavior to excite all the observable dynamics of the system, matrix $\mathbf{X}(n)$ is ensured to be full row-ranked. In addition, $\mathcal{O}_f$ has full column-rank under the assumption of full observability. These properties suggest applying a singular value decomposition (SVD): (i) to determine the order of the identified system as the rank of $\mathcal{O}_f \mathbf{X}(n)$ and (ii) to isolate $\mathcal{O}_f$. Mathematically, this amounts to

$$\mathcal{H}_{fp} \mathbf{Z}_p = \begin{pmatrix} \mathcal{U}_1 & \mathcal{U}_2 \end{pmatrix} \begin{pmatrix} \mathcal{S}_1 & 0 \\ 0 & \mathcal{S}_2 \end{pmatrix} \begin{pmatrix} \mathcal{V}_1^T \\ \mathcal{V}_2^T \end{pmatrix}, \tag{A.16}$$

where the diagonal matrix $\mathcal{S}$ has been partitioned so that $\mathcal{S}_2$ is negligible compared to $\mathcal{S}_1$. The size of $\mathcal{S}_1$ then represents the order of the identified system. Moreover, the extended observability matrix $\mathcal{O}_f$ can be extracted according to

$$\mathcal{O}_f = \mathcal{U}_1 \mathcal{S}_1^{1/2}. \tag{A.17}$$

A.3 Extraction of the system matrices

Based on $\mathcal{O}_f$, two different approaches may be adopted to extract the system matrices. The first one, denoted as *estimation focus*, extracts only the system matrices $\mathcal{A}$, $\mathcal{B}$, $\mathcal{C}$ and $\mathcal{D}$ from the data. On the other hand, if the noise covariances are needed, a more complex algorithm, a *simulation focus technique*, is called for. In this article, we will briefly introduce the first approach, while a detailed

description of the second one can be found in Van Overschee and De Moor (1994), Van Overschee and De Moor (1996) or Juillet et al. (2013).

The first step consists in extracting the matrices $\mathcal{A}$ and $\mathcal{C}$ from $\mathcal{O}_f$. This can be accomplished rather easily by computing the matrix $\mathcal{O}_{f-1}$ as previously done with $\mathcal{O}_f$ and by recalling that, by definition, both matrices are related by the equation

$$\begin{pmatrix} \mathcal{I} & 0 \\ 0 & \mathcal{O}_{f-1} \end{pmatrix} \begin{pmatrix} \mathcal{C} \\ \mathcal{A} \end{pmatrix} = \mathcal{O}_f, \tag{A.18}$$

which can be solved by least-squares techniques. To determine the remaining matrices $\mathcal{B}$ and $\mathcal{D}$, one uses the fact that the problem is linear in these matrices; a simple least-squares matching to the output data may be used to find the remaining matrices (Van Overschee and De Moor (1996)).

Appendix B

Model order reduction using the Eigensystem Realization Algorithm (ERA)

In this appendix, we introduce a technique to reduce the degrees of freedom of the full-order system: the eigensystem realisation algorithm (ERA).

The full-order linearised Navier-Stokes equations are expressed as a linear-time invariant system

$$\mathbf{v}(n+1) = \mathscr{A}\mathbf{v}(n) + \mathscr{B}_w w(n) + \mathscr{B}_u u(n), \tag{B.1a}$$

$$\mathbf{Y}_f(n) = \mathscr{C}_y \mathbf{v}(n), \quad s_f(n) = \mathscr{C}_s \mathbf{v}(n), \tag{B.1b}$$

where $\mathscr{A}$, $\mathscr{B}_w$, $\mathscr{B}_u$, $\mathscr{C}_y$ and $\mathscr{C}_s$ are linear operators, $\mathbf{v}(n)$ is the full-order velocity field, $w(n)$ and $u(n)$ are the inputs corresponding to the external driving term and the controller, respectively; and $\mathbf{Y}_f(n)$ and $s_f(n)$ are the outputs corresponding to a vector of POD-coefficients and a wall-stress sensor measurement, respectively.

The ERA was proposed in (Juang and Pappa, 1985) as a system identification and model reduction technique for linear systems. The algorithm follows three main steps:

The first step consists in running impulse-responses of the system (B.1) for $2NP+2$ time steps. Then, the snapshots of the outputs are collected in the following

pattern:

$$\left(\mathscr{C}\mathscr{B},\ \mathscr{C}\mathscr{A}\mathscr{B},\ \mathscr{C}\mathscr{A}^{P}\mathscr{B},\ \mathscr{C}\mathscr{A}^{P+1}\mathscr{B},\ldots,\ \mathscr{C}\mathscr{A}^{2NP}\mathscr{B},\ \mathscr{C}\mathscr{A}^{2NP+1}\mathscr{B}\right)$$

$$\mathscr{B}\equiv\left(\mathscr{B}_w\ \mathscr{B}_u\right)\qquad \mathscr{C}\equiv\begin{pmatrix}\mathscr{C}_y\\ \mathscr{C}_s\end{pmatrix}$$

The terms $\mathscr{C}\mathscr{A}^{k}\mathscr{B}$ are called *Markov parameters*. The variable P is the number of time steps between each pair of Markov parameters, and N is the number of pairs. The Markov parameters are subsequently ranged in two generalized Hankel matrices of the form

$$\mathsf{H}=\begin{pmatrix}\mathscr{C}\mathscr{B} & \mathscr{C}\mathscr{A}\mathscr{B} & \cdots & \mathscr{C}\mathscr{A}^{NP}\mathscr{B}\\ \mathscr{C}\mathscr{A}^{P}\mathscr{B} & \mathscr{C}\mathscr{A}^{2P}\mathscr{B} & \cdots & \mathscr{C}\mathscr{A}^{(N+1)P}\mathscr{B}\\ \vdots & \vdots & \ddots & \vdots\\ \mathscr{C}\mathscr{A}^{NP}\mathscr{B} & \mathscr{C}\mathscr{A}^{(N+1)P}\mathscr{B} & \cdots & \mathscr{C}\mathscr{A}^{2NP}\mathscr{B}\end{pmatrix}, \tag{B.2}$$

and

$$\mathsf{H}'=\begin{pmatrix}\mathscr{C}\mathscr{A}\mathscr{B} & \mathscr{C}\mathscr{A}^{P+1}\mathscr{B} & \cdots & \mathscr{C}\mathscr{A}^{NP+1}\mathscr{B}\\ \mathscr{C}\mathscr{A}^{P+1}\mathscr{B} & \mathscr{C}\mathscr{A}^{2P+1}\mathscr{B} & \cdots & \mathscr{C}\mathscr{A}^{(N+1)P+1}\mathscr{B}\\ \vdots & \vdots & \ddots & \vdots\\ \mathscr{C}\mathscr{A}^{NP+1}\mathscr{B} & \mathscr{C}\mathscr{A}^{(N+1)P+1}\mathscr{B} & \cdots & \mathscr{C}\mathscr{A}^{2NP+1}\mathscr{B}\end{pmatrix}. \tag{B.3}$$

The second step is to compute the singular value decomposition (SVD) of H to obtain $\mathsf{H}=\mathsf{U}\Sigma\mathsf{V}^{H}$, where U and V are unitary and Σ is diagonal. Then, we select the order of the reduced-order model, N_{x}, and truncate the matrices, keeping the first N_{x} columns of U and V to obtain U_r and V_r , and the first N_{x} rows and columns of Σ to obtain Σ_r. Then, we find the reduced-order model matrices,

$$\begin{aligned}\mathsf{A}_w &= \Sigma_r^{-1/2}\ \mathsf{U}_r^{H}\ \mathsf{H}'\ \mathsf{V}\ \Sigma_r^{-1/2};\\ \mathsf{B} &= \text{the first [number of inputs] columns of } \Sigma_r^{1/2}\mathsf{V}^{H};\\ \mathsf{C} &= \text{ the first [number of outputs] rows of } \mathsf{U}_r\Sigma_N^{1/2}\end{aligned} \tag{B.4}$$

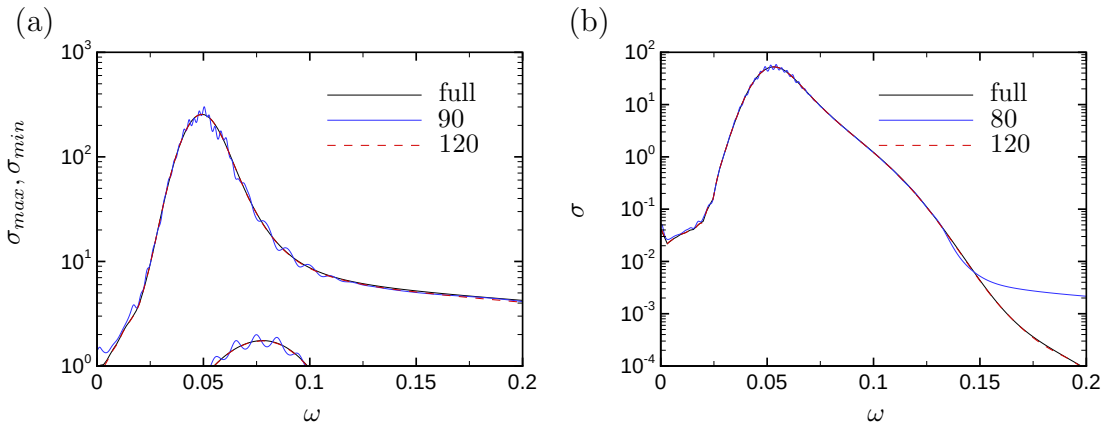

FIGURE B.1: Comparison of the input-output behaviour ($(w, u) \rightarrow (s, \mathbf{Y})$) between the full-state system and ROMs based on ERA. (a) Singular values of the transfer functions from u and w to 70 POD-coefficients for (black solid) the full-state system and two ROMs of size (blue solid) 90 and (red dashed) 120, respectively. (b) Singular value of the transfer function from w to 60 POD-coefficients for the full-state system (black solid) and two ROMs of size 80 (blue solid) and 120 (red dashed). The full-state system comprises 392000 degrees of freedom.

The reduced system is

$$\mathbf{X}(n+1) = \mathsf{A}_w \mathbf{X}(n) + \mathsf{B}\mathbf{U}(n), \tag{B.5a}$$

$$\begin{pmatrix} \mathbf{Y}(n) \\ s(n) \end{pmatrix} = \begin{pmatrix} \mathsf{C}_\mathrm{y} \\ \mathsf{C}_\mathrm{s} \end{pmatrix} \mathbf{X}(n) = \mathsf{C}\mathbf{X}(n), \tag{B.5b}$$

where $\mathbf{X} \in \mathbb{R}^{\mathbf{N}_\mathrm{x}}$ is the reduced state, and A_w, B and C are the reduced-order matrices. The vector $\mathbf{U}$ contains the two inputs of the system $\mathbf{U}(n) = \begin{pmatrix} w(n) & u(n) \end{pmatrix}^T$; the matrix B can be decomposed into $\mathsf{B} = \begin{pmatrix} \mathbf{B}_w & \mathbf{B}_u \end{pmatrix}$.

This technique has been applied to the boundary layer considered in this thesis. Figure B.1 presents the frequency response of the ROM compared to the full-order system for two cases: (a) the transfer function from (w, u) to 70 POD-coefficients $\mathbf{Y}$, and (b) the transfer function from w to 60 POD-coefficients $\mathbf{Y}$. The results show that an increasing number of states improves the quality of the ROM.

The performance of the ROMs is summarized in Table B.1. To compute the truncation error $\mathbf{Z}_f = (\mathbf{Y}_f - \mathbf{Y})$, we applied an impulse to w and u individually in the full- and reduced-order systems. Subsequently, we computed the difference between the time-evolution of the outputs for the two impulses and we Fourier-transformed these two errors to obtain the frequency response from each input.

Transfer function	N_{x}	$\|\mathbf{Z}_f\|_\infty$	$\|\mathbf{Z}_f\|_\infty/\|\mathbf{Y}_f\|_\infty$
$w \to \mathbf{Z}_f$ $(k = 60)$			
	80	3.59	0.068
	100	0.4	0.007
	120	0.07	0.001
$(w, u) \to \mathbf{Z}_f$ $(k = 70)$			
	90	50.94	0.2
	100	9.71	0.038
	120	0.86	0.003
	140	0.45	0.002

TABLE B.1: Performance of the reduced-order model versus the number of elements of the reduced-state N_x. $H\infty-$norm of the transfer function from w and (w, u) to the truncation error of the ROM $\mathbf{Z}_f = (\mathbf{Y}_f - \mathbf{Y})$.

The error relative to a given input is defined as the $H_\infty-$norm of the error divided by the $H_\infty-$norm of the full-order system. The size of the ROMs that are used in Chapter 4 was selected to be $N_x = 120$ for either the estimation $w \to \mathbf{Y}$ and $(w, u) \to \mathbf{Y}$ control cases, and yield relative errors of 0.1% and 0.3%, respectively.

Bibliography

Adrian, R. (1979). Conditional eddies in isotropic turbulence. *Phys. Fluids*, 22:2065–2070.

Ahuja, S. and Rowley, C. (2010). Feedback control of unstable steady states of flow past a flat plate using reduced-order estimators. *J. Fluid Mech.*, 645:447–478.

Åkervik, E., Hœpffner, J., Ehrenstein, U., and Henningson, D. S. (2007). Optimal growth, model reduction and control in a separated boundary-layer flow using global eigenmodes. *Journal of Fluid Mechanics*, 579(1):305–314.

Alizard, F. and Robinet, J.-C. (2007). Spatially convective global modes in a boundary layer. *Physics of Fluids*, 19(11):114105.

Antoulas, A. (2005). *Approximation of large-scale dynamical systems*. SIAM Publishing.

Aubry, N., Holmes, P., Lumley, J. L., and Stone, E. (1988). The dynamics of coherent structures in the wall region of a turbulent boundary layer. *Journal of Fluid Mechanics*, 192:115–173.

Bagheri, S. (2013). Koopman-mode decomposition of the cylinder wake. *Journal of Fluid Mechanics*, 726:596–623.

Bagheri, S., Brandt, L., and Henningson, D. (2009). Input–output analysis, model reduction and control of the flat-plate boundary layer. *J. Fluid Mech.*, 620(1):263–298.

Barbagallo, A., Sipp, D., and Schmid, P. (2009). Closed-loop control of an open cavity flow using reduced-order models. *J. Fluid Mech.*, 641(1):1–50.

Barbagallo, A., Sipp, D., and Schmid, P. J. (2011). Input–output measures for model reduction and closed-loop control: application to global modes. *Journal of Fluid Mechanics*, 685:23–53.

Bearman, P. W. and Harvey, J. K. (1993). Control of circular cylinder flow by the use of dimples. *AIAA journal*, 31(10):1753–1756.

Belson, B. A., Semeraro, O., Rowley, C. W., and Henningson, D. S. (2013). Feedback control of instabilities in the two-dimensional blasius boundary layer: The role of sensors and actuators. *Physics of Fluids (1994-present)*, 25(5):054106.

Bergmann, M., Bruneau, C.-H., and Iollo, A. (2009). Enablers for robust pod models. *J. Comp. Phys.*, 228(2):516–538.

Bergmann, M. and Cordier, L. (2008). Optimal control of the cylinder wake in the laminar regime by trust-region methods and pod reduced-order models. *Journal of Computational Physics*, 227(16):7813–7840.

Bergmann, M., Cordier, L., and Brancher, J. P. (2005). Optimal rotary control of the cylinder wake using proper orthogonal decomposition reduced-order model. *Physics of Fluids (1994-present)*, 17(9):097101.

Bewley, T. R. and Liu, S. (1998). Optimal and robust control and estimation of linear paths to transition. *Journal of Fluid Mechanics*, 365:305–349.

Boiko, A. V., Dovgal, A. V., and Hein, S. (2008). Control of a laminar separating boundary layer by induced stationary perturbations. *European Journal of Mechanics-B/Fluids*, 27(4):466–476.

Bonnet, J.-P., Cole, D., Delville, J., Glauser, M., and Ukeiley, L. (1994). Stochastic estimation and proper orthogonal decomposition: complementary techniques for identifying structure. *Exp. Fluids*, 17:307–314.

Bottaro, A., Corbett, P., and Luchini, P. (2003). The effect of base flow variation on flow stability. *Journal of Fluid Mechanics*, 476:293–302.

Brandt, L., Sipp, D., Pralits, J., and Marquet, O. (2011). Effect of base-flow variation in noise amplifiers: the flat-plate boundary layer. *J. Fluid Mech.*, 687:503–528.

Burl, J. B. (1999). *Linear Optimal Control*. Addison-Wesley Longman Publishing Co., Inc.

Butler, K. M. and Farrell, B. F. (1992). Three-dimensional optimal perturbations in viscous shear flow. *Physics of Fluids A: Fluid Dynamics (1989-1993)*, 4(8):1637–1650.

Cattafesta III, L. N. and Sheplak, M. (2011). Actuators for active flow control. *Annual Review of Fluid Mechanics*, 43:247–272.

Chaturantabut, S. and Sorensen, D. C. (2010). Nonlinear model reduction via discrete empirical interpolation. *SIAM Journal on Scientific Computing*, 32(5):2737–2764.

Chevalier, M., Hœpffner, J., Akervik, E., and Henningson, D. S. (2007). Linear feedback control and estimation applied to instabilities in spatially developing boundary layers. *Journal of Fluid Mechanics*, 588:163.

Choi, H., Jeon, W. P., and Kim, J. (2008). Control of flow over a bluff body. *Annu. Rev. Fluid Mech.*, 40:113–139.

Chomaz, J. M. (2005). Global instabilities in spatially developing flows: non-normality and nonlinearity. *Annu. Rev. Fluid Mech.*, 37:357–392.

Cortelezzi, L., Speyer, J. L., Lee, K. H., and Kim, J. (1998). Robust reduced-order control of turbulent channel flows via distributed sensors and actuators. In *Decision and Control, 1998. Proceedings of the 37th IEEE Conference on*, volume 2, pages 1906–1911. IEEE.

Dahan, J. A., Morgans, A. S., and Lardeau, S. (2012). Feedback control for form-drag reduction on a bluff body with a blunt trailing edge. *Journal of Fluid Mechanics*, 704:360–387.

Dergham, G., Sipp, D., and Robinet, J. C. (2011a). Accurate low dimensional models for deterministic fluid systems driven by uncertain forcing. *Physics of Fluids (1994-present)*, 23(9):094101.

Dergham, G., Sipp, D., and Robinet, J. C. (2013). Stochastic dynamics and model reduction of amplifier flows: the backward facing step flow. *J. Fluid Mech.*, 719:406–430.

Dergham, G., Sipp, D., Robinet, J.-C., and Barbagallo, A. (2011b). Model reduction for fluids using frequential snapshots. *Physics of Fluids*, 23:064101.

Dowling, A. P. and Morgans, A. S. (2005). Feedback control of combustion oscillations. *Annu. Rev. Fluid Mech.*, 37:151–182.

Ehrenstein, U. and Gallaire, F. (2005). On two-dimensional temporal modes in spatially evolving open flows: the flat-plate boundary layer. *Journal of Fluid Mechanics*, 536:209–218.

Ehrenstein, U., Passaggia, P. Y., and Gallaire, F. (2011). Control of a separated boundary layer: reduced-order modeling using global modes revisited. *Theoretical and Computational Fluid Dynamics*, 25(1-4):195–207.

Fosas de Pando, M., Schmid, P. J., and Sipp, D. (2013). Nonlinear model-order reduction for oscillator flows using pod-deim. In *APS Meeting Abstracts*, volume 1, page 25006.

Galletti, B., Bruneau, C. H., Zannetti, L., and Iollo, A. (2004). Low-order modelling of laminar flow regimes past a confined square cylinder. *Journal of Fluid Mechanics*, 503:161–170.

Gaster, M. (1974). On the effects of boundary-layer growth on flow stability. *Journal of Fluid Mechanics*, 66(03):465–480.

Gautier, N. and Aider, J. L. (2014). Feed-forward control of a perturbed backward-facing step flow. *Journal of Fluid Mechanics*, 759:181–196.

Gautier, N., Aider, J. L., Duriez, T., Noack, B. R., Segond, M., and Abel, M. (2015). Closed-loop separation control using machine learning. *Journal of Fluid Mechanics*, 770:442–457.

Giannetti, F. and Luchini, P. (2007). Structural sensitivity of the first instability of the cylinder wake. *Journal of Fluid Mechanics*, 581:167–197.

Godard, G. and Stanislas, M. (2006). Control of a decelerating boundary layer. part 1: Optimization of passive vortex generators. *Aerospace Science and Technology*, 10(3):181–191.

Guezennec, Y. (1989). Stochastic estimation of coherent structures in turbulent boundary layers. *Phys. Fluids*, 1:1054–1060.

Guzmán Iñigo, J., Sipp, D., and Schmid, P. J. (2014). A dynamic observer to capture and control perturbation energy in noise amplifiers. *J. Fluid Mech.*, 758:728–753.

He, J. W., Chevalier, M., Glowinski, R., Metcalfe, R., Nordlander, A., and Periaux, J. (2000). Drag reduction by active control for flow past cylinders. In *Computational Mathematics Driven by Industrial Problems*, pages 287–363. Springer.

Hervé, A., Sipp, D., Schmid, P., and Samuelides, M. (2012). A physics-based approach to flow control using system identification. *J. Fluid Mech.*, 702:26–58.

Hogberg, M., Bewley, T. R., and Henningson, D. S. (2003). Linear feedback control and estimation of transition in plane channel flow. *Journal of Fluid Mechanics*, 481:149–175.

Högberg, M., Bewley, T. R., and Henningson, D. S. (2003). Relaminarization of reτ= 100 turbulence using gain scheduling and linear state-feedback control. *Physics of Fluids (1994-present)*, 15(11):3572–3575.

Högberg, M. and Henningson, D. S. (2002). Linear optimal control applied to instabilities in spatially developing boundary layers. *Journal of Fluid Mechanics*, 470:151–179.

Huang, S.-C. and Kim, J. (2008). Control and system identification of a separated flow. *Physics of Fluids (1994-present)*, 20(10):101509.

Hudy, L., Naguib, A., and Humphreys, W. (2007). Stochastic estimation of a separated flow field using wall-pressure array measurements. *Phys. Fluids*, 19:024103.

Huerre, P. and Rossi, M. (1998). Hydrodynamic instabilities in open flows. *Collection alea saclay monographs and texts in statistical physics*, pages 81–294.

Ilak, M. and Rowley, C. W. (2008). Modeling of transitional channel flow using balanced proper orthogonal decomposition. *Physics of Fluids (1994-present)*, 20(3):034103.

Illingworth, S. J., Morgans, A. S., and Rowley, C. W. (2011). Feedback control of flow resonances using balanced reduced-order models. *Journal of Sound and Vibration*, 330(8):1567–1581.

Illingworth, S. J., Morgans, A. S., and Rowley, C. W. (2012). Feedback control of cavity flow oscillations using simple linear models. *Journal of Fluid Mechanics*, 709:223–248.

Illy, H., Geffroy, P., and Jacquin, L. (2004). Control of flow oscillations over a cavity by means of a spanwise cylinder. In *XXI International Congress of Theoretical and Applied Mechanics Warsaw, Poland, August*, volume 1521.

Jackson, C. P. (1987). A finite-element study of the onset of vortex shedding in flow past variously shaped bodies. *Journal of fluid Mechanics*, 182:23–45.

Jacquin, L., Molton, P., Deck, S., Maury, B., and Soulevant, D. (2009). Experimental study of shock oscillation over a transonic supercritical profile. *AIAA journal*, 47(9):1985–1994.

Joshi, S. S., Speyer, J. L., and Kim, J. (1997). A systems theory approach to the feedback stabilization of infinitesimal and finite-amplitude disturbances in plane poiseuille flow. *Journal of Fluid Mechanics*, 332:157–184.

Juang, J. N. and Pappa, R. S. (1985). An eigensystem realization algorithm for modal parameter identification and model reduction. *Journal of guidance, control, and dynamics*, 8(5):620–627.

Juillet, F., McKeon, B., and Schmid, P. J. (2014). Experimental control of natural perturbations in channel flow. *Journal of Fluid Mechanics*, 752:296–309.

Juillet, F., Schmid, P., and Huerre, P. (2013). Control of amplifier flows using subspace identification techniques. *J. Fluid Mech.*, 725:522–565.

Kim, J. and Bewley, T. R. (2007). A linear systems approach to flow control. *Annu. Rev. Fluid Mech.*, 39:383–417.

Lacy, S. L., Venugopal, R., and Bernstein, D. S. (1998). Armarkov adaptive control of self-excited oscillations of a ducted flame. In *Decision and Control, 1998. Proceedings of the 37th IEEE Conference on*, volume 4, pages 4527–4528. IEEE.

Lee, K. H., Cortelezzi, L., Kim, J., and Speyer, J. (2001). Application of reduced-order controller to turbulent flows for drag reduction. *Physics of Fluids (1994-present)*, 13(5):1321–1330.

Lewis, J., Lakshmivarahan, S., and Dhall, S. (1989). Dynamic data assimilation: a least squares approach. In *Encyclopedia of Mathematics and Its Application 104*, volume 13. Cambridge University Press.

Lin, J. C. (2002). Review of research on low-profile vortex generators to control boundary-layer separation. *Progress in Aerospace Sciences*, 38(4):389–420.

Ljung, L. (1999). *System identification: theory for the user*. Prentice Hall PTR.

Lumley, J. L. (1967). The structure of inhomogeneous turbulent flows. *Atmospheric turbulence and radio wave propagation*, pages 166–178.

Ma, X. and Karniadakis, G. E. (2002). A low-dimensional model for simulating three-dimensional cylinder flow. *Journal of Fluid Mechanics*, 458:181–190.

Ma, Z., Ahuja, S., and Rowley, C. W. (2011). Reduced-order models for control of fluids using the eigensystem realization algorithm. *Theoretical and Computational Fluid Dynamics*, 25(1-4):233–247.

Marquet, O., Sipp, D., and Jacquin, L. (2008). Sensitivity analysis and passive control of cylinder flow. *Journal of Fluid Mechanics*, 615:221–252.

McKernan, J., Papadakis, G., and Whidborne, J. F. (2009a). Linear and nonlinear simulations of feedback control in plane poiseuille flow. *International journal for numerical methods in fluids*, 59(8):907–925.

McKernan, J., Whidborne, J. F., and Papadakis, G. (2009b). Design of poiseuille flow controllers using the method of inequalities. *International Journal of Automation and Computing*, 6(1):14–21.

Meliga, P., Pujals, G., and Serre, E. (2012). Sensitivity of 2-d turbulent flow past a d-shaped cylinder using global stability. *Physics of Fluids (1994-present)*, 24(6):061701.

Mettot, C., Renac, F., and Sipp, D. (2014a). Computation of eigenvalue sensitivity to base flow modifications in a discrete framework: Application to open-loop control. *Journal of Computational Physics*, 269:234–258.

Mettot, C., Sipp, D., and Bézard, H. (2014b). Quasi-laminar stability and sensitivity analyses for turbulent flows: Prediction of low-frequency unsteadiness and passive control. *Physics of Fluids (1994-present)*, 26(4):045112.

Monokrousos, A., Brandt, L., Schlatter, P., and Henningson, D. S. (2008). Dns and les of estimation and control of transition in boundary layers subject to free-stream turbulence. *International Journal of Heat and Fluid Flow*, 29(3):841–855.

Moore, B. (1981). Principal component analysis in linear systems: Controllability, observability, and model reduction. *Automatic Control, IEEE Transactions on*, 26(1):17–32.

Noack, B. R., Afanasiev, K., Morzynski, M., Tadmor, G., and Thiele, F. (2003). A hierarchy of low-dimensional models for the transient and post-transient cylinder wake. *Journal of Fluid Mechanics*, 497:335–363.

Noack, B. R., Papas, P., and Monkewitz, P. A. (2005). The need for a pressure-term representation in empirical galerkin models of incompressible shear flows. *Journal of Fluid Mechanics*, 523:339–365.

Parezanović, V., Laurentie, J. C., Fourment, C., Delville, J., Bonnet, J. P., Spohn, A., Duriez, T., Cordier, L., Noack, B. R., Abel, M., et al. (2015). Mixing layer manipulation experiment. *Flow, Turbulence and Combustion*, 94(1):155–173.

Protas, B. and Wesfreid, J. E. (2002). Drag force in the open-loop control of the cylinder wake in the laminar regime. *Physics of Fluids (1994-present)*, 14(2):810–826.

Qin, S. (2006). An overview of subspace identification. *Comp. & Chem. Eng.*, 30(10):1502–1513.

Rigas, G., Morgans, A. S., Brackston, R. D., and Morrison, J. F. (2015). Diffusive dynamics and stochastic models of turbulent axisymmetric wakes. *arXiv preprint arXiv:1506.03678*.

Rowley, C. W. (2005). Model reduction for fluids, using balanced proper orthogonal decomposition. *International Journal of Bifurcation and Chaos*, 15(03):997–1013.

Rowley, C. W., Colonius, T., and Murray, R. M. (2004). Model reduction for compressible flows using pod and galerkin projection. *Physica D: Nonlinear Phenomena*, 189(1):115–129.

Rowley, C. W. and Juttijudata, V. (2005). Model-based control and estimation of cavity flow oscillations. In *Decision and Control, 2005 and 2005 European Control Conference. CDC-ECC'05. 44th IEEE Conference on*, pages 512–517. IEEE.

Rowley, C. W., Mezić, I., Bagheri, S., Schlatter, P., and Henningson, D. S. (2009). Spectral analysis of nonlinear flows. *Journal of Fluid Mechanics*, 641:115–127.

Rowley, C. W. and Williams, D. R. (2006). Dynamics and control of high-reynolds-number flow over open cavities. *Annu. Rev. Fluid Mech.*, 38:251–276.

Rowley, C. W., Williams, D. R., Colonius, T., M., R. M., and Macmynowski, D. G. (2006). Linear models for control of cavity flow oscillations. *Journal of Fluid Mechanics*, 547:317–330.

Samimy, M., Debiasi, M., Caraballo, E., Serrani, A., Yuan, X., Little, J., and Myatt, J. H. (2007). Feedback control of subsonic cavity flows using reduced-order models. *Journal of Fluid Mechanics*, 579:315–346.

Schmid, P. J. (2007). Nonmodal stability theory. *Annu. Rev. Fluid Mech.*, 39:129–162.

Schmid, P. J. (2010). Dynamic mode decomposition of numerical and experimental data. *Journal of Fluid Mechanics*, 656:5–28.

Schmid, P. J. (2011). Application of the dynamic mode decomposition to experimental data. *Experiments in fluids*, 50(4):1123–1130.

Schmid, P. J. and Henningson, D. (2001). Stability and transition in shear flows.

Schmid, P. J., Li, L., Juniper, M. P., and Pust, O. (2011). Applications of the dynamic mode decomposition. *Theoretical and Computational Fluid Dynamics*, 25(1-4):249–259.

Seena, A. and Sung, H. J. (2011). Dynamic mode decomposition of turbulent cavity flows for self-sustained oscillations. *International Journal of Heat and Fluid Flow*, 32(6):1098–1110.

Semeraro, O., Bagheri, S., Brandt, L., and Henningson, D. S. (2011). Feedback control of three-dimensional optimal disturbances using reduced-order models. *Journal of Fluid Mechanics*, 677:63–102.

Semeraro, O., Bagheri, S., Brandt, L., and Henningson, D. S. (2013a). Transition delay in a boundary layer flow using active control. *Journal of Fluid Mechanics*, 731:288–311.

Semeraro, O., Pralits, J. O., Rowley, C. W., and Henningson, D. S. (2013b). Riccati-less approach for optimal control and estimation: an application to two-dimensional boundary layers. *Journal of Fluid Mechanics*, 731:394–417.

Sharma, A. S., Morrison, J. F., McKeon, B. J., Limebeer, D. J. N., Koberg, W. H., and Sherwin, S. J. (2011). Relaminarisation of reτ= 100 channel flow with globally stabilising linear feedback control. *Physics of Fluids (1994-present)*, 23(12):125105.

Shih, W., Wang, C., Coles, D., and Roshko, A. (1993). Experiments on flow past rough circular cylinders at large reynolds numbers. *Journal of Wind Engineering and Industrial Aerodynamics*, 49(1):351–368.

Sipp, D. (2012). Open-loop control of cavity oscillations with harmonic forcings. *Journal of Fluid Mechanics*, 708:439–468.

Sipp, D. and Lebedev, A. (2007). Global stability of base and mean flows: a general approach and its applications to cylinder and open cavity flows. *Journal of Fluid Mechanics*, 593:333–358.

Sipp, D. and Marquet, O. (2013). Characterization of noise amplifiers with global singular modes: the case of the leading-edge flat-plate boundary layer. *Theoretical and Computational Fluid Dynamics*, 27(5):617–635.

Sipp, D., Marquet, O., Meliga, P., and Barbagallo, A. (2010). Dynamics and control of global instabilities in open-flows: a linearized approach. *Applied Mechanics Reviews*, 63(3):030801.

Sirisup, S. and Karniadakis, G. E. (2004). A spectral viscosity method for correcting the long-term behavior of pod models. *Journal of Computational Physics*, 194(1):92–116.

Sirovich, L. (1987). Turbulence and the dynamics of coherent structures. *Q. Appl. Math.*, 45:561–571.

Strykowski, P. J. and Sreenivasan, K. R. (1990). On the formation and suppression of vortex 'shedding'at low reynolds numbers. *Journal of Fluid Mechanics*, 218:71–107.

Taylor, J. A. and Glauser, M. N. (2004). Towards practical flow sensing and control via pod and lse based low-dimensional tools. *Journal of fluids engineering*, 126(3):337–345.

Tinney, C., Coiffet, F., Delville, J., Hall, A., Jordan, P., and Glauser, M. (2006). On spectral linear stochastic estimation. *Exp. Fluids*, 41:763–775.

Tokumaru, P. T. and Dimotakis, P. E. (1991). Rotary oscillation control of a cylinder wake. *Journal of Fluid Mechanics*, 224:77–90.

Trefethen, L., Trefethen, A., Reddy, S., Driscoll, T., et al. (1993). Hydrodynamic stability without eigenvalues. *Science*, 261(5121):578–584.

Tu, J. H., Griffin, J., Hart, A., Rowley, C. W., Cattafesta III, L. N., and Ukeiley, L. S. (2013). Integration of non-time-resolved piv and time-resolved velocity point sensors for dynamic estimation of velocity fields. *Experiments in fluids*, 54(2):1–20.

Van Overschee, P. and De Moor, B. (1994). N4SID: Subspace algorithms for the identification of combined deterministic-stochastic systems. *Automatica*, 30(1):75–93.

Van Overschee, P. and De Moor, B. (1996). *Subspace identification for linear systems*. Kluwer.

Weller, J., Camarri, S., and Iollo, A. (2009). Feedback control by low-order modelling of the laminar flow past a bluff body. *Journal of Fluid Mechanics*, 634:405–418.

Willcox, K. and Peraire, J. (2002). Balanced model reduction via the proper orthogonal decomposition. *AIAA journal*, 40(11):2323–2330.

Estimation and control of noise amplifier flows using data-based approaches

This work aims to provide new modelling strategies for noise amplifier flows using data-based techniques. This kind of flow is particularly difficult to model since the upstream noise environment, triggering the flow via a receptivity process, is not known. We propose a system-identification approach, rather than a classical Galerkin technique, to extract the model from time-synchronous velocity snapshots and wall-shear stress measurements. The technique is illustrated using the case of a transitional flat-plate boundary layer, where the snapshots of the flow are obtained from direct numerical simulations. Particular attention is directed to limiting the processed data to data that would be readily available in experiments, thus making the technique applicable to an experimental setup. The proposed approach combines a reduction of the degrees of freedom of the system by projection of the velocity snapshots onto a POD basis combined with a system-identification technique to obtain a state-space model. This model is then used in a feed-forward control setup to significantly reduce the kinetic energy of the perturbation field and thus successfully delay transition.
In the second part of this work, the extracted model is used to determine coherent structures of the flow that are inherent to the system and not a representation of the external driving noise. The global modes and frequency response of the reduced-order model are qualitatively compared to global modes of the full-order boundary layer reported previously in the literature.
Finally, the estimator obtained using system identification is compared to an estimator obtained using a projection technique together with a Kalman filter (this method is exact but it cannot be applied in experimental setups). Here, the influence that different parameters have on the quality of the estimation has been analysed: noise in the estimation sensor, number of internal states of the reduced order model and the position of the sensor with respect to the position of the window measuring the velocity field.

Mots-clés : NOISE-AMPLIFIER FLOWS ; CLOSED-LOOP CONTROL ; SYSTEM-IDENTIFICATION ; REDUCED-ORDER MODELS ; DYNAMIC OBSERVER

Estimation et contrôle des amplificateurs de bruit avec des stratégies basées sur les données

Ce travail est consacré à la modélisation des écoulements laminaires et incompressibles de type amplificateur de bruit avec des stratégies basées sur les données. Ce type d'écoulement est particulièrement difficile à modéliser car le bruit en amont gouvernant l'écoulement n'est pas connu. On propose ici une stratégie basée sur l'identification de systèmes (plutôt qu'une technique classique de projection Galerkin) pour extraire un modèle à partir de clichés de champ de vitesse et de mesures d'un capteur situé à l'amont de l'écoulement. La technique est appliquée dans le cas d'une couche limite sur une plaque plane, avec des clichés de vitesse obtenus d'une simulation numérique des équations de Navier-Stokes. Le principe de la méthode consiste à déterminer au préalable les modes POD du champ de perturbation, de projeter les clichés de l'écoulement à chaque instant sur cette base et d'apprendre la dynamique de ces modes par des techniques d'identification. Le modèle résultant peut ensuite être utilisé pour contrôler cette dynamique de manière à supprimer les instabilités du système. Dans la première partie de cette thèse, la méthode est présentée en détail et la qualité des modèles est évaluée.
La deuxième partie, propose d'exploiter la technique décrite ci-dessus pour extraire la dynamique intrinsèque d'un écoulement de type amplificateur de bruit. On montre que la technique utilisée traditionnellement par la communauté (Dynamic Mode Decomposition) présente un biais pour ce type d'écoulement, du fait qu'elle néglige les termes de forçage, présents de façon inhérente dans ces écoulements. On propose alors d'utiliser la technique d'identification pour estimer les modes globaux de l'écoulement de façon juste et d'extraire la fonction de transfert entre le capteur amont et l'énergie cinétique des perturbations dans le champ.
La dernière partie compare de façon exhaustive les performances des modèles obtenus par la technique d'identification aux performances des modèles obtenus par une méthode de projection avec un filtre de Kalman (méthodes exactes mais non applicables dans un contexte expérimental). Différents paramètres sont analysés ici : bruit de capteur, nombre d'états dans le modèle réduit par rapport au nombre de modes POD estimés et position du capteur par rapport à la fenêtre des clichés de champ de vitesse.

Keywords : AMPLIFICATEUR DE BRUIT ; CONTROLE EN BOUCLE FERMEE ; IDENTIFICATION DE SYSTEME ; MODELE REDUIT ; OBSERVATEUR DYNAMIQUE

Office National d'Études et de Recherches Aérospatiales
BP 72 - 29 avenue de la Division Leclerc
92322 CHATILLON CEDEX
Tél. : +33 1 46 73 40 40 - Fax : +33 1 46 73 41 41
http://www.onera.fr